Experimental Study of Defect Behaviors in Germanium

Yoko Kawamura

Supervised by:
Professor Kohei M. Itoh, Keio University
Professor Paul C. McIntyre, Stanford University

March 2012

Abstract

Improvements of semiconductor integrated circuit (IC) performance have been driven mainly by miniaturization of silicon (Si) MOSFET (metal-oxide-semiconductor field-effect-transistor). However, with the gate length reaching 100 nm and below, various issues such as the increase of the leakage current, characteristic variability among many transistors, and emergence of quantum effect start to limit the advancement. Therefore, industry is seeking for reliable methods to improve the IC device performance that can be adopted in parallel to the conventional scaling approach. A partial substitution of widely used Si with germanium (Ge) is one of them because of its intrinsic electron and hole carrier mobilities that are higher by more than a factor of three compared to those of Si. Realization of Ge MOSFET whose characteristic is comparable or even higher than state-of-the-art Si CMOS, however, requires enormous efforts covering the full range between basic research and production. The present thesis focuses on understanding of defect and surface properties that will be of importance to future designing of Ge MOSFET devices and fabrication processes.

After introduction of the background in Chapter 1, Chapter 2 discusses the experimental observation of host-Ge displacements as a result of arsenic (As) impurity ion-implantations. Ge isotope superlattices (SLs) composed of alternating layers of stable isotope ^{70}Ge and naturally available Ge were grown by solid-source molecular beam epitaxy followed by As ion-implantation from the surface. Ge atoms were displaced by the collisions with implanted As ions leading to smearing of the periodicity of the Ge isotope SLs and turning heavily displaced region into the amorphous state. The average distance of the Ge displacements as a function of depth was determined from the depth profiles of ^{74}Ge measured by secondary ion mass spectroscopy (SIMS) for each sample implanted with different condition. Cross-sectional transmission electron microscopy was employed in parallel to identify the amorphous regions to reveal

that amorphization occured when the Ge displacements exceeded 0.75 nm. This critical value, 0.75 nm, was found to be independent of implantation doses.

Chapter 3 presents an experimental investigation to probe Ge self-diffusivities in biaxially-compressed Ge layers. Growth of a compressively strained Ge (s-Ge) isotope SL was conducted by sandwiching a Ge isotope SL by relaxed $Si_{0.2}Ge_{0.8}$ layers. Diffusion annealing with various temperatures and durations induces Ge self-diffusion within the strained SLs without releasing the strain. The self-diffusivities in compressively s-Ge were determined from the SIMS depth profiles of ^{74}Ge in the SLs. The self-diffusion was enhanced by the compressive biaxial strain with the degree of the enhancement being consistent quantitatively with a theory that considered local volume changes of Ge lattices around vacancies which were responsible for the diffusion.

Chapter 4 presents near-infrared (NIR) photoluminescence (PL) studies of Ge nanowires (NWs) to probe the effect of the surfaces (Ge/native oxide interfaces) on the electronic properties of Ge nanostructures. Ge NWs with a 40 nm diameter were synthesized on a Si substrate by chemical vapor deposition. The dependence of the observed PL peak position on temperatures and excitation laser powers confirmed that we observed a PL peak originating from direct-band-gap recombination in the Ge NWs for the first time. While this observation confirmed the high quality of the present Ge NWs, the diameter 40 nm was still too large to turn the Ge into direct-gap semiconductors. A simple analysis is presented to show that the absence of indirect-band-gap PL from the Ge NWs is most likely due to the fact that the non-radiative recombination rate at the Ge/native oxide interfaces is much faster than recombination via indirect band gap.

Chapter 5 presents over all summary and conclusions of this study.

Acknowledgements

number of different projects throughout my Ph.D – Tokyo City University: Professor Yasuhiro Shiraki, Assistant Professor Kentarou Sawano and Dr. Yusuke Hoshi, University of California at Berkeley: Professor Eugene Haller and Professor Oscar Dubon, The University of Warwick: Dr. Maksym Myronov. In addition, I would like to thank Professor Hartmut Bracht of University of Munster and Professor Wilfried Vandervorst of Katholieke Universiteit Leuven for many fruitful discussions.

I would like to thank San Francisco Mita-Kai members for their kind support of my time at Stanford University. I am really grateful to my U.S parents Yoko and Hiroshi Haruki, who welcomed me as a family member and allowed me to stay home during the first month of my life at Stanford University, and thereafter invited me to dinner, took me to many places, and looked after me a lot. I never felt alone thanks to the utmost hospitality. I would like to thank people at Fujitsu America Inc. I could enjoy the U.S. holidays thanks to their invitations. I also thank Takashi Toriumi and Takao John Haruki, who looked after me when I went to Stanford University for the first time.

I would like to thank Keio Tennis Team and the members, especially Coach Toshiaki Sakai, Takafumi Watanabe, Jyunko Sakamoto, and Eri Nozawa. I could get my huge energy to work hard on the Ph.D. from their energetic altitudes and activities.

To Oriha, thanks a lot for all the support during my bachelor, master,

Contents

Chapter 3
Self-Diffusion in Germanium under Biaxial Compressive Strain.........................43

Chapter 1

Introduction

1.1 Germanium versus Silicon MOS Technology

In 1947, the first transistor was invented in Bell Telephone Laboratories using bulk germanium (Ge) as the semiconducting material [1, 2]. Ge was the dominant material for solid-state devices up to early 1960s [3, 4]. During 1960s, however, before metal oxide semiconductor (MOS) field effect transistors (FETs) became technologically significant, Ge was replaced mainly by silicon (Si) [3, 4]. There was a number of reasons for this shift; the most important factor being discovery of thermal Si dioxide (SiO_2) that could isolate electrically various components in the integrated devices without significant degradation of the channel carrier mobility [3, 4]. Properties of the thermal SiO_2 as a gate dielectric on Si are far superior to those of water-soluble Ge dioxides (GeO_2) [4]. Invention of complementary MOS (CMOS) transistors in 1967 [5] was followed by incredible advancement of integration [6, 7] following the empirical trend known as Moore's law [8]. This development of the scaling technology led to so-called "ultra-large-scale integration" (ULSI) in mid 1970s with over 10 million transistors contained in a single chip.   Si-based technologies accounted for 98% of the IC market in 1995 [9]. However, with the gate length scaling down to 100 nm and below, various challenges have emerged. With the source and drain being so close to each other, suppression of leakage current sufficiently below

very small on-current (~1.0 mA/μm) is becoming more difficult.   With the on-bias coming down to the order of ~1.0 V, statistical variation of the CMOS characteristics including the on-bias among more than 10 million CMOS in a single chip is becoming a serious issue.   Therefore, some think that the gate length of 130 nm was the last CMOS generation where making the transistors smaller was sufficient to achieve the improvement forecasted by the Moore's law [10].   Therefore, suspension of Moore's law requires additional ingredients together with the conventional miniaturization approach.   In this regard, general interest in Ge is reviving due to the following factors;

·   At room temperature, intrinsic bulk Ge exhibits electron (3900 cm^2/Vs) and hole (1900 cm^2/Vs) mobilities, which are much higher than electron (1400 cm^2/Vs) and hole (500 cm^2/Vs) mobilities in intrinsic bulk Si.   To the first approximation, doubling the mobility has the same effect as reducing the channel length by half.   Furthermore, it has been demonstrated that inducing strain within Ge enables further enhancements of the carrier mobility.   The CMOS process to induce strain has been studied and improved extensively [11−14].

·   Both Ge and Si are group IV elements in the periodic table.   Therefore, Ge in Si and Si in Ge do not introduce any electronic levels that can degrade the device performance.   Therefore, Ge can be introduced to the conventional Si IC processing line readily.   Indeed SiGe heterostructure bipolar transistors (HBT) are fabricated commercially and installed in a wide variety of mobile communication tools.   Hetero-growth of Si and Ge is possible thanks to fact that the mixture of Si and Ge always takes the diamond structure regardless of their composition (i. e., single solid phase in Si-Ge binary diagram) and relatively small difference in the lattice constants between Si (5.431 Å) and Ge (5.658 Å).

·   Recent development of a variety of high-dielectric-constant gate materials such as hafnium dioxide [15, 16] and Ge oxynitride [17, 18] has allowed forming gates on Ge with the characteristic far superior to that of GeO$_2$.

1.2 Germanium Defect Studies Discussed in the Present Thesis

Despite all the advantages of Ge mentioned in the previous section, increasing the performance of the Ge ICs comparable to today's advanced Si ICs and sustaining Moore's law based partly on Ge technology requires repetition of all developments achieved for Si with Ge. This section outlines the motivations behind three core chapters of this thesis (Chapters 2–4), each of which corresponds to a small but important part of a large list of "to do" for Ge. The unified theme shared by these three chapters is investigation of defects related to miniaturization of Ge devices.

Chapter 2 investigates behavior of defects in Ge after ion-implantation of dopants and effect of post-implantation annealing. It is well-known that formation of source/drain regions involves ion-implantation of dopant impurities such as arsenic (As) for n-type MOS and boron for p-type MOS followed by post-implantation annealing to electrically activate the dopants and eliminate Ge defects created by implantation. The post-implantation annealing, however, redistribute dopants via diffusion putting the severe limitation on how small once can make the structures. Very often, the diffusion length of dopants turns out to be much larger than the length estimated by equilibrium diffusion constant for a post-implantation annealing temperature and time. This is due to the fact that doping creates excess charged point defects that enhance the dopant diffusion [19–21]. In case of the high-dose implantation of heavy elements like As, Ge matrix can even be amorphousized and behavior of dopant distribution during post-annealing with solid phase regrowth process can be quite complicated. Therefore, understanding of defect behaviors in Ge associated with implantation and post-implantation annealing is very important.

With such motivation, Chapter 2 describes experimental investigation of Ge point defect behaviors in Ge by probing stable isotope ^{74}Ge as a marker in Ge isotope superlattices (SLs) composed of alternating layers of stable isotope ^{70}Ge and naturally available Ge. Ion implantation, which provides a convenient method to produce a specified concentration profile of dopant atoms into semiconductors, has been used extensively for the fabrication of CMOS

transistors. While As ion-implantation has become a standard processes to fabricate source/drain regions in n-type MOS FETs, it is known to generate excess Ge point defects in Ge and causes amorphization of Ge host-lattices. Therefore, As diffusion in Ge and Ge self-diffusion in As-implanted Ge [19–21] have been studied in the past. However, a quantitative understanding of the effects of As ion-implantation on Ge host-lattices is yet to be achieved. Chapter 2 of this thesis describes quantitative determination of average displacements of Ge host-atoms recoiled by implanted As-atoms. Furthermore, the critical displacement length of Ge atoms for amorphization of Ge host-lattices is determined.

Chapter 3 describes an experimental investigation of Ge self-diffusion in compressively strained-Ge (s-Ge). As remarked above, electron and hole bulk mobilities in Ge are inherently higher than those in Si by a factor of approximately 3 and 4, respectively, at room temperature. In particular, since hole mobility in Si (500 cm^2/Vs) is about one third of electron mobility (1400 cm^2/Vs), there are high expectations for Ge as a high-mobility channel material for p-type MOS FETs. Furthermore, it is well known that application of biaxial compressive strain on Ge by SiGe virtual substrates leads to additional enhancements of the hole mobility thanks to the decrease in the average effective mass of carriers. Indeed, the hole mobility of 120000 cm^2/Vs [12, 13] and 3000 cm^2/Vs [14] have been achieved experimentally in biaxial compressive s-Ge at temperatures 2K and 300 K, respectively. It is of both scientific and technological interest to determine how self-diffusion of Ge is affected by the biaxial strain induced by the substrate having slightly different lattice constant. It has been well-known that self- and impurity-diffusions in Ge occur through the vacancy mechanism [19–21]. Chapter 3 shows probes of how Ge self-diffusion is affected by the biaxial compressive strain quantitatively and compared with existing models of vacancy-mediated diffusion under external stress.

Chapter 4 concerns with the possibility of reducing the dimensionality of Ge transistors further down to one-dimension. An application of Ge nanowires (NWs) for MOS FETs has been of great interest [22]. One-dimensional structures suppress carrier scattering and enable fabrication of so-called surrounding gate transistors (SGTs) [23], in which the level of leakage current can be decreased

4

significantly. However, with increasing surface-to-volume ratio, the effect of surface states and/or surface defects becomes larger in such nanowire devices. Therefore, Chapter 4 focuses on photoluminescence (PL) characterization of Ge NWs (~40 nm in averaged diameter) grown by the vapor-liquid-solid mechanism. The average diameter of the nanowires is still too large to observe pure quantum effect, i. e., in the idealistic scenario observation of PL that is similar to high quality bulk Ge is expected. However, previous PL studies on similar Ge NWs reported complete absence of PL in the near-infrared (NIR) region, near the crystalline Ge band gap, indicating that the increase of the surface fraction in such nanowires with respect to the one in the bulk Ge has led to preferential non-radiative recombination of electrons and holes at the surface states and/or surface defects. With this background in mind, the significance of Chapter 4 is observation of clear NIR PL originating from the direct-band-gap recombination of Ge for the first time. While this observation confirmed the high quality of the present Ge NWs, the diameter 40 nm was still too large to turn the Ge into direct-gap semiconductors. Furthermore, a simple analysis is presented to show that the absence of indirect-band-gap PL from the Ge NWs is most likely due to the fact that the non-radiative recombination rate at the Ge/native oxide interfaces is much faster than recombination across the indirect band gap.

References

[1] J. Bardeen and W.H. Brattain, Phys. Rev. **71**, 230 (1948).

[2] J. Bardeen and W.H. Brattain, Phys. Rev. **75**, 1208 (1949).

[3] P. Seidenberg, IEEE Center for the History of Electrical Engineering, A. Goldstein and W. Aspray (Eds.), New Brunswick, p. 35 (1997).

[4] D. P. Brunco, B. De Jaeger, G. Eneman, J. Mitard, G. Hellings, A. Satta, V. Terzieva, L. Souriau, F. E. Leys, G. Pourtois, M. Houssa, G. Wenderickx, E. Vrancken, S. Sioncke, K. Opsomer, G. Nicholas, M. Caymax, A. Stesmans, J. Van Steenbergen, P. W. Mertens, M. Meuris, and M. M. Heyns, J. Electrochem. Soc. **155**, 552 (2008).

[5] F. M. Wanlass, U.S. Patent 3,356,858 (1967).

[6] J. S. Kilby and E. Keonjian, Tech. Dig. IEDM **5**, 76 (1959).

[7] J. S. Kilby, IEEE Trans. Electron Devices **23**, 648 (1976).

[8] G. E. Moore, Electronics **38**, 114 (1965).

[9] D. J. Paul, Adv. Mater. **11**, 191 (1999).

[10] K. J. Kuhn, 13th International Workshop on Computational Electronics, Beijing, (2009).

[11] K. Sawano, Y. Abe, H. Satoh, Y. Shiraki, and K. Nakagawa, Appl. Phys. Lett. **87**, 192102 (2005).

[12] B. Rössner, D. Chrastina, G. Isella, and H. von Känel, Appl. Phys. Lett. **84**, 3058 (2004).

[13] W. -C. Tsai, C. -Y. Chang, G. -W. Huang, F. -F. Fang, Y. -H. Chang, and C. -F. Huang, Jpn. J. Appl. Phys. **36**, 323 (1997).

[14] R. People, J. C. Bean, D. V. Lang, A. M. Sergant, H. L. Störmer, K. W. Wecht, R. T. Lynch, and K. Baldwin, Appl. Phys. Lett. **45**, 1231 (1984).

[15] A. Ritenour, S. Yu I, M.L. Lee, N. Lu, W. Bai, A. Pitera, E.A. Fitzgerald, D.L. Kwong, and D.A. Antoniadis, Electron Devices Meeting, 2003. IEDM '03 Technical Digest. IEEE International, 18.2.1 (2003).

[16] N. Wu, Q. Zhang, C. Zhu, C. C. Yeo, S. J. Whang, D. S. H. Chan, M. F. Li, and B. J. Cho, Appl. Phys. Lett. **84**, 3741 (2004).

[17] H. Shang, K.-L Lee, P. Kozlowski, C. D'Emic, I. Babich, E. Sikorski, M. Ieong, H.-S. P. Wong, Kathryn Guarini, and W. Haensch, IEEE Electr. Device L. **25**, 135 (2004).

[18] H. Shang, H. Okom-Schmidt, K. K. Chan, M. Copel, J. A. Ott, P. M. Kozlowski, S. E. Steen, S. A. Cordes, H.-S. P. Wong, E. C. Jones and W. E. Haensch, Electron Devices Meeting, 2002. IEDM '02. Digest. International, 441 (2002).

[19] M. Naganawa, Y. Shimizu, M. Uematsu, K. M. Itoh, K. Sawano, Y. Shiraki, and E. E. Haller, Appl. Phys. Lett., **93**, 191905 (2008).

[20] M. Uematsu, M. Naganawa, Y. Shimizu, K. M. Itoh, K. Sawano, Y. Shiraki, and E. E. Haller, ECS Transactions **25**, 51 (2009).

[21] S. Brotzmann, H. Bracht, J. Lundsgaard Hansen, A. Nylandsted Larsen, E. Simoen, E. E. Haller, J. S. Christensen, and P. Werner, Phys. Rev. B **77**, 235207 (2008).

[22] Andrew B. Greytak, Lincoln J. Lauhon, Mark S. Gudiksen, and Charles M.

Lieber, Appl. Phys. Lett. **84**, 4176 (2004).

[23] H. T. Ng, J. Han, T. Yamada, P. Nguyen, Y. P. Chen, and M. Meyyappan, Nano Lett. **4**, 1247 (2004).

Chapter 2

Germanium Displacement Induced by Arsenic Implantation

This chapter reports quantitative evaluation of the germanium (Ge) displacement induced by arsenic ion-implantation as a function of the depth from the sample surface both in the amorphous and single-crystalline regions using $^{70}Ge/^{nat}Ge$ isotope superlattices. The profiles of ^{74}Ge in the Ge isotope superlattices were measured by secondary ion mass spectrometry and the sample structure along the depth was observed by cross-sectional transmission electron microscopy. The critical Ge displacement for amorphization induced by Arsenic implantation is found to be 0.75 nm, which is independent of the implantation doses. This value is 50% larger than a value of 0.5 nm for silicon [Appl. Phys. Express **1**, 021401 (2008)].

This work was a collaboration with Dr. Yasuo Shimizu (who is currently an Assistant Professor of Tohoku University), Hiroyuki Oshikawa, and Professor Masashi Uematsu of Keio University, and Professor Eugene Haller of University of California at Berkeley and Lawrence Berkeley National Laboratory.

2.1   Introduction

A renewed interest in the use of germanium (Ge) as a substrate material of metal-oxide-semiconductor (MOS) field-effect-transistor (FET) is increasing because carrier mobilities in Ge are inherently higher by a factor of more than 3 compared to those in silicon (Si) [1−3]. While arsenic (As) ion-implantation both into Si and Ge are important processes for the formation of the n-channel MOS transistors, they induce radiation damages including amorphization that can significantly affect redistribution of the dopants during post-implantation annealing [4−6]. Therefore, the As implantation process into Si has been studied extensively from various perspectives [7−11]. Specifically, the critical displacement of Si host-atoms, which is the average Si displacement along the depth to make the structure appear uniformly amorphous by cross-sectional transmission electron microscopy (XTEM) observation, was reported to be 0.5 nm for the case of Si [7]. However, a quantitative understanding of the effects of As implantation on Ge host-atoms and amorphization of Ge has not yet achieved.

This chapter evaluates quantitatively the average distance of Ge displacements induced by As ion-implantation as a function of the depth from the implanted surface both in the amorphous and single-crystalline regions. Moreover, the critical value of displacement of Ge host-atoms for amorphization is determined.

2.2   Native Point Defects in Crystalline Germanium

Native point defects in crystalline Ge, i.e., (a) self-interstitials and (b) vacancies, are schematically shown in Fig. 2.1. Ge self-interstitials are Ge host-atoms which occupy a site in the crystal structure at which there is usually not a Ge atom, or two or more Ge atoms sharing one or more lattice sites such that the number of host atoms is larger than the number of lattice sites. Vacancies are empty lattice sites where a Ge atom should be, but is missing. In a crystal lattice, the source of the point defects is known to be the free surface.
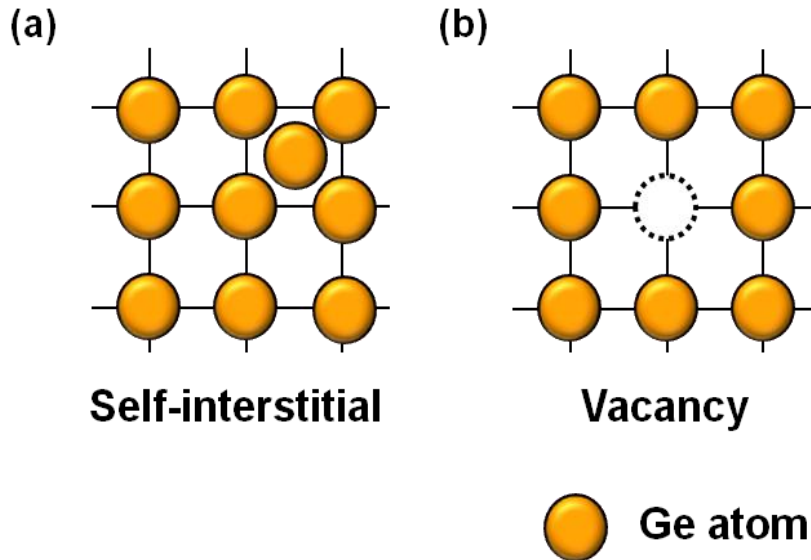
Figure 2.1 Native point defects in crystalline Ge: (a) self-interstitial and (b) vacancy.

2.3 Ion-Implantation Technique

Ion implantation is a technique by which ions of a material are accelerated by direct-current or radio-frequency electric fields and impacted into another solid target. The ion-implantation technique is used for almost all doping in the modern Si integrated circuits (ICs) and therefore it is essential for the IC technology. Among techniques of semiconductor processing, ion implantation is nearly unique in that process parameters, such as concentration and depth of the dopant, are specified directly in the equipment settings for implantation dose and energy, respectively. Thus, ion implantation has been used as the dominant method of semiconductor doping because of its precise, reliable, and repeatable control of placement of ions based on these parameters. Especially, formation of source/drain regions in MOS transistor, a main component of ICs, are realized by ion implantation of dopants, most commonly arsenic and phosphorus for n-channel MOS and boron for p-channel MOS both in Si and Ge. Due to ion implantation, however, the crystal structures of Si and Ge can be damaged or

even destroyed by the energetic collision cascades. When ions are implanted into crystalline Si or Ge, they collide with host-atoms constructing the crystal lattice and kick out the atoms from the lattice sites (knock-on). The collision and knock-on continually occur within the kinetic energy that ions initially have. Thus, ion implantation into the crystalline structure generates excess point defects (radiation damage), resulting in a non-equilibrium concentration of point defects. In particular, implantation of relatively heavy ions such as As into crystalline Ge causes a phase transition to an amorphous state. The radiation damages significantly affect dopant redistribution during post-implantation annealing to activate the dopant.

By motivated by these backgrounds, in this experiment, we have investigated radiation damages of crystalline Ge induced by As ion-implantation and determined the critical parameter for amorphization.

2.4   Growth System of Germanium Isotope Super lattice: Molecular Beam Epitaxy (MBE)

2.4.1   Germanium Isotopes

Naturally available Ge (^{nat}Ge) consists of five stable isotopes in a fixed ratio. In order to reveal the interactions between As atoms implanted into single-crystalline Ge and Ge host-atoms, a Ge isotope superlattice (SL) [12–16], composed of alternating layers of ^{nat}Ge and isotopically purified ^{70}Ge, was grown by solid-source molecular beam epitaxy (MBE). The isotope abundances in the ^{nat}Ge and ^{70}Ge sources used for MBE growth is shown in Table 2.1.

Table 2.1 Isotope abundances in the ^{nat}Ge and ^{70}Ge sources used for MBE growth

Abundance / Source	^{70}Ge	^{72}Ge	^{73}Ge	^{74}Ge	^{76}Ge
^{nat}Ge	20.5%	27.4%	7.8%	36.5%	7.8%
^{70}Ge	96.3%	2.1%	0.1%	1.2%	0.3%

2.4.2 Ultra-High-Vacuum (UHV) System in MBE

MBE is an ultra-high-vacuum (UHV)-based growth technique for producing high quality epitaxial thin films on a surface of a heated crystalline substrate with monolayer control of thickness. Figure 2.2 shows (a) a picture of a MBE chamber (EW-100, EIKO Engineering Corporation), at our group, used in this experiment and (b) a schematic illustration of the MBE growth system, where major components of the MBE system are indicated. Keeping the UHV is necessary for MBE growth. This is realized by separating the whole chamber into two parts, corresponding to a load lock chamber (preparation chamber) and a main growth chamber. A thin film sample is grown by means of molecular beams in the main growth chamber, where UHV of $\sim 10^{-11}$ Torr is maintained by an ion pump. The load lock chamber plays the role of an intermediary for loading the sample from air into the ultra-high-vacuumed growth chamber, and the vacuum pressure is maintained at approximately 10^{-8} Torr by a turbo and a rotary pump. The sample is placed in the growth chamber by two steps: (1) air to the load lock chamber and (2) the load lock chamber to the growth chamber. In Step (1), the pumps are stopped once and the chamber is exposed to the air for inserting the sample to the chamber and then vacuumed by the pumps again. In Step (2), a gate valve located between the two chambers is opened and the sample is transferred from the load lock to the growth chamber by a transfer rod. The valve is immediately closed after transfer. In this way, the growth chamber can always be at ultra-high-vacuum. In order to minimize outgassing from the internal walls and reach the UHV, a bakeout of the growth chamber at 200 °C for longer than 72 h is required for maintenance.

(a)

(b)
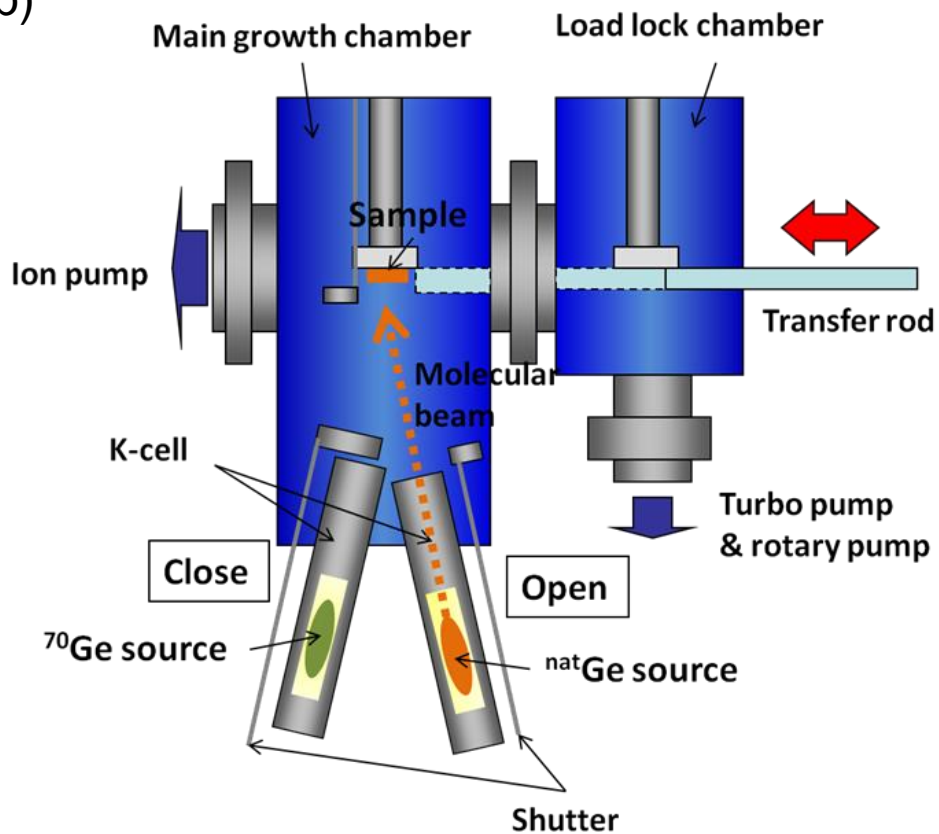
Figure 2.2 (a) Picture of a MBE chamber (EW-100, EIKO Engineering Corporation), at our group, that was used in this experiment. (b) Schematic illustration of the MBE growth system. Major components of the MBE growth system are indicated.

2.4.3   Production and Control of Molecular Beams

Molecular beams striking a substrate are produced by resistively heating up solid sources. In our experiment, ^{nat}Ge and ^{70}Ge are used as the solid sources, as in Table 2.1. They are chemically cleaned and placed in crucibles in evaporation cells which are called Knudsen cells (K-cells). Pyrolysis boron nitride (PBN) is chosen for the crucibles due to its low rate of gas evolution and chemical stability up to 1400 °C. For Si sources, tantalum crucibles are used because tantalum has a higher melting point (~3000 °C). All the crucibles are annealed at 1250 °C in the growth chamber for degassing prior to use. The ^{nat}Ge and ^{70}Ge sources are also degassed at temperatures just above the temperatures that are used for growth. The K-cells are usually kept at a temperature of 300 °C (the basic temperature), and for growth, they are heated up approximately to temperatures above 1100 °C for the Ge sources and 1400 °C for the Si sources, depending upon growing structure and sources. The control of the growing structure at monolayer level is achieved by changing the incoming beams just by opening and closing mechanical shutters located at the top of the K-cells. There also exists a shutter below the substrate so that we can control when the deposition on the substrate surface occurs and when not, even though the K-cells are heated up and molecular beams are traveling in the growth chamber. The operation time of the shutters of approximately 0.1 s is much shorter than the time needed to grow one monolayer. This is important to obtain atomically smooth and steep interfaces in the structure.

The evaporated molecules or atoms flow as beams and impinge on the hot substrate surface, where they can diffuse and eventually incorporate into the growing film. Once on the surface, the atoms move by surface diffusion until they reach a thermodynamically favorable location to bond to the substrate. Molecules dissociate to atomic form during diffusion or at a favorable site. Figure 2.3 illustrates the processes that can occur on the substrate surface. Because the atoms require time for surface diffusion, the quality of the film is generally better with slower growth.
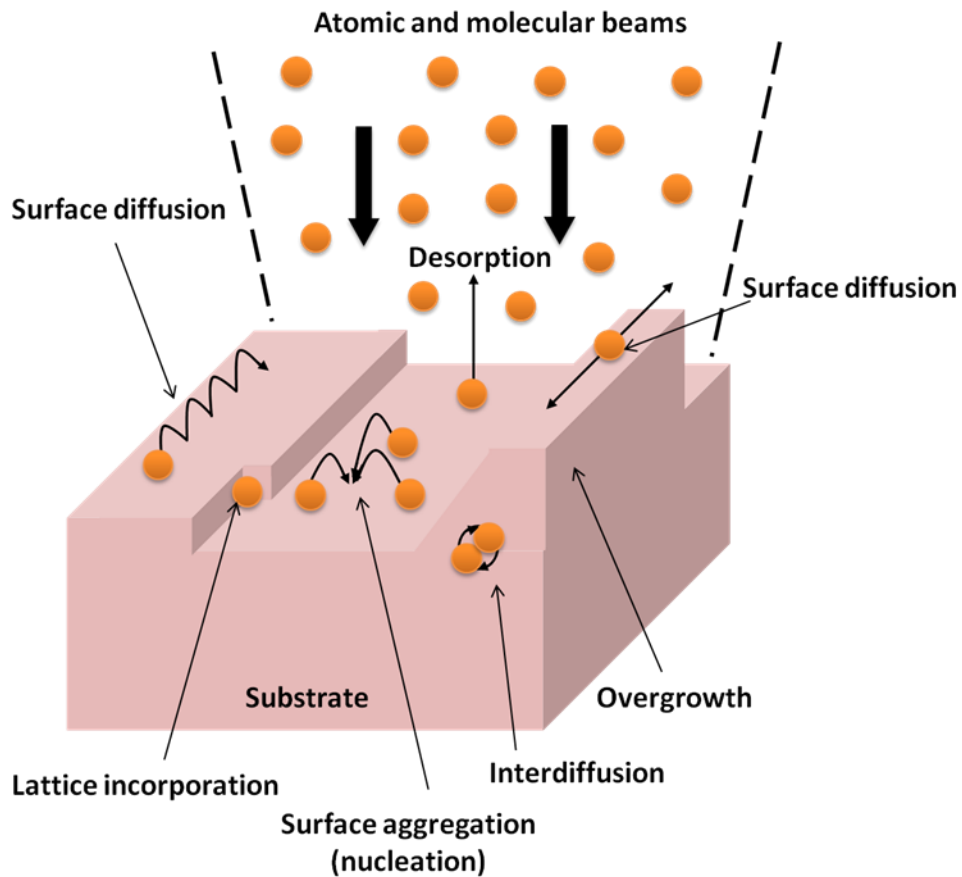
Figure 2.3 Schematic illustration of the processes occurring at the substrate surface during film growth by MBE.

2.4.4 Growth Procedure

Growth procedure of Ge isotope SL using the ultra-high-vacuumed MBE system is as follows. Ge or Ge-rich SiGe (will be described in Chapter 3) substrates are chemically cleaned: they are dipped in distilled water for 5 min

and cleaned by hydrofluoric acid (HF) treatment for 15 sec followed by thorough rinse with distilled water for 3 min. This process is repeated 3 times. Then, the substrates are put into the load lock chamber, where it is further cleaned by annealing at 150 °C for 2 h. This removes the top layers of the substrate such as natural oxide layers, which grow in air and contains impurities, or removes moistures on the substrate surface. The substrate is then carried to the main growth chamber by using the transfer rod, and again annealed at 650 °C for 30 minutes for degassing in the UHV environment and cooled down to the necessary growth temperature of 250 °C for both substrates. Note that, for the case of Si or Si-rich SiGe epitaxial growth, higher substrate temperatures should be used. The substrate is continuously rotated to obtain the growth homogeneity during growth. The total pressure in the growth chamber is approximately $\sim 10^{-10}$ Torr during growth of Ge isotope SLs. Growth rate of each isotope source will be described in 2.4.3. When growth is done, the inverse processes are basically carried out. All of the K-cell shutters and substrate shutter are closed immediately. The K-cells are gradually cooled down to the basic temperature of 300 °C to keep size and shape of the sources as same as possible because growth rate depends on these parameters. In contrast, the substrate temperature is quenched to avoid further reactions and/or growth on the surface.

2.5   Characterization Techniques

2.5.1   Secondary Ion Mass Spectroscopy (SIMS)

2.5.1.1   SIMS Measurement System

Bombardment of a sample surface with a primary ion beam followed by mass spectrometry of the emitted secondary ions constitutes secondary ion mass spectroscopy (SIMS). Today, SIMS is widely used for analysis of trace elements in solid materials, especially semiconductors and thin films. In this experiment, in order to investigate behaviors of Ge host-atoms in Ge, the distribution of ^{74}Ge isotope in a Ge isotope SL as a marker was measured by SIMS.

A SIMS measurement system mainly consists of a primary ion source (ion gun), a sample chamber, an energy analyzer, a mass spectrometer, and a detector. A primary ion beam is incident on a sample surface. The primary ions mix with sample atoms to depths of typically 1 to 10 nm and knock out secondary ions and atoms of the sample materials and resputtered primary ions from the surface layers as shown in Fig. 2.4. SIMS is therefore a locally destructive technique. These sputtered secondary particles are mass-analyzed by the mass spectrometer and then detected by the detector. Thus, molecular composition of the sample surface layers and distribution of sample elements as a function of depth can be obtained. As well as secondary ions, this sputtering process generates large numbers of electrons, which can be used to produce a physical image of the sample surface during SIMS analysis.
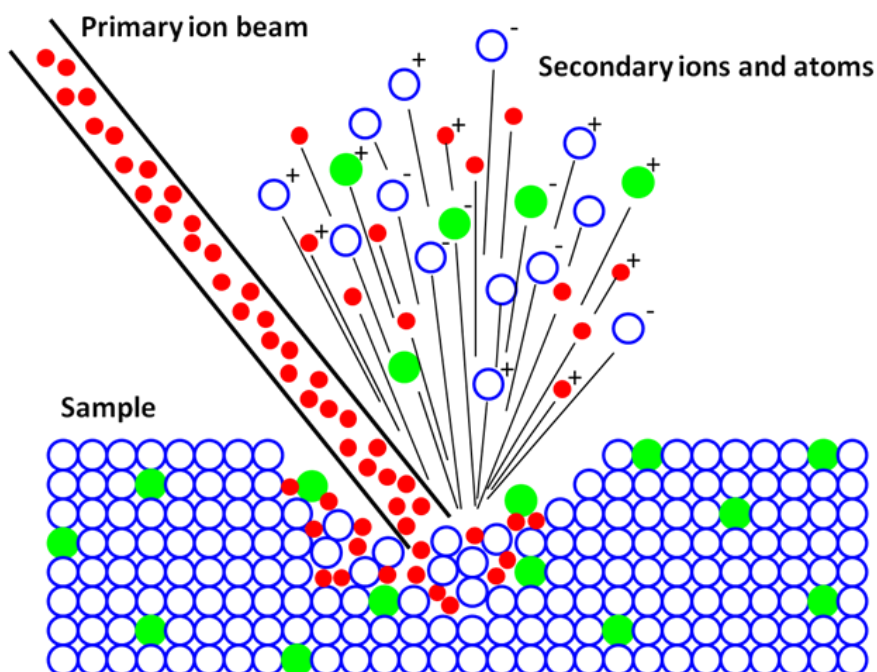
Figure 2.4 Sputtering of a sample surface by a primary ion beam. The primary ions mix with the sample atoms and knock out secondary ions and atoms of the sample materials and resputtered primary ions from the surface layers.

2.5.1.2   Measurement Mode: Dynamic SIMS and Static SIMS

In SIMS analysis, there are mainly two types of measurement modes, static SIMS (S-SIMS) and dynamic SIMS (D-SIMS). The S-SIMS mode is mostly used as a qualitative characterization of the molecular composition of the topmost surface layers. The D-SIMS mode is, on the other hand, semi-quantitative analysis of distribution of sample elements as a function of depth. During SIMS analysis, the sample surface is sputtered away by a primary ion beam. For the D-SIMS mode, by continuous sputtering of the sample surface and mass-analyzing the sputtered secondary ions, we obtain composition information as a function of depth, called a depth profile. When sputtering rate is extremely slow, the entire analysis consume only less than a tenth of an atomic monolayer from the surface. This slow sputtering mode is S-SIMS. In this work, depth profiles of ^{74}Ge isotope in the Ge isotope SL samples were obtained by using the D-SIMS mode.

2.5.1.3   Primary Ion Beam

The bombarding primary ion beam produces monatomic and polyatomic particles of sample materials and resputtered primary ions, along with electrons and photons. The secondary particles carry negative, positive, and neutral charges and they have kinetic energies that range from zero to several hundreds eV. The acceleration energy of the primary ion beam affects sputter rate. Higher primary ion energies give faster sputter rates but lower depth resolutions. The proper choice of primary ion beam energy is important for SIMS analysis. Primary ion beam species useful in SIMS analysis are mainly Cs^+ and O^{2+} ions, which are chemically active and has high ionization efficiency, i.e., secondary ion yields. The secondary ion yield can be affected by several factors. The most obvious factor is the intrinsic tendency of the sputtered ion to be ionized. O^{2+} ions are usually used for sputtering electropositive elements or those with low ionization potentials. Cs^+ ions, on the other hand, are better at sputtering negative ions with high electron affinity. The ion yield is also depends on the sample matrix. The presence of oxygen in the sample enhances positive ion yields

for most elements, but fluorine exhibits anomalously high positive ion yields in nearly all samples. Furthermore, the ion yield also depends on the primary ion beam itself. Oxygen bombardment increases the yield of positive ions and cesium bombardment increases the yield of negative ions. These increases can range up to four orders of magnitude. The proper choice of primary ion beam is therefore important in enhancing the sensitivity of SIMS. The detection limit of SIMS is severely reduced with improper selection of the ion beam. In this study, Cs^+ primary ion and the acceleration energy of 1 kV was used for sputtering both As and Ge in Ge matrix, based on the above-described concepts.

2.5.1.4   Mass Spectrometer

Mass spectrometry is an analytical technique that measures the mass-to-charge ratio of charged particles. It is used for determining masses of secondary particles and separating the particles in mass during SIMS analysis. There exist several types of mass spectrometer: mainly double forcing mass spectrometer (DF-MS), quadrupole mass spectrometer (Q-MS), and time-of-flight mass spectrometer (TOF-MS). Each type has a number of different advantages and disadvantages, depending on the purpose. The type of mass spectrometer also depends on which mode, S- or D-SIMS, is used for the analysis. In this study, PHI ADEPT-1010 D-SIMS with a Q-MS was utilized. A quadrupole mass analyzer uses oscillating electrical fields to selectively stabilize or destabilize the paths of ions passing through a radio frequency quadrupole field created between 4 parallel rods. Only the ions in a certain range of mass-charge ratio are passed through the system. The Q-MS system allows us to obtain high sensitivity and resolution depth profiles, especially of isotopes.

2.5.1.5   Depth Profiling

Monitoring the secondary ion count rate of selected elements as a function of time leads to depth profiles. To convert the time axis into depth, a profilometer is used to measure the sputter crater depth. A profilometer is a

separate instrument that determines depth by dragging a stylus across the crater and noting vertical deflections. Total crater depth divided by total sputter time provides the average sputter rate. In this work, the total sputter time was adapted so that the average sputter rate was same between different measurements and samples in order to obtain depth profiles with a same depth resolution.

2.5.1.6 Quantitative Analysis

Quantitative analysis by SIMS uses relative sensitivity factors defined according to the following equation.

$$\frac{I_R}{C_R} = RSF_E \frac{I_E}{C_E} \tag{2.1}$$

where RSF_E is the relative sensitivity factor for an element E, I_E and C_E are, respectively, secondary ion intensity and concentration for the element E, and I_R and C_R are secondary ion intensity and concentration for a reference element R. The major (or matrix) element is usually chosen as the reference. Substituting M (matrix) for R (reference) and rearranging gives the following equation:

$$C_E = RSF_E \frac{I_E C_M}{I_M}. \tag{2.2}$$

In trace element analysis, we can assume that the matrix elemental concentration remains constant. The matrix concentration can be combined with the elemental RSF (RSF_E) to give a more convenient constant, RSF:

$$RSF = C_M \, RSF_E. \tag{2.3}$$

This RSF is a function of element of interest and the sample matrix. Concentration of the element E, can be described as follows:

$$C_E = RSF \frac{I_E}{I_M}. \tag{2.4}$$

Note that RSF and C_E have the same concentration units. This is the most

common form of the RSF equation. Thus, RSF values convert the vertical axis from ion counts into concentration.

2.5.1.7 Collision Cascade Model

The collision cascade model [17] explains how the primary ion beam interacts with the sample atoms (Figure 2.5). In this model, a fast primary ion passes energy to target atoms in a series of binary collisions. Then energetic target atoms (called recoil atoms) collide with more target atoms. Target atoms that recoil back through the sample surface constitute sputtered ions, atoms, and molecules which can be collected and analyzed. The sampling depth depends on primary ion energies. Recoiled atoms can be driven in deeper depth (penetration depth) and producing surface mixing. Sputtering also leads to surface roughness in the sputter craters. Lattice imperfections, either already present or introduced by surface mixing, can be origins for roughness.
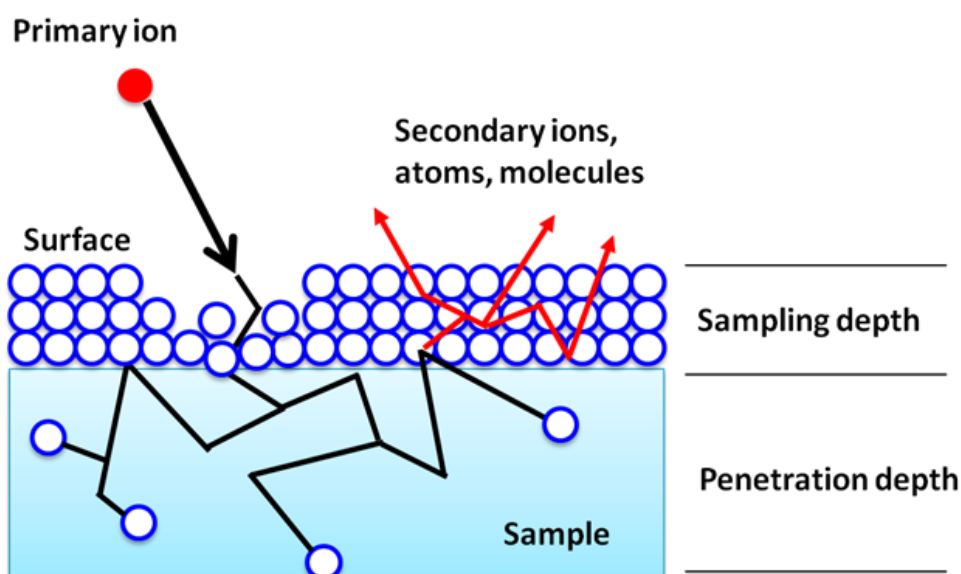
Figure 2.5 Schematic illustration of a collision cascade in a sample during SIMS analysis.

2.5.1.8   Mixing Roughness Information-Depth (MRI) Model

These artifacts during SIMS analysis, atomic mixing and surface roughing (described in 2.5.1.7), affect the depth profiles. In this work, unavoidable artificial smearing of the ^{74}Ge depth periodicity known as the SIMS artifacts was corrected by employing the mixing, roughness, and information-depth (MRI) model [18]. This model considers these artificial parameters, atomic mixing (w) and surface roughing (s). The degree of the SIMS mixing can be described by the difference between the concentration measured by SIMS, $C(x)$ and the true concentration profile $C^0(x + w)$ where w is a small distance away from, x;

$$\frac{dC(x)}{dx} = \frac{C^0(x + w) - C(x)}{w}.$$

(2.5)

The roughness is considered by superposition of a normalized Gaussian broadening as described by

$$C(x) = \frac{1}{\sqrt{2\pi}s} \int_{x-3s}^{x+3s} C^0(x')\exp\left[-\frac{(x - x')^2}{2s^2}\right] dx',$$

(2.6)

where s is the standard deviation. Note that there is no broadening in SIMS depth profiles due to the information depth and this parameter is used for auger electron spectroscopy (AES) and X-ray photoelectron spectroscopy (XPS) analysis.

2.5.2   Atomic Force Microscopy (AFM)

2.5.2.1   AFM System

Atomic force microscopy (AFM) is one type of scanning probe microscopes, which is used to image surface structures on a nm level and to measure surface forces. Figure 2.6 shows (a) a picture of a SPA300/SPI3800N AFM (Seiko) that was used in this work and (b) a schematic illustration of the

AFM system. The AFM works by scanning a semiconductor tip over a surface. The tip is positioned at the end of a cantilever. A set of the tip and the cantilever is called a probe. To acquire a surface image, the tip is brought down to the surface. A piezoelectric element is used to scan the tip line by line across the sample. As the tip is repelled by or attracted to the surface, the cantilever deflects. In order to detect this deflection, which is as small as 0.01 nm, a laser beam is focused on the back of the cantilever. Then the laser beam is reflected towards a position-sensitive photodetector. Depending on the cantilever deflection, the position of the reflected beam changes. The photodetector converts this change in an electrical signal. A plot of the laser deflection versus tip position on the sample surface provides the resolution of the hills and valleys that constitute the topography of the surface.

(a)   (b)
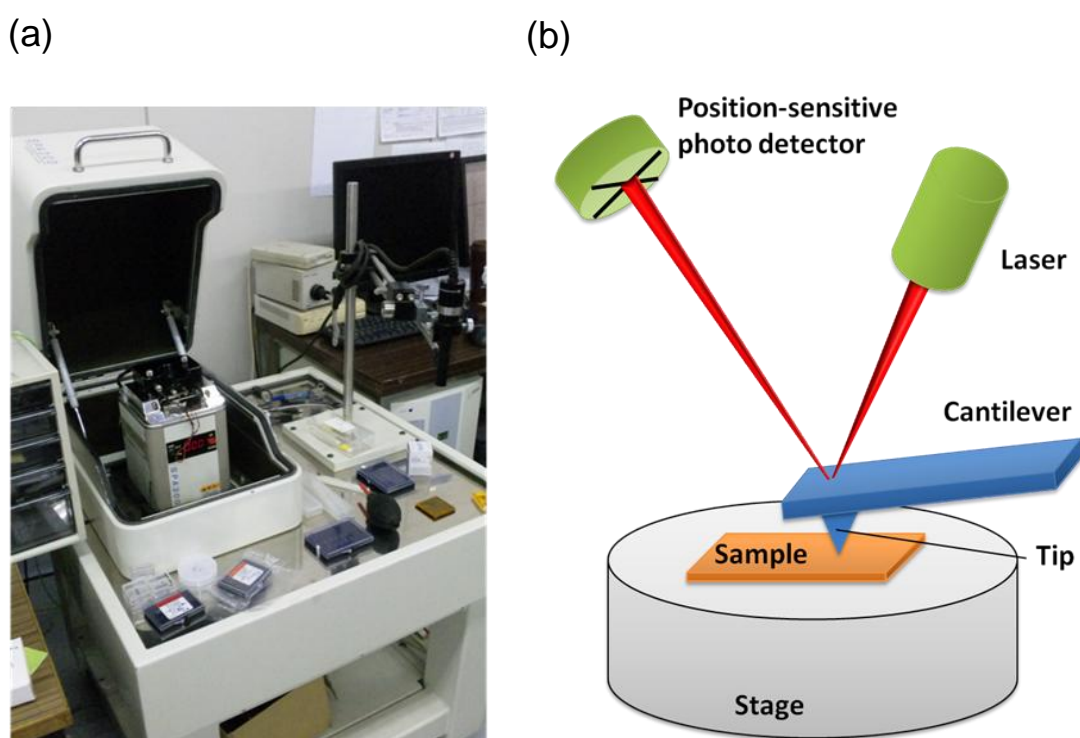
Figure 2.6 (a) Picture of a SPA300/SPI3800N AFM (Seiko) at our group that was used in this work. (b) Schematic illustration of the AFM system.

2.5.2.2 Tapping Mode (Non-Contact Mode)

The AFM can work with the tip mechanically touching the sample (contact mode), or the tip can tap across the surface (tapping mode). For the contact mode, an electronic feedback control keeps the resulting deflection constant by adjusting the z position, thus the force is measured. The contact mode has a disadvantage: the tip exerts forces to the sample. Although these forces are only of the order of 0.1−1 nN, the pressure applied to the sample can easily reach 1000 bar because the contact area is so small. This may lead to structure damages. In tapping mode, the cantilever tip is stimulated to vibrations near the resonance frequency. On approach to the surface, the vibration amplitude of the cantilever will decrease, since the interaction force with the surface shifts the resonance frequency. Instead of scanning the sample at constant deflection, the surface is scanned at constant reduction of the oscillation amplitude. As a result the tip is not in mechanical contact with the surface during the scan. The tapping mode is less destructive than the contact mode, because the exerted forces are in the pN range. An atomic force microscope can reach a lateral resolution of 0.1 to 10 nm. In this work, the tapping mode was utilized for probing the surfaces of Ge or SiGe (in Chapter 3) samples with a NC-10T Arrow NC crystalline silicon probe (NanoWorld Inc.). The resonance frequency is ~265 kHz.

2.5.2.3 Root Mean Square (RMS) Roughness

The AEM can evaluate the surface roughness of a sample by means of root mean square (RMS) described by

$$\text{RMS} = \sqrt{\frac{\Sigma\left(Z_i - Z_{\text{average}}\right)^2}{N}}. \qquad (2.7)$$

Here, the scan area is divided into 512 × 512 points and the height of each point i is described by Z_i, and Z_{average} indicates the average of Z_i. N is the number of

data points (=512×512). In this work, surface roughness of the samples was evaluated by using this RMS equation.

2.5.4 Transmission Electron Microscopy (TEM)

2.5.4.1 Interactions Between Electrons and Material

When electrons are accelerated up to high energy levels (few hundreds keV) and focused on a thin sample, some electrons can pass through the sample (transmitted electrons), and some scatter or backscatter elastically or inelastically, and also many other different signals such as characteristic X-rays, Auger electrons, secondary electrons, and light are produced (Figure 2.7). In transmission electron microscopy (TEM), the transmitted electrons and some of the elastically forward scattered electrons are used to form magnified images.
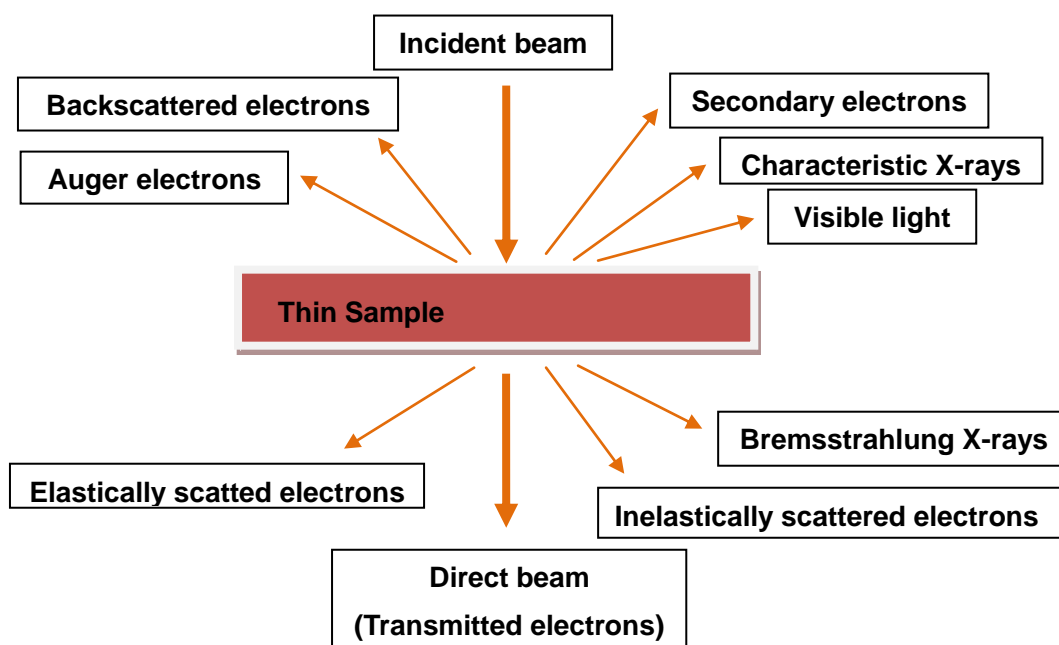
Figure 2.7 Signals generated when a high-energy beam of electrons interacts with a thin sample.

2.5.4.2 TEM Operation System

Figure 2.8 shows (a) a schematic illustration of a TEM and (b) a schematic ray-diagram of the multi-stage lens system of the TEM, imaging on the screen. The TEM consists of an electron gun (E-gun), condenser lenses, sample chamber, imaging lens system, screen, and camera chamber. The E-gun is located at the top. A heated filament emits electrons which are then accelerated by a voltage in the anode. A higher anode voltage will give the electrons a higher speed. Thus, the electrons will have a smaller de Broglie wavelength according to the equation, $\lambda = h/mv$, where h is Planck's constant, m and v are the electron mass and velocity, respectively. The resolving power of a microscope is directly related to the wavelength of the irradiation used to form an image. The faster the electrons travel, the shorter their wavelength. As the wavelength is reduced, the resolution is increased. Therefore, the resolution of the microscope is increased if the accelerating voltage of the electron beam is increased. The electron beam generated by the E-gun is focused by the condenser lenses onto a thin sample. Sample thickness should be less than 60 nm. Electrons passing through the sample (transmitted electrons and forward scattered electrons) are focused by the imaging lens system. There are essentially two types of lenses in the imaging lens system used to form the final image in TEM. These are objective and projector lenses. The electrons passing through the sample are firstly focused by the objective lens to form an image called the first intermediate image. This first intermediate image forms the "object" for the next lens, the intermediate lens, which produces a magnified image of it, called the second intermediate image. This second intermediate image becomes the "object" for the projector lens. The projector lens forms the greatly-magnified final image on the viewing screen of the microscope. These final images can be recorded by a CCD camera in the camera chamber. The whole system is enclosed in vacuum.

In this work, a Phillip TECNAI F12 FEI electron microscope was employed. The acceleration voltage of the electron beam is 200 kV, which corresponds to an electron wavelength of 0.0025 nm. The samples for TEM observations were fabricated by Argon ion-milling.

(a)

- E-gun
- Condenser lens system
- Sample Chamber
- Imaging lens system
- Screen
- Camera

(b)

- Electron beam
- Condenser lenses
- Object
- Objective lens
- Objective aperture
- First intermediate image
- Intermediate lens
- Second intermediate image
- Projector lens
- Final image
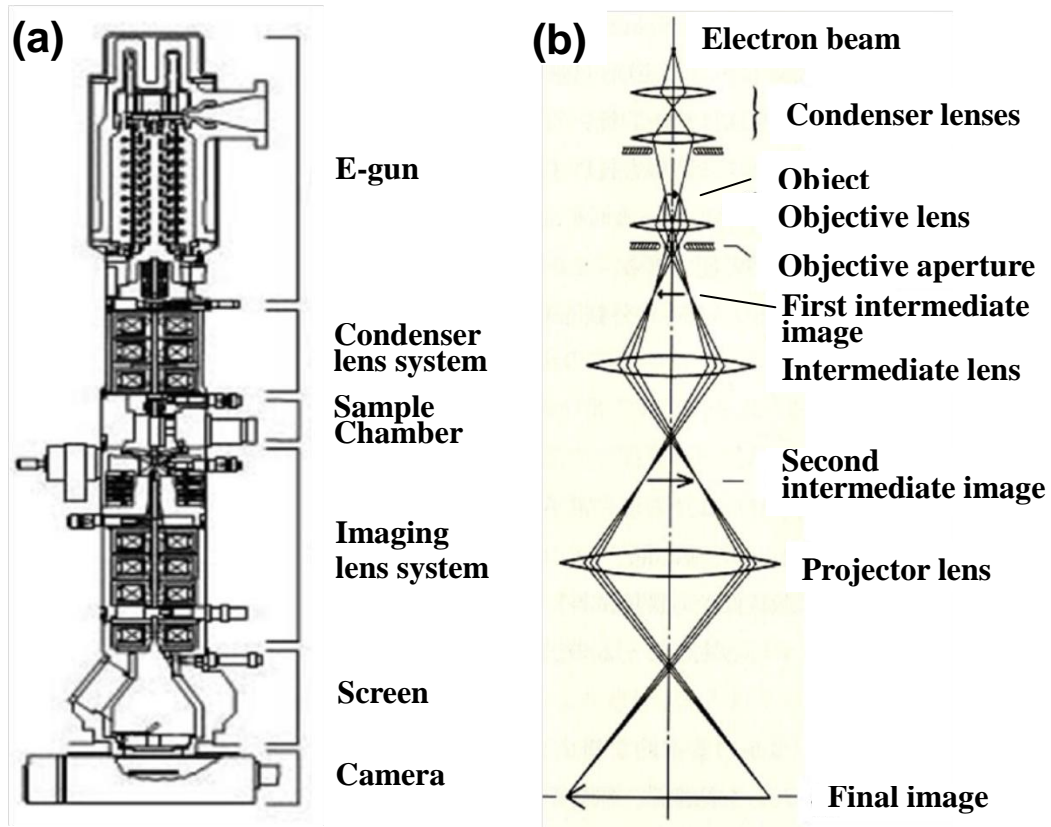
Figure 2.8 (a) Schematic illustration of a TEM system. (b) Schematic ray-diagram of the multi-stage lens system of the TEM, imaging on the screen.

2.6   Growth of Germanium Isotope Superlattice

2.6.1   Growth Rate Calibration

In order to obtain a precisely-controlled thickness of isotope layers, the growth rates of the ^{nat}Ge and ^{70}Ge K-cells in the MBE growth system were calibrated. The sample structure for the growth rate calibration is schematically shown in Fig. 2.9. An approximately-100-nm-thick ^{nat}Ge buffer layer was grown on a Ge(001) substrate. Then, a ^{nat}Ge/^{70}Ge SL structure was grown at several

K-cell temperatures: 1060, 1100, 1150 °C for ^{nat}Ge, and 1040, 1100, 1150 °C for ^{70}Ge. The growth duration of the each layer was determined so that each thickness corresponded to approximately 10 nm. The temperature of the substrate during growth was 250 °C and the sample was rotated with a consistent speed. The sample was measured by secondary ion mass spectroscopy (SIMS), PHI ADEPT-1010, using a Cs^{+} primary ion beam at 1.0 kV (see 2.5.1). Mixing roughness information-depth (MRI) analysis (see 2.5.1) was performed to estimate the thickness of the each layer. Figure 2.10 shows the depth profile of ^{74}Ge in the Ge isotope SL along with the simulation result, where atomic mixing w = 2.0, and surface roughness s = 0.9 nm in Eqs. (2.5) and (2.6), respectively, were used for the fitting. From the obtained thicknesses and the growth times of the layers, the growth rates of the ^{nat}Ge and ^{70}Ge K-cells in the MBE growth system were determined (Table 2.2).
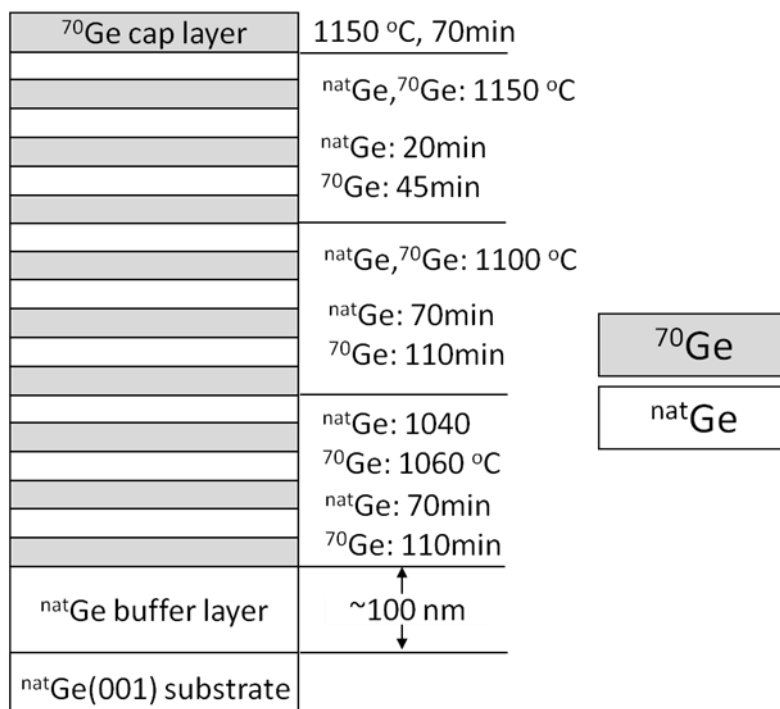
Figure 2.9 Schematic illustration of the ^{nat}Ge/^{70}Ge isotope SL grown for the growth rate calibration. The temperatures and times shown in the figure indicate the temperatures of the ^{nat}Ge and ^{70}Ge K-cells in the MBE system and growth durations for these layers.
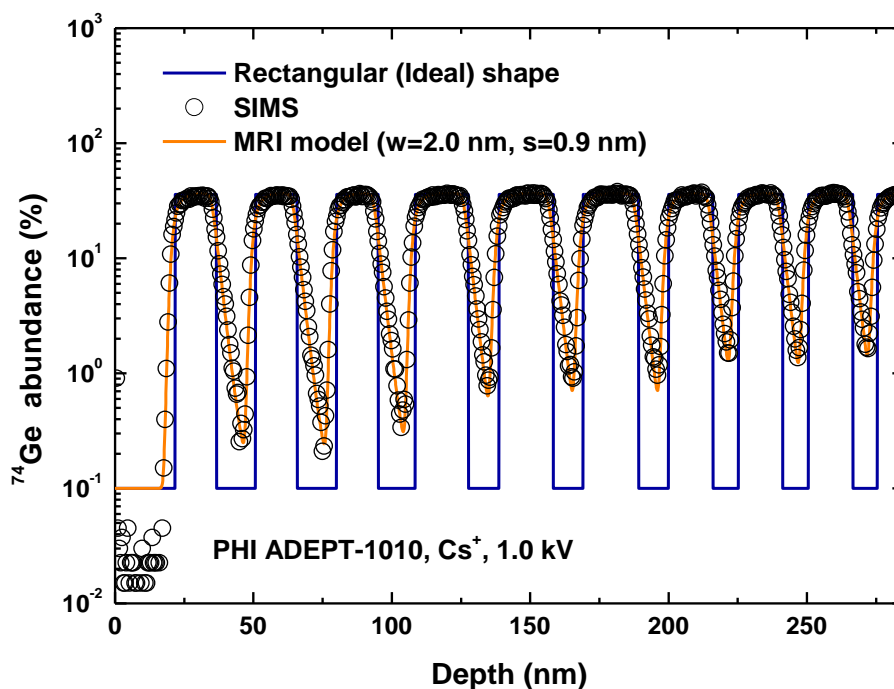
Figure 2.10 MRI analysis result and SIMS depth profile of [74]Ge in the [nat]Ge/[74]Ge isotope SL for the growth rate calibration. Atomic mixing w = 2.0 nm and surface roughness s = 0.9 nm are used for the fitting

Table 2.2 Growth rates of [nat]Ge and [70]Ge K-cells in the MBE growth system.

Cell temperature (℃)	Growth Rate (nm/min)	
	[nat]Ge	[70]Ge
1040	0.073	−
1160	−	0.039
1100	0.280	0.100
1150	0.753	0.308

2.6.2 Growth Procedure and Sample Structure

By using the determined growth rates at 1150 ℃ (0.753 nm/min for ^{nat}Ge and 0.308 nm/min for ^{70}Ge), a Ge isotope SL, composed of the alternating layers of ^{nat}Ge and ^{70}Ge, was grown by MBE on a (100)-oriented ^{nat}Ge substrate. Figure 2.11 shows a schematic illustration of the Ge isotope SL fabricated in this experiment. A 100-nm-thick ^{nat}Ge buffer layer was formed prior to the growth of the Ge isotope SL in order to achieve an atomically smooth surface. A ^{70}Ge (6 nm) / ^{nat}Ge (6 nm) multilayer was grown on the buffer layer. A 6-nm-thick ^{nat}Ge cap layer was grown on the top. The temperature of the substrates during the growth was 250 °C and the sample was rotated with a consistent speed.
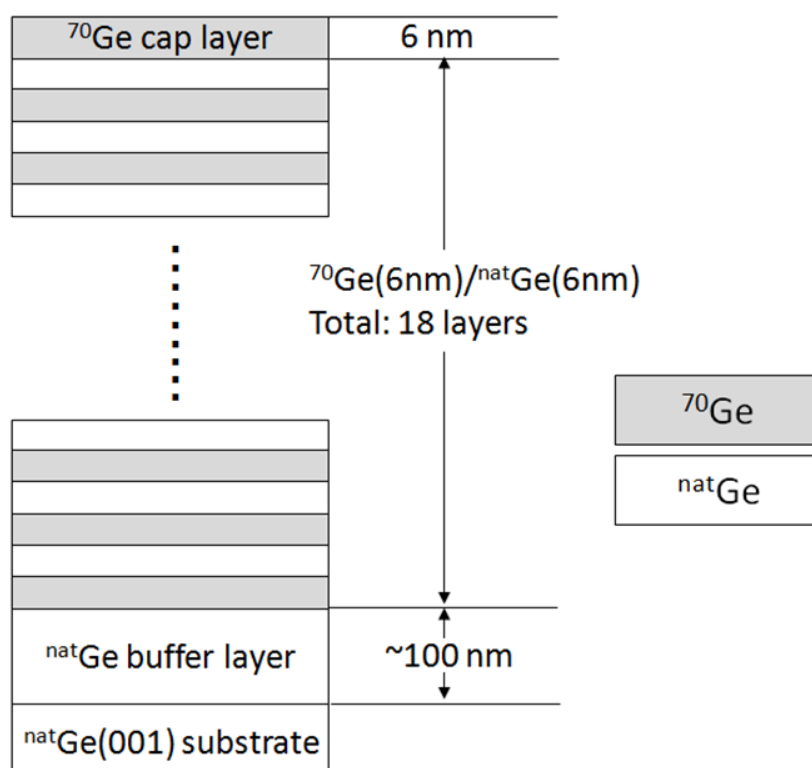
Figure 2.11 Schematic illustration of the ^{70}Ge (6 nm) / ^{nat}Ge (6 nm) isotope SL.

2.6.3   Characterization: SIMS, AFM

The depth profile of ^{74}Ge in the as-grown Ge isotope SL as a function of depth measured by SIMS (PHI ADEPT1010) using a Cs$^+$ primary ion beam at 1.0 kV is shown in Fig. 2.12. A periodicity of ^{74}Ge was observed in the Ge isotope SL. In order to estimate the layer thickness, the depth profile was reproduced by using MRI model, and the simulation result is shown in Fig. 2.12 along with the SIMS result. The same set of atomic mixing of $w = 2.0$ nm and surface roughness of $s = 0.9$ nm as for the growth rate calibration were used for the fitting. As expected, the thickness of the each layer is estimated to be 6 nm.
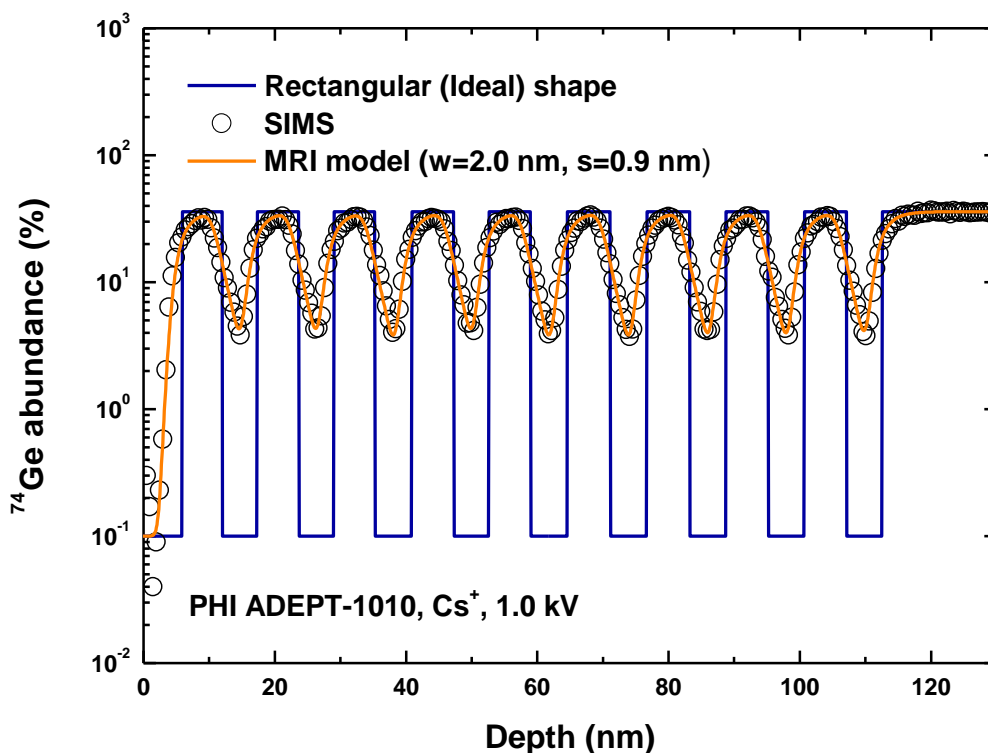
Figure 2.12 MRI analysis result and SIMS depth profile of ^{74}Ge in the ^{nat}Ge/^{70}Ge isotope SL. Atomic mixing $w = 2.0$ nm, and surface roughness $s = 0.9$ nm, are used for the fitting.

Furthermore, the sample surface was examined with AFM with a Seiko SPA300/SPI3800N AFM. The AFM image of the topmost surface of the Ge isotope SL is displayed in Fig. 2.13. The scan area is 10 × 10 µm². The surface RMS roughness was measured to be ~1.10 nm. The small RSM value indicates that a high quality single-crystalline Ge isotope SL was fabricated without impurity contamination.
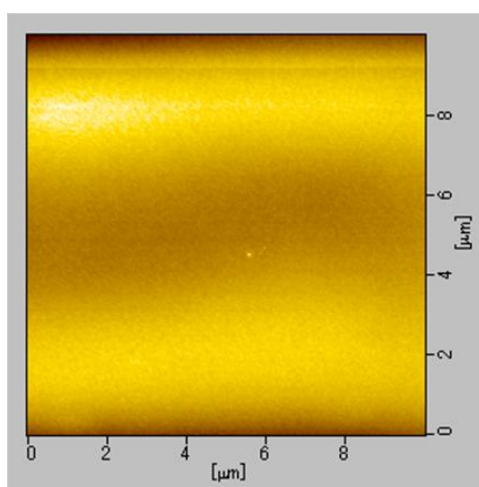
Figure 2.13 AFM image of the topmost surface of the Ge isotope SL which was grown for this experiment.

2.7   Experimental Procedures

The Ge isotope SL grown by MBE was cut into a number of smaller pieces and [75]As⁺ ions were implanted into the Ge isotope SL samples at an energy of 90 keV, which corresponded to the projected range of 40.5 nm, and with the doses in the range between 5×10^{13} and 1×10^{15} cm^{-2}. The As ion-implantation was performed with a 7° tilt angle to avoid channeling of the ions and the beam current striking the samples was ~50 µA. The depth profiles of [74]Ge and [75]As in the Ge isotope SL were obtained by SIMS (PHI ADEPT1010) using a Cs⁺ primary ion beam at 1.0 kV. XTEM observations were performed with the TECNAI F12 electron microscope operating at 200 kV.

2.8   Ion-Implantation-Induced Heating Effects

2.8.1   Room-Temperature Arsenic Ion-Implantation

As ion-implantation was initially performed at room temperature (RT). Figure 2.14(a)−(d) show the depth profiles of ^{74}Ge in the Ge isotope SLs before and after implantation with ^{75}As$^+$ ions at 90 keV with doses of 1×10^{14}, 3×10^{14}, 5×10^{14}, and 5×10^{15} cm^{-2}, respectively, and the profiles of ^{75}As in each case. In addition, XTEM images of the Ge substrates implanted under the same conditions as the SLs samples are shown in Fig. 2.15(a)−(d). As expected, the ^{74}Ge periodicity in the SIMS depth profiles of the Ge isotope SLs after As implantation was perturbed compared to the profiles before implantation. Furthermore, the mixing degree of Ge atoms in the Ge isotope SLs increases with increasing the implantation doses. On the other hand, no amorphous layer was observed from the XTEM images of the As-implanted samples with lowest (1×10^{14} cm^{-2}) and highest doses (5×10^{15} cm^{-2}) although amorphous layers with the thickness of 80 and 90 nm were observed from the samples with the middle implant doses of 3×10^{14} and 5×10^{14} cm^{-2}, respectively. This difference indicates that the amorphous Ge layers formed by the As ion-implantation were recrystallized by as so-called solid phase epitaxial (SPE) regrowth due to a local elevation of temperature caused by the implantation. Epitaxial regrowth of ion-implanted amorphous Ge on the underlying crystal substrate occurs between 300 and 400 °C with an activation energy of 2.0 eV and a rate of 10 nm/min on (100)-oriented Ge at 350 °C [19]. On the other hand, the rate of ion-implanted amorphous Si is 10 nm/min on (100)-oriented Si at 550 °C [20]. The regrowth temperature of Ge is 200 °C lower than that of Si at the same rate, which shows that recrystallization of amorphous layers more easily occurs in Ge than Si. Moreover, the XTEM images that we observed in this experiment suggest that amorphous Ge layers formed by As ion-implantation were recrystallized by a local elevation of temperature caused by implantation as we mentioned above, and besides, the recrystallized Ge regions were amorphized again due to the implanted ions with time.
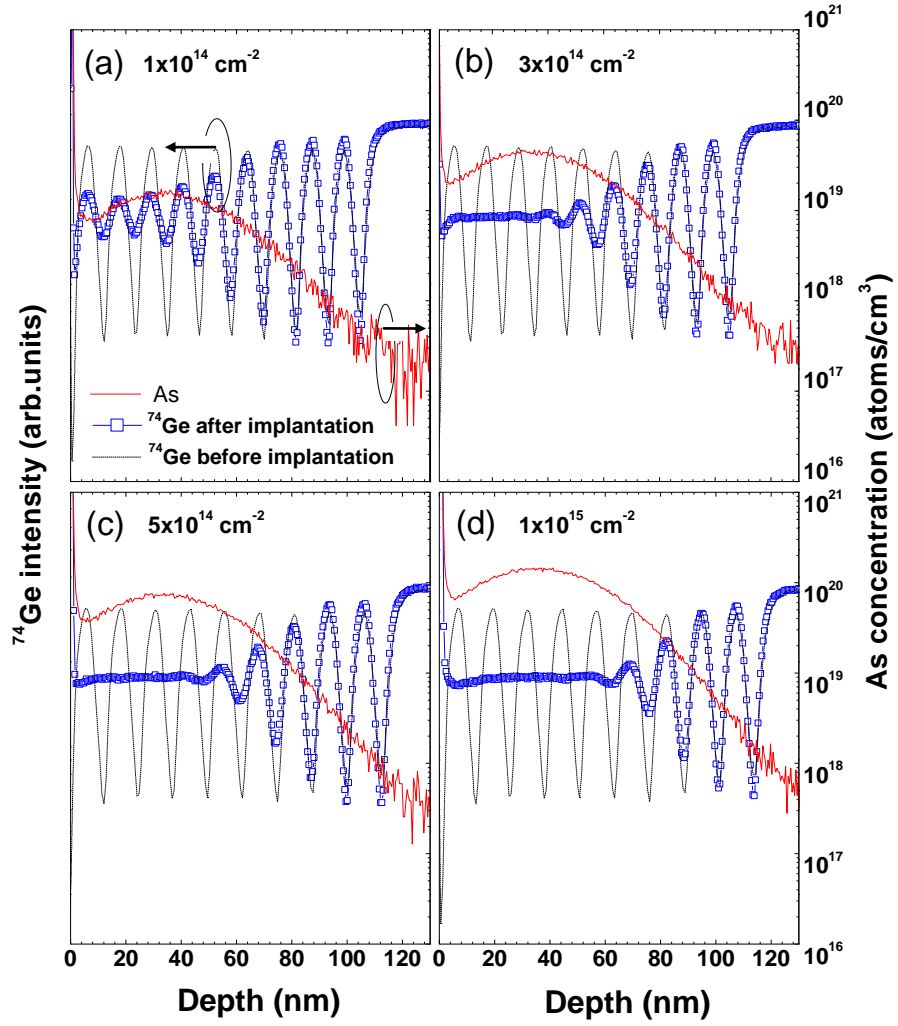
Figure 2.14 Depth profiles of [74]Ge (solid symbols) and [75]As (solid lines) in the Ge isotope SLs measured by SIMS after As implantation at the energy of 90 keV and with the doses of (a) 1×10^{14}, (b) 3×10^{14}, (c) 5×10^{14}, and (d) 1×10^{15} cm^{-2}, respectively. Dashed lines represent the profiles of [74]Ge in the Ge isotope SLs before the implantation.
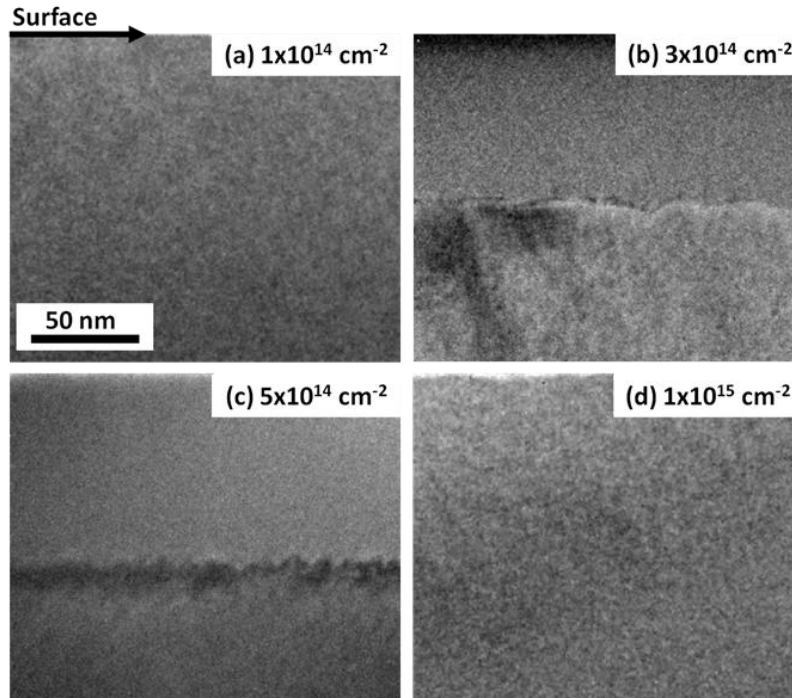
Figure 2.15 XTEM images of the Ge substrates As-implanted at the energy of 90 keV with the doses of (a) 1×10^{14}, (b) 3×10^{14}, (c) 5×10^{14}, and (d) 1×10^{15} cm^{-2}, respectively.

2.8.2   Low-Temperature (77 K) Arsenic Ion-Implantation

In order to avoid regrowth of amorphous Ge layers due to implantation-induced heating, the implantation temperature of 77 K was chosen in this study by attaching the samples directly to a holder cooled down using liquid N_2. The temperature of the substrate during implantation was below -100 °C. Figure 2.16 compares between the SIMS depth profiles of the samples implanted with the dose of 1×10^{14} cm^{-2} at room- and liquid-N_2- temperatures. This observation confirmed that the temperature difference did not affect the mixing degree of Ge atoms due to implantation in SIMS depth profiles. We also confirmed that no recrystallization occurred during argon (Ar) ion milling prepared at RT, by comparing the XTEM samples prepared by Ar ion milling at room- and liquid-N_2- temperatures. The results obtained from the liquid-N_2-temperature implantation will be discussed below.
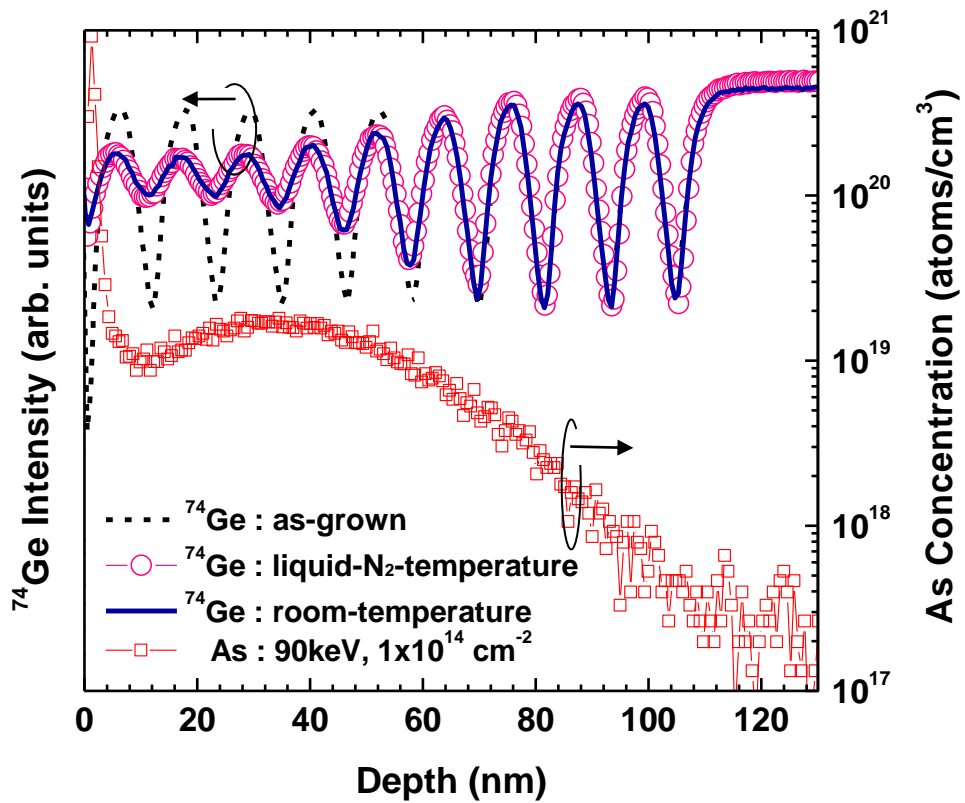
Figure 2.16 Comparison between the depth profiles of [74]Ge in the Ge isotope SLs implanted with [75]As[+] at 90 keV with the dose of 1×10^{14} cm^{−2} at liquid-N$_2$- (open circles) and room- (solid line) temperatures. The dashed line represents the depth profile of [74]Ge in the Ge isotope SL before implantation, i.e. the as-grown Ge SL. The open squares represent the depth profile of [75]As implanted into the Ge isotope SLs.

2.9 Determination of Germanium Displacements

Figure 2.17 shows the depth profiles of [75]As and [74]Ge in the Ge isotope SLs before and after As implantation at 90 keV with the doses of (a) 1×10^{14} and (b) 5×10^{14} cm^{-2}. In order to reproduce such perturbed depth profiles of [74]Ge in the Ge isotope SLs with the characteristic length of Ge atomic displacement as a function of the depth x from the surface, the following simulation model based on a convolution integral [7] was employed;

$$C_{after-implant}(x) = \int C_{before-implant}(x') \cdot g(x - x')dx'. \tag{2.8}$$

Here, $C_{after-implant}(x)$ and $C_{before-implant}(x)$ correspond to the concentration distribution of [74]Ge in the SLs after and before implantation, respectively. g(x) is a Gaussian function described by

$$g(x) = \frac{1}{\sqrt{2\pi}\sigma(x)} \exp\left[-\frac{x^2}{2\sigma(x)^2}\right], \tag{2.9}$$

where $\sigma(x)$ is the displacement of Ge host-atoms due to implantation as a function of the depth x;

$$\sigma(x) = k \exp\left[-\frac{(x-p)^2}{2d^2}\right], \tag{2.9}$$

where k, p, and d are the parameters of peak amplitude, peak position, and peak width, respectively. It is known that the distribution of the displacement of atoms by ion implantation can be approximated well by a Gaussian except for the tails [21]. The [74]Ge SIMS depth profiles after implantation are reproduced by appropriately perturbing the originally rectangular profiles of [74]Ge shown in Fig. 2.12 using Eqs. (2.8) − (2.9). In parallel, unavoidable artificial smearing of the [74]Ge depth periodicity known as the SIMS artifacts was corrected by the MRI model described in Eqs. (2.5) and (2.6). The profiles of [74]Ge perturbed by the convolution integral model were in turn broaden by the MRI model using the set of w = 2.0 nm and s = 0.9 nm, already determined for the as-grown SL in 2.6.1.
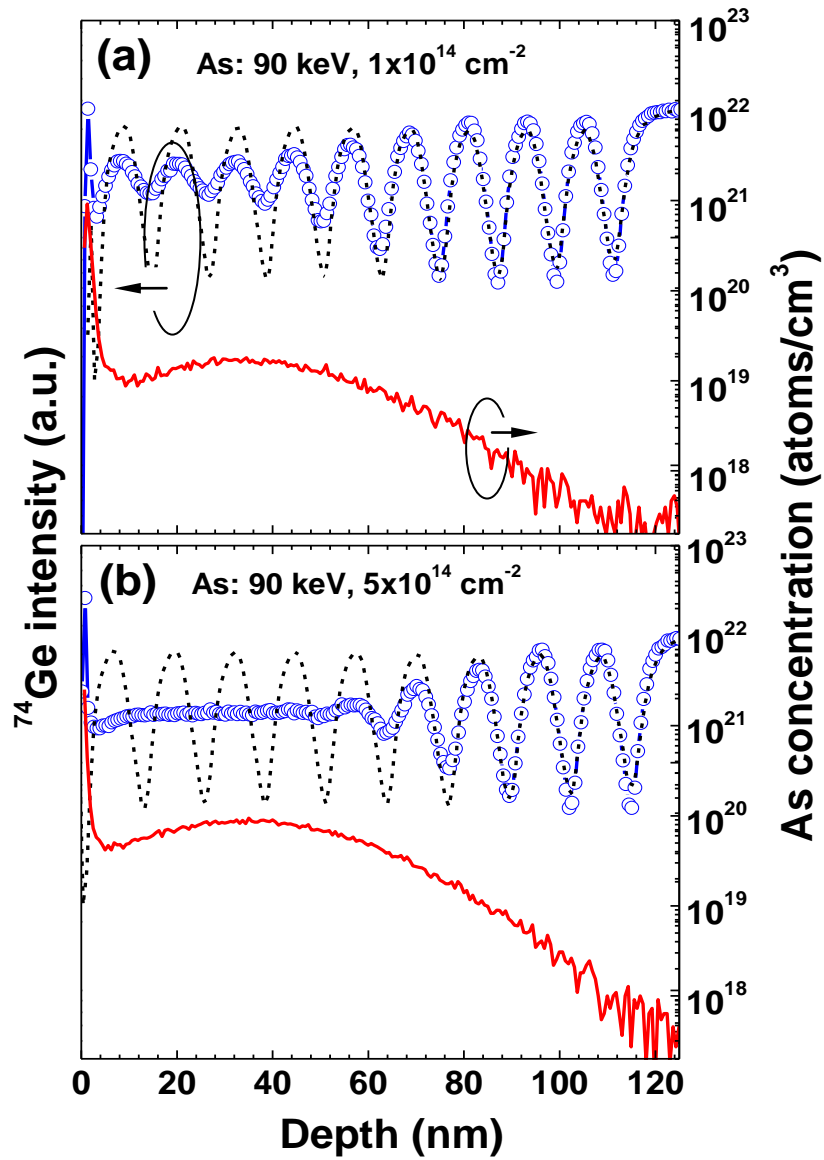
Figure 2.17 Depth profiles of ^{74}Ge (upper profiles) and ^{75}As (lower profiles) in the ^{70}Ge/^{nat}Ge isotope SLs implanted with ^{75}As$^+$ at 90 keV and with doses of (a) 1×10^{14} and (b) 5×10^{14} cm^{-2}, respectively. In the upper profiles, the dashed line and the solid symbols represent the ^{74}Ge SIMS intensity before and after As implantation, respectively.

Figure 2.18(a) shows the SIMS depth profiles of ^{74}Ge in the Ge isotope SLs implanted with 5×10^{13} cm^{-2} along with calculated profile using $k = 2.0$, $p = 24$, and $d = 31$ nm. This allows us to plot the distribution of the Ge displacement with the maximum of 2.0 nm situating at 24 nm from the surface [Fig. 2.18(b)]. The XTEM image of the same sample is shown in Fig. 2.18(c). The XTEM image shows that amorphization due to the As implantation occurred between the surface and ~66 nm in depth, while the deeper region of $x > 66$ nm remained single-crystal. Note that smeared but clearly existing periodicity of ^{74}Ge is observable even in the amorphous region. By comparing the displacement of Ge atoms shown in Fig. 2.18(b) with the XTEM image shown in Fig. 2.18(c), we find that the region where σ_C is larger than 0.75 nm appears "uniformly amorphous" in the XTEM image. Therefore, we define $\sigma_C = 0.75$ nm as the critical value of the Ge displacement for amorphization. Figures 2.18(d)–2.18(i) show similar results for the samples implanted with the doses of 1×10^{14} and 5×10^{14} cm^{-2}. We find $k = 3.2$, $p = 24$, and $d = 31$ nm for the 1×10^{14} cm^{-2} dose, and $k = 8.1$, $p = 24$, and $d = 31$ nm for the 5×10^{14} cm^{-2} dose. The XTEM images shown in Figs. 2.18(f) and 2.18(i) indicate that amorphization takes place between the surface and ~77 nm in the sample with the 1×10^{14} cm^{-2} dose, and ~92 nm in the sample with the 5×10^{14} cm^{-2} dose. Here the critical displacement of Ge atoms for amorphization $\sigma_C = 0.75$ nm remains the same and does not depend on the doses. Therefore, amorphization occurs when Ge atoms are displaced in the direction of the depth by average 0.75 nm and more. This $\sigma_C = 0.75$ nm is 50% larger than $\sigma_C = 0.5$ nm for Si [7]. This difference may be attributed to the fact that Ge−Ge bonding energy in Ge is smaller than that of Si–Si in Si [22]. Therefore, Ge atoms are more easily displaced but at the same time also more easily brought back to the substitutional sites than Si.
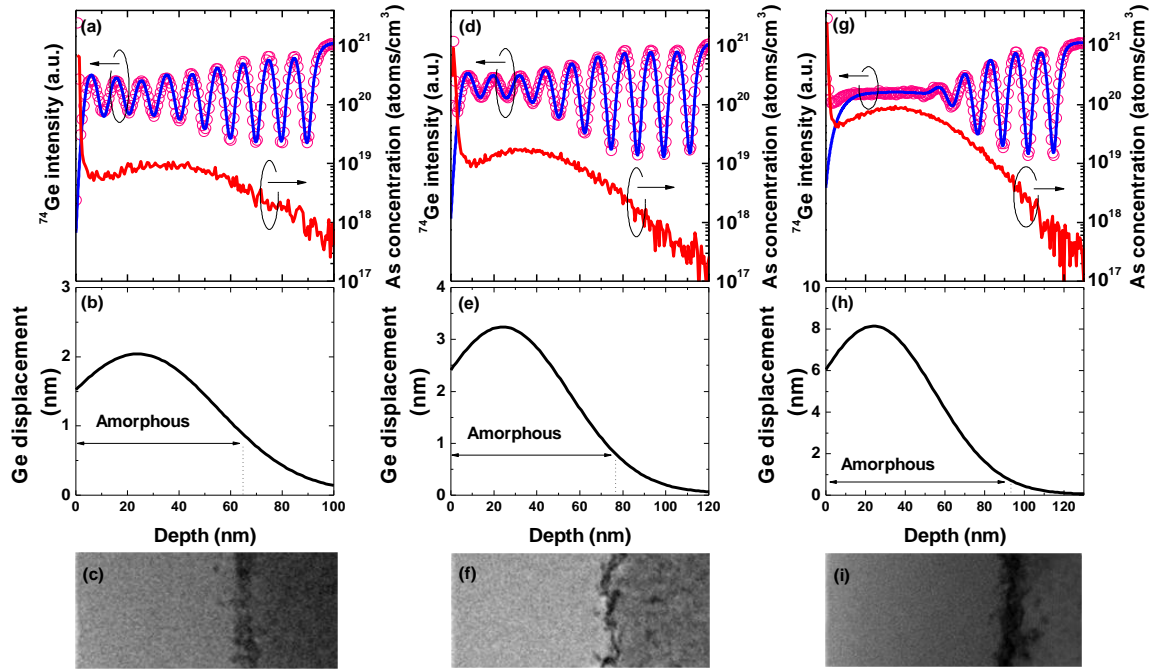
Figure 2.18 (a) Depth profiles of ^{74}Ge (upper profiles) and ^{75}As (lower profile) in the ^{70}Ge / ^{nat}Ge isotope SLs implanted with ^{75}As$^+$ at 90 keV and with the dose of 5×10^{13} cm^{-2}. In the upper profiles, the solid symbols represent the SIMS data and the solid line represents the simulation result. (b) The displacement of Ge atoms induced by As implantation as a function of the depth from the sample surface with the same scale as (a). (c) XTEM image of the sample with the same condition with the depth scale same as (a)−(b). The same set of figures for the samples As-implanted at 90 keV with the dose of 1×10^{14} and 5×10^{14} cm^{-2} are shown in (d)−(f) and (g)−(i), respectively.

2.10 Conclusions

In conclusion, we have quantitatively evaluated the displacement of Ge host-atoms induced by As ion-implantation using Ge isotope SLs. We found that amorphous layers formed by the RT implantation were recrystallized due to a local elevation of temperature caused by the implantation, and therefore liquid-N_2-temperature implantation was employed. We reproduced SIMS data using the convolution integral model and obtained good agreements between experimental data and simulation results. We showed that the critical displacement of Ge atoms necessary to make the structure appear amorphous by XTEM is 0.75 nm, which is independent of implantation doses. This value is 50% larger than a value of 0.5 nm for silicon [7].

References

[1] H. Shang, M. M. Frank, E. P. Gusey, J.O. Chu, S. W. Bedell, K. W. Guarini, and M. Ieong, IBM J. Res. Dev. **50**, 377 (2006).

[2] K. Saraswat, C. O. Chui, T. Krishnamohan, D. Kim, A. Nayfeh, and A. Pethe, Mater. Sci. and Eng. : B **135**, 242 (2006).

[3] K. H. Kim, R. G. Gordon, and A. Ritenour, Appl. Phys. Lett. **90**, 212104 (2007).

[4] Y. Kim, H. Z. Massoud, and R. B. Fair, J. Electron. Mater. **18**, 143 (1989).

[5] P. M. Fahey, P. B. Griffin, and J. D. Plummer, Rev. Mod. Phys. **61**, 289 (1989).

[6] L. Pelaz, L. A. Marques, and J. Barbolla, J. Appl. Phys. **96**, 5947 (2004).

[7] Y. Shimizu, M. Uematsu, K. M. Itoh, A. Takano, K. Sawano, and Y. Shiraki, Appl. Phys. Express **1**, 021401 (2008).

[8] Y. Shimizu, A. Takano, M. Uematsu, and K. M. Itoh, Physica B **401-402**, 597 (2007).

[9] G. F. Cerofolini, L. Meda, G. Queirolo, A. Armigliato, S. Solmi, F. Nava, and G. Ottaviani, J. Appl. Phys. **56**, 2981 (1984).

[10] P. F. Byrne, N. W. Cheung, and D. K. Sadana, Appl. Phys. Lett. **41**, 537 (1982).

[11] A. Kamgar, F. A. Baiocchi, and T. T. Sheng, Appl. Phys. Lett. **48**, 1090 (1986).

[12] K. Morita, K. M. Itoh, M. Nakajima, H. Harima, K. Mizoguchi, Y. Shiraki, and E. E. Haller, Physica B, **316-317**, 561 (2002).

[13] M. Naganawa, Y. Shimizu, M. Uematsu, K. M. Itoh, K. Sawano, Y. Shiraki, and E. E. Haller, Appl. Phys. Lett. **93**, 191905 (2008).

[14] Y. Kawamura, Y. Shimizu, H. Oshikawa, M. Uematsu, E. E. Haller, and K. M. Itoh, Appl. Phys. Express **3**, 071303 (2010).

[15] Y. Kawamura, Y. Shimizu, H. Oshikawa, M. Uematsu, E. E. Haller, and K. M. Itoh, Physica B **404**, 4546 (2009).

[16] E. Silveira, W. Dondl, G. Abstreiter, and E. E. Haller, Phys. Rev. B **56**, 2062 (1997).

[17] S. Matteson, Appl. Phys. Lett. **39**, 288 (1981).

[18] S. Hofmann, Surf. Interface Anal. **21**, 673 (1994).

[19] L. Csepregi, R. P. Kullen, J. W. Mayer, and T. W. Sigmon, Solid State Commun. **21**, 1019 (1977)

[20] L. Csepregi, E. F. Kennedy, J. W. Mayer, and T. W. Sigmon, J. Appl. Phys. **49**, 3906 (1978).

[21] D. K. Brice, J. Appl. Phys. **46**, 3385 (1975).

[22] B. deB. Darwent, "National Standard Reference Data Series", National Bureau of Standards, Washington, DC, No. 31 (1970).

Chapter 3

Self-Diffusion in Germanium under Biaxial Compressive Strain

This chapter presents the effect of biaxial compressive strain on Ge self-diffusion. Under a compressive biaxial strain of ~0.71%, Ge self-diffusion has been measured using an isotopically controlled Ge single-crystal layer grown on a relaxed $Si_{0.2}Ge_{0.8}$ virtual substrate. The self-diffusivity is enhanced by the compressive strain and its behavior is fully consistent with a theoretical prediction of a generalized activation volume model of a simple vacancy-mediated diffusion, reported by Aziz *et al.* [Phys. Rev. B **73**, 054101 (2006)]. The activation volume of −(0.65±0.21) times the Ge atomic volume quantitatively describes the observed enhancement due to the compressive biaxial strain very well.

3.1 Introduction

Compressively strained Ge (s-Ge) grown on a relaxed $Si_{1-x}Ge_x$ virtual substrate is attracting much attention as a promising candidate for next generation higher mobility p-type metal oxide semiconductor (MOS) field effect transistors (FETs) owing to its high hole mobility [1−3]. Knowledge of self-diffusion in Ge under compressive biaxial stain, which is required to understand the kinetics of the dopant diffusion and activation, is essential for the development of the s-Ge based MOS technology. In addition, the investigation of self-diffusion is important, not only to design appropriate device processing schemes, but also from the physics point of view. Self-diffusion is the most fundamental process of atomic transport in a solid. A study of self-diffusion can provide valuable information on the properties of native point defects, which are responsible for the diffusion processes. In particular, Ge self-diffusion in Ge takes place by a simple vacancy-mediated mechanism. The s-Ge matrix is, therefore, an ideal system to study and to understand the effect of strain on self-diffusion in a solid.

Recently, Si and Ge self-diffusion in relaxed $Si_{1-x}Ge_x$ has been widely investigated by probing the concentration profiles of stable or radio isotopes as tracers in relaxed $Si_{1-x}Ge_x$ epitaxial layers ($0 \leq x \leq 1$) [4−8]. In this case, a decrease in the activation enthalpy with increasing Ge content, x, has been observed. The influence of compressive strain on the Si/Ge interdiffusion has been described in the literature by Cowern *et al* [9]. In their case, enhanced Ge diffusion has been observed. On the contrary, the number of self-diffusion studies in strained materials is extremely limited. Zangenberg *et al.* have reported retardation (enhancement) of Ge self-diffusion in $Si_{0.9}Ge_{0.1}$ under the tensile (compressive) strain of 0.21% [4]. However, a theoretical description of the observed phenomena was not achieved because of the complication induced by the existence of two constituents, Si and Ge, and due to multi-diffusion mechanisms involving interstitials and vacancies. Aziz *et al.* [10−12] have theoretically predicted the thermodynamic effects of hydrostatic pressure and biaxial strain on dopant- and self-diffusion mediated by the simple vacancy and interstitial mechanism in a crystalline solid based on a generalized activation

volume model. They demonstrated the consistency of the prediction for antimony (Sb) diffusion in hydrostatically compressed Si and in biaxially strained Si (tensile) and SiGe (compressive). For self-diffusion, however, the theoretical finding has never been experimentally tested.

This chapter reports on an experimental study of self-diffusion in Ge under biaxial compressive strain. The experimental observation is quantitatively described in terms of the behavior of the vacancies in Ge by means of the activation volume with relevant previous experimental diffusion results.

3.2 Basics of Self-Diffusion in Germanium

3.2.1 Diffusion Equation

Diffusion equation is the mathematical model of diffusion phenomena using partial differential equation, first reported by Adolf Fick (1829−1901) in 1855 [13]. Here, we derive the one-dimensional diffusion equation. The mass flux (J) of a diffusion component is defined as the mass of the diffusion component flowing per unit time through unit cross sectional area. Fick found by direct observation that the magnitude of the mass flux is proportional to the magnitude of the concentration gradient at that point, i.e.

$$J(x) = -D\frac{\partial C}{\partial x} , \qquad (3.1)$$

where C is the concentration of the diffusion component and D is the diffusion coefficient (diffusivity). Eq. (3.1) is kwon as Fick's first law.

In order to obtain more useful relation, we consider a mass-flow small volume with unit cross sectional areas along the x axis, as shown in Fig. 3.1. Mass conservation is a general physical constraint that may be imposed on diffusion system. If the mass fluxes entering at $x = x$ and leaving at $x = x + dx$ in the mass-flow small volume do not balance, a net accumulation (or loss) occurs in the volume. Thus, the mass balance may be expressed as

$$\text{inflow} - \text{outflow} = \text{accumuration rate.} \qquad (3.2)$$
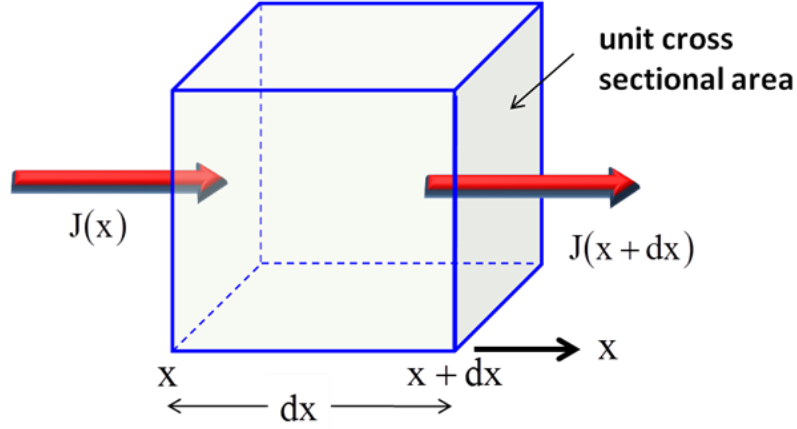
Figure 3.1 Mass-flow small volume with unit cross sectional areas along the x axis

Therefore, if dx is very small, the mass flux at $x = x$, $J(x)$, can be described by using the flux at $x = x + dx$, $J(x + dx)$, as follows:

$$J(x) = J(x + dx) - dx\left(\frac{\partial J}{\partial x}\right). \tag{3.3}$$

Furthermore, the time derivative of the concentration $(\partial C/\partial t)$ represents the time rate of change of the concentration within the small volume. Thus, $J(x) - J(x + dx)$ can be described by

$$J(x) - J(x + dx) = dx\left(\frac{\partial C}{\partial t}\right) = -dx\left(\frac{\partial J}{\partial x}\right). \tag{3.4}$$

By inserting Eq. (3.1) into Eq. (3.4), we can obtain Fick's second law:

$$\frac{\partial C}{\partial t} = \frac{\partial}{\partial x}\left(D\frac{\partial C}{\partial x}\right). \tag{3.5}$$

In addition, if the diffusivity D is constant, Eq. (3.5) simplifies to the linear form of Fick's second law:

$$\frac{\partial C}{\partial t} = D\frac{\partial^2 C}{\partial x^2} \, .$$

(3.6)

Fick's second law shown in Eq. (3.6) is also called the linear diffusion equation and widely used to obtain diffusivities in materials.

3.2.2   Germanium Self-Diffusion Mechanism

Elements diffusing in semiconductors such as Si and Ge are classified into either "slow" or "fast" diffusers in relative manners. Fast diffusers have diffusivity that is many orders magnitude larger than that of slow diffusers. The large difference between fast and slow diffusers is caused by the different diffusion mechanisms, which are closely related to their incorporation in the lattice. Fast diffusers, such as copper, lithium, hydrogen, or iron, are predominantly interstitially dissolved and move by jumping from one interstitial site to another interstitial site without any contribution of point defects (self-interstitials (I) and vacancies (V)). Slow diffusers, such as common group III and group V dopants, are substitutionally dissolved and require point defects for their diffusion processes.

Diffusion of host atoms, i.e., self-diffusion, in Si and Ge is also mediated by point defects as well as slow dopant diffusers. In the slow diffusion, the diffusivity depends on which point defect dominates the diffusion process and self-diffusion in Ge is different from self-diffusion in Si in that sense. The self-diffusion mechanisms involving self-interstitials and vacancies are called interstitialcy and vacancy mechanisms, respectively. For the interstitialcy mechanism as shown in Fig. 3.2(a), a self-interstitial (I) replaces a lattice atom (A_s), which then becomes a self-interstitial in return. The reaction can be described by

$$I \Leftrightarrow A_s + I.$$

(3.7)

For the vacancy mechanism (Fig. 3.2(b)), a lattice atom is replaced by a neighboring vacancy (V) and the reaction is described by

$$V \Leftrightarrow A_s + V. \tag{3.8}$$

It is known that self-diffusion in Si takes palace via both Si self-interstitials and vacancies, depending on diffusion temperature [14]. On the other hand, self-diffusion in Ge is mediated by simply the vacancy mechanism [15].
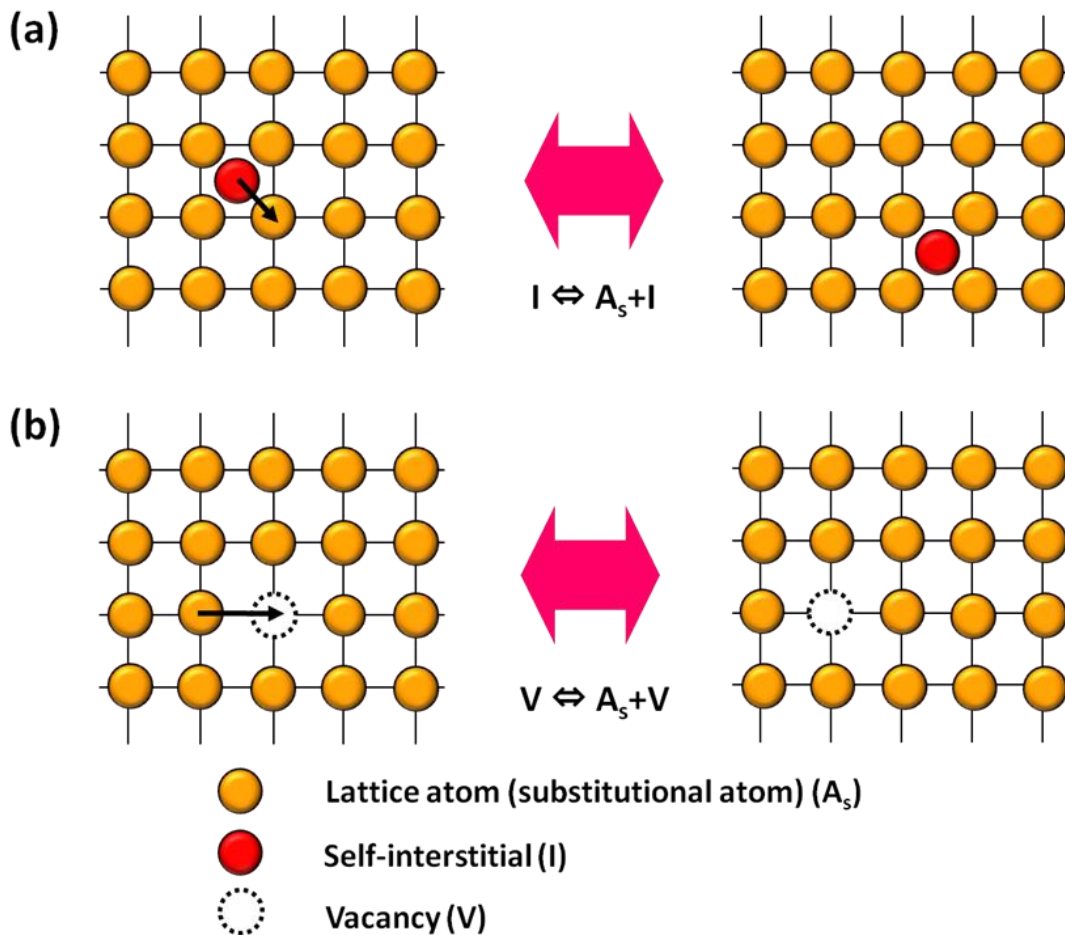
Figure 3.2 Mechanisms of self-diffusion for a two dimensional lattice: (a) Interstitialcy and (b) vacancy mechanisms. Ge self-diffusion takes place by simply the vacancy mechanism, while Si self-diffusion takes place via both mechanisms.

3.2.3   Germanium Self-Diffusivity

Typically, diffusivity, D, depends on temperature and the temperature dependence is described by an Arrhenius expression:

$$D = D_0 \exp\left(-\frac{H^M}{k_B T}\right).$$ (3.9)

Here, H^M is the activation enthalpy of migration, k_B is the Boltzmann constant, and T is the absolute temperature. D_0 is the pre-exponential factor and described by

$$D_0 = \gamma a^2 \nu \exp\left(\frac{S^M}{k_B}\right),$$ (3.10)

where γ is the geometrical constant, a is the lattice parameter, ν is the attempt frequency and S^M is the entropy of migration.

As mentioned in 3.2.2, the self-diffusion in Si and Ge takes place via point defects. Therefore, the concentrations of the point defects should be taken into account for the self-diffusivities. The equilibrium concentrations of point defects, $C_{I,V}^{eq}$, are given by

$$\frac{C_{I,V}^{eq}}{N_0} = \exp\left(\frac{S_{I,V}^F}{k_B}\right) \exp\left(-\frac{H_{I,V}^F}{k_B T}\right),$$ (3.11)

where N_0 is the atomic density (5×10^{22} cm^{-3} for Si and 4.4×10^{22} cm^{-3} for Ge), $S_{I,V}^F$ and $H_{I,V}^F$, respectively, are the entropy and activation enthalpy of defect formation. Thus, the self-diffusivity, D^{SD}, is described as a sum of two terms corresponding to the two types of point defects:

$$D^{SD} = f_I \frac{C_I^{eq}}{N_0} D^I + f_V \frac{C_V^{eq}}{N_0} D^V.$$ (3.12)

Here, D_I and D_V are the diffusivities of I and V. f_I and f_V are the correlation factors for I and V, respectively, and in the diamond structure $f_I \approx 0.73$ and $f_V \approx 0.5$ are known. By substituting Eqs. (3.9) and (3.11) to Eq. (3.12), the self-diffusivity becomes

$$D^{SD} = f\gamma a^2 \nu \exp\left(\frac{S^{SD}}{k_B}\right) \exp\left(-\frac{H^{SD}}{k_B T}\right), \tag{3.13}$$

where $S^{SD} = S^M + S^F$, $H^{SD} = H^M + H^F$. Furthermore, by describing D_0 by

$$D_0^{SD} = f\gamma a^2 \nu \exp\left(\frac{S^{SD}}{k_B}\right), \tag{3.14}$$

the self-diffusivity, D^{SD}, can be described by

$$D^{SD} = D_0^{SD} \exp\left(-\frac{H^{SD}}{k_B T}\right). \tag{3.15}$$

It has been experimentally demonstrated that Si self-diffusion in Si takes palace via both Si self-interstitials and vacancies in the temperature range of 735 to 1388 °C [14]. Specifically, at high temperature above approximately 900 °C, Si self-interstitials dominate the self-diffusion, and at low temperature below 900 °C, the vacancy-mediated self-diffusion dominantly occurs [14]. Therefore, Si self-diffusivity describes by a sum of two exponential terms [14]:

$$D_{Si}^{SD} = 2175.4 \exp\left(-\frac{4.95\ eV}{k_B T}\right) + 0.0023 \exp\left(-\frac{3.6\ eV}{k_B T}\right) \frac{cm^2}{s}. \tag{3.16}$$

Here, the first term represents Si self-diffusion due to the self-interstitial mechanism. The second term represents Si self-diffusion due to the vacancy mechanism. On the other hand, it has been experimentally demonstrated that Ge self-diffusion is predominantly mediated by the vacancy mechanism in the wide temperature range of 429 to 904 °C and the reported Ge self-diffusivity [15] is

$$D_{Ge}^{SD} = 25.4\ c\exp\left(-\frac{3.13\ eV}{kT}\right) \frac{cm^2}{s}. \tag{3.17}$$

The enthalpies of vacancy-madiated self-diffusion in Si (the second term) and Ge are very smilar.

3.3   X-Ray Diffraction (XRD) Technique Used for Strain Analysis

3.3.1   Biaxial Strain in Crystal Lattice

When a crystal with a lattice constant, a, is biaxially strained, the horizontal (in-plane) strain ($\varepsilon_{\parallel}$) and vertical strain ($\varepsilon_{\perp}$) are respectively given by

$$\varepsilon_{\parallel} = \frac{a_{\parallel} - a}{a}, \quad \varepsilon_{\perp} = \frac{a_{\perp} - a}{a}. \tag{3.18}$$

Here, $a_{\parallel}$ and $a_{\perp}$ are the horizontal and vertical crystal lattice constants, respectively. Furthermore, in general, the stress-strain relationship in cubic crystal lattice is described using the elastic coefficient tensor as follows:

$$\begin{bmatrix} T_{xx} \\ T_{yy} \\ T_{zz} \\ T_{xy} \\ T_{yz} \\ T_{zx} \end{bmatrix} = \begin{bmatrix} c_{11} & c_{12} & c_{12} & 0 & 0 & 0 \\ c_{12} & c_{11} & c_{12} & 0 & 0 & 0 \\ c_{12} & c_{12} & c_{11} & 0 & 0 & 0 \\ 0 & 0 & 0 & c_{44} & 0 & 0 \\ 0 & 0 & 0 & 0 & c_{44} & 0 \\ 0 & 0 & 0 & 0 & 0 & c_{44} \end{bmatrix} \begin{bmatrix} \varepsilon_{xx} \\ \varepsilon_{yy} \\ \varepsilon_{zz} \\ 2\varepsilon_{xy} \\ 2\varepsilon_{yz} \\ 2\varepsilon_{zx} \end{bmatrix}. \tag{3.19}$$

In the biaxially-strained crystal lattice, T_{zz} in Eq. (3.19) becomes zero, and therefore $\varepsilon_{zz} = \varepsilon_{\perp}$, $\varepsilon_{xx} = \varepsilon_{yy} = \varepsilon_{\parallel}$ is obtained. Then the relationship between the in-plane ($\varepsilon_{\parallel}$) and vertical ($\varepsilon_{\perp}$) strain can be given by

$$\varepsilon_{\perp} = -\frac{2c_{12}}{c_{11}} \varepsilon_{\parallel}. \tag{3.20}$$

By inserting Eq. (3.18) into Eq. (3.20), the relationship:

$$a_{\perp} = a \left(1 - \frac{2c_{12}}{c_{11}} \frac{a_{\parallel} - a}{a} \right) \tag{3.21}$$

can be obtained. The relevant material properties of Si and Ge at 300 K are shown in Table 3.1.

In addition, the crystal lattice constant of a relaxed $Si_{1-x}Ge_x$ crystal (a_{SiGe}) [16] is given by

<div align="center">

Table 3.1 Relevant material properties of Si and Ge at 300 K.

</div>

	Si	Ge
Crystal lattice constant (Å)	5.4310	5.6575
Elastic coefficient c_{11} ($\times 10^{10}$ N/m^2)	16.58	12.4
Elastic coefficient c_{12} ($\times 10^{10}$ N/m^2)	6.39	4.13

$$a_{SiGe} = (1-x)a_{Si} + xa_{Ge} - 0.0270x + 0.0270x^2. \tag{3.22}$$

The elastic coefficients of Si$_{1-x}$Ge$_x$ (c_{ij}^{SiGe}) are described using the elastic coefficients of Si (c_{ij}^{Si}) and Ge (c_{ij}^{Ge}) by

$$c_{ij}^{SiGe} = (1-x)c_{ij}^{Si} + xc_{ij}^{Ge}. \tag{3.23}$$

3.3.2   X-Ray Diffraction Measurement System

In this work, strain of the samples was determined by using X-ray diffraction (XRD), X'pert MRD, at Shiraki group of Tokyo City University. A cupper anode target was used as the X-ray source. Kα^1 X-rays (λ=1.5406 Å) were produced through an asymmetric Ge[220] crystal monochrometer as the incident beams. Figure 3.3 shows a schematic illustration of the X-ray measurement system utilized in this experiment. Omega (ω) is the angle between the incident X-rays and the sample surface, phi (φ) is the angle of the in-plane sample rotation, and psi (ψ) is the tilt angle of the sample. The sample stage is adjusted with respect to the incident X-ray beams by using the above-mentioned 3 angles. 2-theta (2θ) is the angle between the incident X-rays and the detector. The relationship between 2θ and ω will be described below.

Figure 3.4 shows a schematic illustration of a reciprocal lattice space in the X-ray measurement system, where the angles, ω and 2θ, satisfy the Bragg's condition (n=0) at a reciprocal lattice point (hkl), which corresponds to a set of lattice planes (hkl) in the real space lattice, and the Bragg's condition is described by
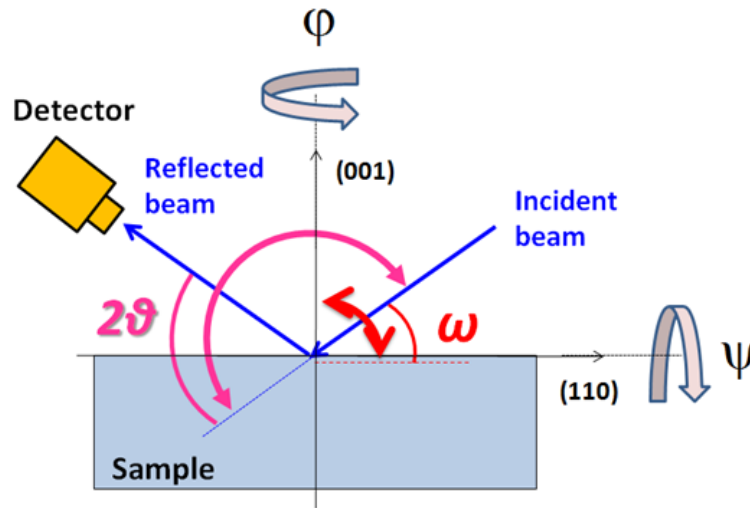
Figure 3.3 Schematic illustration of the X-ray diffraction measurement system that was used in this work.
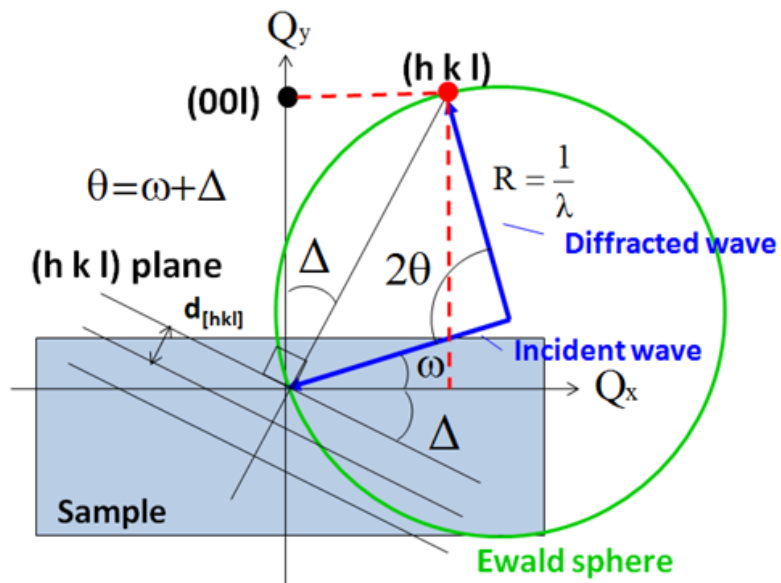
Figure 3.4 Schematic image of a reciprocal lattice space in the X-ray diffraction measurement system. The angles, ω and 2θ, satisfy the Bragg's condition (n=1) at a reciprocal lattice point (hkl), which corresponds to a set of lattice planes (hkl) in the real space lattice

$$2R \sin\theta = \frac{1}{d_{[hkl]}}. \tag{3.24}$$

Here, R is the radius of the Ewald sphere, corresponding to the inverse of the incident X-ray wavelength, $1/\lambda$. $d_{[hkl]}$ is the interplanar spacing of the lattice planes (hkl). Delta (Δ) is defined as the angle between the reciprocal lattice vectors (00l) and (hkl), and can be described by

$$\theta = \omega + \Delta, \qquad \cos\Delta = \frac{l}{\sqrt{h^2 + k^2 + l^2}} . \tag{3.25}$$

Furthermore, from this figure, horizontal (Q_x) and vertical (Q_y) reciprocal lattice units can be described by

$$Q_x = \frac{1}{d_{[hk0]}} = R\{\cos\omega - \cos(2\theta - \omega)\} \tag{3.26a}$$

$$Q_y = \frac{1}{d_{[00l]}} = R\{\sin\omega + \sin(2\theta - \omega)\}, \tag{3.26b}$$

where $d_{[hk0]}$ and $d_{[00l]}$ is the interplaner spacing of the lattice planes (hk0) and (00l), respectively, and given by

$$d_{[hk0]} = \frac{a_{\parallel}}{\sqrt{h^2 + k^2}} \tag{3.27a}$$

$$d_{[00l]} = \frac{a_{\perp}}{l}. \tag{3.27b}$$

By experimentally changing the angles, ω and 2θ, in the X-ray measurement system shown in Figs. 3.3 and 3.4, a mapping image of (Q_x, Q_y), i.e., reciprocal space map (RSM), can be obtained. By using Eqs. (3.26) and (3.27), the horizontal and vertical lattice constants ($a_{\parallel}$ and $a_{\perp}$) of the crystal lattices in the sample can be determined. Furthermore, by substituting the determined lattice constants to Eq. (3.18), the in-plane and vertical strain of the crystal lattices can be obtained. The single scan, so-called "$\omega - 2\theta$ scan", using the X-ray diffraction system was also utilized for strain analysis.

3.4   Growth of Silicon-Germanium Virtual Substrate

3.4.1   Reversed Linear Graded Technique

In order to produce biaxial compressive strain to a Ge isotope superlattice (SL) for the self-diffusion study, a Ge-rich SiGe virtual substrate was employed. In this section, the growth method and structural analysis of a $^{nat}Si_{0.2}^{nat}Ge_{0.8}$ virtual substrate used in this experiment is presented.

High quality Ge-rich SiGe buffers are typically achieved by two major techniques by using chemical vapor deposition (CVD). The one is through a two temperature growth method directly on (001)-oriented Si substrates. The other is by a slow grading of a buffer structure, which for such high-composition layers leads to a relatively thick structure, typically 8-12 µm. In this work, a reverse linear graded (RLG) buffer layer [17] was employed. The feature of the RLG method is that the alloy content is graded down from a relaxed pure Ge interlayer grown on a Si wafer to the required final composition instead of grading up from the Si wafer, which produces a high Ge composition SiGe relaxed buffer of relatively small thickness (~a few µm) and high quality with very few defects and smooth surface.

3.4.2   Growth Procedures and Sample Structure

By using the RLG method, a $^{nat}Si_{0.2}^{nat}Ge_{0.8}$ virtual substrate was grown, in collaboration with Dr. Maksym Myronov of The University of Warwick, by reduced-pressure CVD in an ASM Epsilon 2000 reactor with germane (GeH_4) and dichlorosilane (SiH_2Cl_2) as gaseous precursors. As already mentioned in Chapter 2, ^{nat}Si and ^{nat}Ge, respectively, indicate naturally available Si and Ge with the fixed abundances: ^{nat}Si: ^{28}Si: 92.2%, ^{29}Si: 4.7%, ^{30}Si: 3.1%, and ^{nat}Ge: ^{70}Ge: 20.5%, ^{72}Ge: 27.4%, ^{73}Ge: 7.8%, ^{74}Ge: 36.5%, and ^{76}Ge: 7.8%. Figure 3.5 shows a schematic illustration of the $Si_{0.2}Ge_{0.8}$/RLG SiGe/Ge/Si(001) virtual substrate grown by the RLG method. Firstly, a 1000-nm-thick Ge interlayer was grown on a Si(001) substrate. Then the RLG SiGe layer was deposited on the Ge interlayer, with the Ge content reducing linearly from x=1 to x=0.8 over a thickness of 800

Constant $Si_{0.2}Ge_{0.8}$ layer	1000 nm
Reverse liner graded (RLG) layer	800 nm (27.5%/µm)
Ge layer	1000 nm
Si (001) substrate	
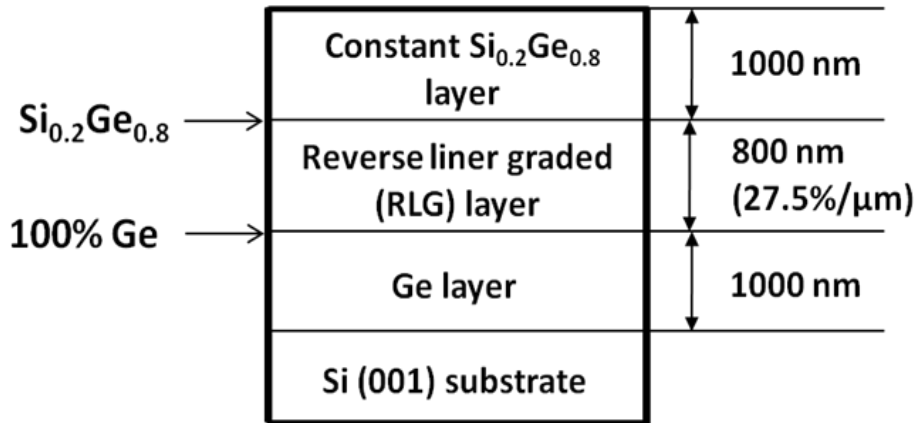
Figure 3.5 Schematic illustration of the $Si_{0.2}Ge_{0.8}$/RLG SiGe/Ge/Si(001) virtual substrate employed in this work. An effective grading rate for the 800-nm-thick RLG $Si_{1-x}Ge_x$ layer (from x=1 down to x=0.8) is 27.5 %/µm in Ge content.

nm, corresponding to an effective grading rate of 27.5 %/µm in Ge content. Finally, a 1000-nm-thick constant composition relaxed $^{nat}Si_{0.2}{}^{nat}Ge_{0.8}$ layer was grown on the top. The grading was achieved by keeping the GeH_4 flow constant and reducing the SiH_2Cl_2 flow.

3.4.3   Characterization: TEM, XRD, AFM

3.4.3.1   Cross-Sectional Transmission Electron Microscopy

In order to determine the threading dislocation density reaching the top surface, a dilute Schimmel etchant with a bulk etching rate of 2.1 nm/s followed by cross-sectional transmission electron microscopy (XTEM) observations was employed. The XTEM observations were performed along the {011} plane using a JEOL 2000FX TEM operating at 200 kV. After a 5-min Schimmel etch, a threading dislocation density of $\sim 4 \times 10^6 \, cm^{-2}$ was measured from the average of 30 XTEM images each with an area of $8.2 \times 10^3 \, \mu m^2$. A XTEM image of the virtual substrate was shown in Fig. 3.6 [17].
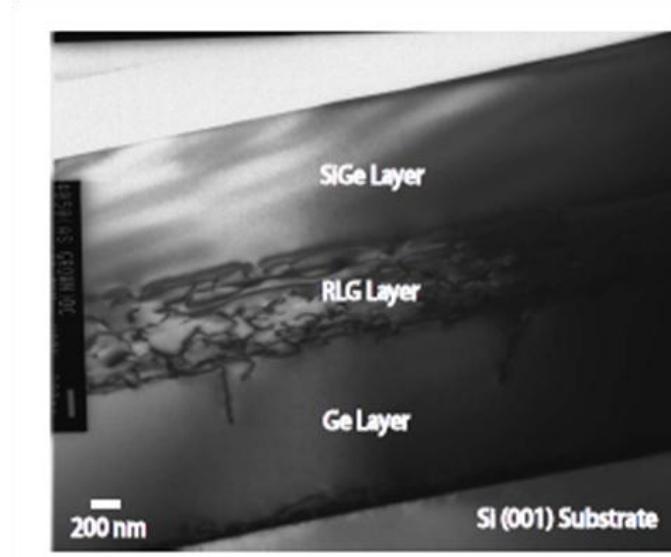
Figure 3.6 XTEM image of the $Si_{0.2}Ge_{0.8}$/RLG SiGe/Ge/Si(001) virtual substrate [17].

3.4.3.2 X-Ray Diffraction

(004) $\omega - 2\theta$ scan and an asymmetrical (224) RSM measurements using the XRD system, X'pert MRD, (described in 3.3.2), were performed to determine structural parameters of the relaxed $Si_{0.2}Ge_{0.8}$ virtual substrate such as the crystal lattice constants, strain, and relaxation. Figure 3.7 shows a (004) $\omega - 2\theta$ scan rocking curve and an asymmetrical (224) RSM image of the $Si_{0.2}Ge_{0.8}$ virtual substrate, in which the peaks of the Si(001) substrate, constant composition $Si_{0.2}Ge_{0.8}$ layer, and Ge interlayer are observed. The continuous intensity between the $Si_{0.2}Ge_{0.8}$ and Ge peaks originates from the 800-nm-thick RLG $Si_{1-x}Ge_x$ layer (from x=1 down to x=0.8). Table 3.2 summarizes the structural properties of the constant SiGe layer on the top, calculated by inserting the peak values obtained from the rocking curve and RSM image into the equations shown in 3.3. As expected, the Ge content of the constant composition SiGe layer is found to be 80% from the RSM observation. The vertical lattice constant, $a_\perp$, of the constant SiGe layer is consistent between the two method. From Eqs. (3.19) and (3.20),

the lattice constant of a fully relaxed $Si_{0.2}Ge_{0.8}$ crystal is calculated to be $a_{SiGe} = 5.608$ Å. From the values of a_{SiGe} and $a_{\parallel}$, the in-plane strain of the constant SiGe layer was found to be 0.02%. Furthermore, the relaxation was measured to be 107% relative to the Si(001) substrate. The XRD observations confirm that the constant composition $Si_{0.2}Ge_{0.8}$ layer is almost fully relaxed.
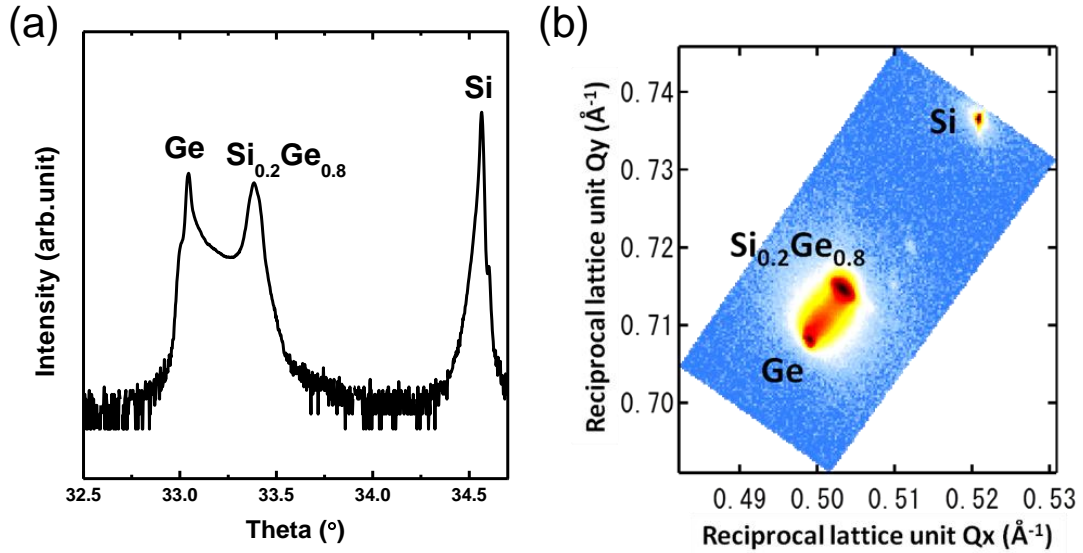
Figure 3.7 (a) (004) $\omega - 2\theta$ scan rocking curve and (b) asymmetrical (224) RSM of the SiGe virtual substrate employed in this experiment.

Table 3.2   Structural properties of the constant composition SiGe layer in the virtual substrate obtained by XRD observations.

(004) $\omega - 2\theta$ scan	Asymmetrical (224) RSM	
$a_{\perp}$ (Å)	$[a_{\parallel}, a_{\perp}]$ (Å)	Ge content (%)
5.600	[5.620, 5.598]	79.7

3.4.3.3   Atomic Force Microscopy

Atomic force microscopy (AFM) observations were performed to evaluate the sample surface condition with a SPA 300/SPI 3800N AFM (Seiko). Figure 3.8 shows an AFM image of the topmost surface of the relaxed $Si_{0.2}Ge_{0.8}$ virtual substrate. The scan area is 10×10 µm². A cross-hatch pattern is observed in the image. This cross-hatch pattern is typical of graded structures due to the strain field generated by misfit dislocations running in orthogonal directions during growth of the graded layer. The measured average of the surface RMS (root-mean-square) roughness was 1.4 nm. The small RSM value indicates that the sample surface is enough smooth to grow s-Ge layers on the virtual substrate.
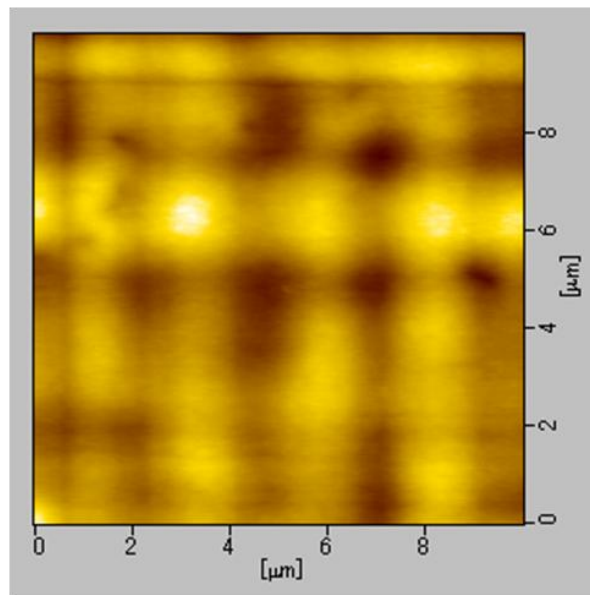
Figure 3.8 AFM image of the topmost surface of the $Si_{0.2}Ge_{0.8}$ virtual substrate. The scan area is 10×10 µm². The surface RMS roughness is found to be 1.4 nm

3.5   Growth of Biaxial Compressive Strained Germanium Isotope Supperlattice

3.5.1   MBE Growth Condition of Silicon-Germanium

Growth of a biaxial compressive s-Ge isotope SL was achieved by sandwiching a Ge isotope SL by relaxed SiGe layers, i.e., a relaxed SiGe/s-Ge isotope SL/relaxed SiGe heterostructure. In this section, the growth method, procedure and the structural analysis of the heterostructure are presented.

A ^{nat}Ge/^{70}Ge isotope SL composed of alternating layers of ^{nat}Ge and isotopically enriched ^{70}Ge was grown on the ^{nat}Si$_{0.2}$^{nat}Ge$_{0.8}$ virtual substrate, characterized in 3.4, by solid-source molecular beam epitaxy (MBE) (described in 2.4). A ^{nat}Si$_{0.2}$^{nat}Ge$_{0.8}$ buffer layer was MBE-grown on the ^{nat}Si$_{0.2}$^{nat}Ge$_{0.8}$ virtual substrate prior to the growth of the Ge isotope SL, in order to obtain an atomically smooth surface and avoid contaminating the Ge isotope SL by means of embedding impurities adsorbing onto the air-exposed surface. The abundances of the sources used for the MBE growth are ^{70}Ge: 20.5%, ^{72}Ge: 27.4%, ^{73}Ge: 7.8%, ^{74}Ge: 36.5%, and ^{76}Ge: 7.8% for ^{nat}Ge, ^{28}Si: 92.2%, ^{29}Si: 4.7%, and ^{30}Si: 3.1% for ^{nat}Si, and ^{70}Ge: 96.3%, ^{72}Ge: 2.1%, ^{73}Ge: 0.1%, ^{74}Ge: 1.2%, and ^{76}Ge: 0.3% for ^{70}Ge, respectively. The composition x of ^{nat}Si$_{1-x}$^{nat}Ge$_x$ of the buffer layer was controlled by the ^{nat}Si and ^{nat}Ge K-cell temperatures in the MBE growth system. To obtain the composition x as a function of the ^{nat}Ge K-cell temperature, multilayer structures of ^{nat}Si$_{1-x}$^{nat}Ge$_x$ with different x were grown on (001)-oriented Ge substrates by keeping the ^{nat}Si K-cell temperature constant at 1440 °C and gradually changing the ^{nat}Ge K-cell temperature between 1080 and 1170 °C. The temperature of the substrate was kept at 250 °C during the MBE growth and rotated with a constant speed. The compositions x of the ^{nat}Si$_{1-x}$^{nat}Ge$_x$ multilayer structures were determined by measuring the concentration profiles of Si and Ge in the samples by secondary ion mass spectroscopy (SIMS) with a PHI ADEPT-1010 microscopy. Figure 3.9 shows ^{nat}Si$_{1-x}$^{nat}Ge$_x$ composition x as a function of the ^{nat}Ge K-cell temperature. From this figure, the ^{nat}Ge K-cell temperature for the ^{nat}Si$_{0.2}$^{nat}Ge$_{0.8}$ growth was determined to be 1105 °C. Furthermore, the growth rate of ^{nat}Si$_{0.2}$^{nat}Ge$_{0.8}$ at the ^{nat}Si (1440 °C) and ^{nat}Ge
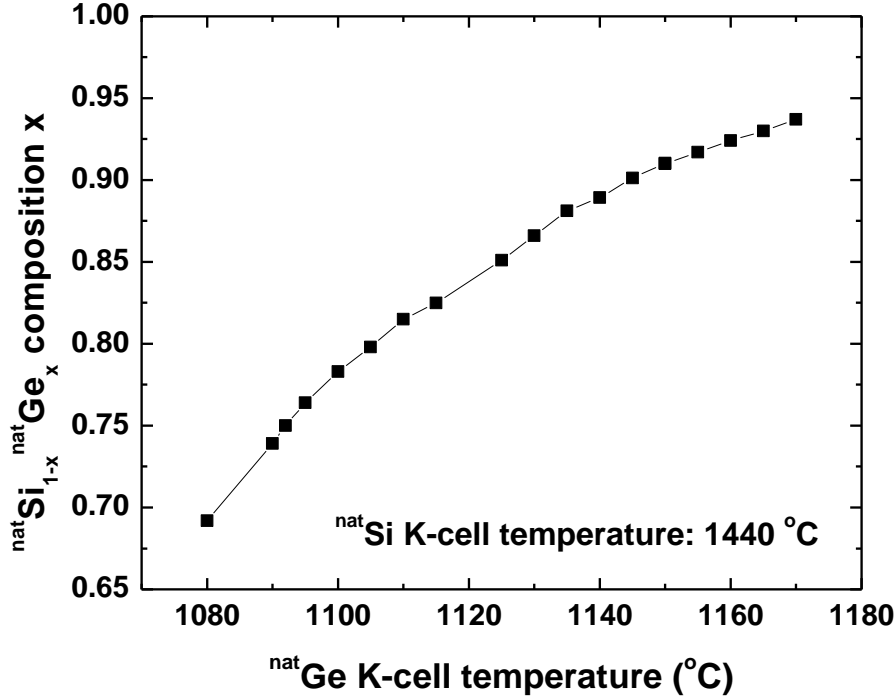
Figure 3.9 $^{nat}Si_{1-x}{}^{nat}Ge_x$ composition x as a function of the ^{nat}Ge K-cell temperature in the MBE growth system. The ^{nat}Si K-cell temperature is constant at 1440 °C during growth.

(1105 °C) K-cell temperatures was determined to be 0.378 nm/min.

We also confirmed that the composition of the $^{nat}Si_{0.2}{}^{nat}Ge_{0.8}$ buffer layer grown by MBE agreed with that of the virtual substrate grown by CVD, by growing a single $^{nat}Si_{0.2}{}^{nat}Ge_{0.8}$ layer on a Ge(001) substrate at the ^{nat}Si (1440 °C) and ^{nat}Ge (1105 °C) K-cell temperatures followed by an asymmetric (224) RSM analysis.

Moreover, the $^{nat}Si_{0.2}{}^{nat}Ge_{0.8}$ buffer layer was grown on the $^{nat}Si_{0.2}{}^{nat}Ge_{0.8}$ virtual substrate and the top surface was imaged by AFM (SPA 300). The surface RMS roughness was found to be 1.4 nm after the buffer growth. This indicates that threading dislocation density reaching the top surface was kept to the minimum ($\sim 4 \times 10^6 \, cm^{-2}$).

3.5.2   Growth Procedure and Sample Structure

In order to chemically clean the surface of the $^{nat}Si_{0.2}{}^{nat}Ge_{0.8}$ virtual substrate, the substrate was dipped in distilled water for 5 min. Then the substrate was cleaned by hydrofluoric acid (HF) treatment for 15 sec followed by thorough rinse with distilled water for 3 min. This process repeated 3 times. Figure 3.10 shows a schematic illustration of the relaxed $^{nat}Si_{0.2}{}^{nat}Ge_{0.8}$/biaxial compressive s-Ge isotope SL/relaxed $^{nat}Si_{0.2}{}^{nat}Ge_{0.8}$ heterostructure fabricated in this work. Firstly, a 50-nm-thick $^{nat}Si_{0.2}{}^{nat}Ge_{0.8}$ buffer layer was MBE-grown on the $^{nat}Si_{0.2}{}^{nat}Ge_{0.8}$ virtual substrate by using the ^{nat}Si K-cell temperature of 1440 °C and the ^{nat}Ge K-cell temperature of 1105 °C, and the growth rate determined in 3.5.1. The MBE growth of a Ge isotope SL consisting of alternating layers of ^{70}Ge and ^{nat}Ge was performed on the $^{nat}Si_{0.2}{}^{nat}Ge_{0.8}$ buffer layer by using the ^{nat}Ge and ^{70}Ge K-cell temperatures of 1150 °C and the growth rate determined in 2.6.1. The thickness of each layer was 8 nm. Finally, a 50-nm-thick relaxed $^{nat}Si_{0.2}{}^{nat}Ge_{0.8}$ cap layer was MBE-grown on the top as a stressor by using the same ^{nat}Si and ^{nat}Ge K-cell temperatures as for the buffer layer. Two ^{nat}Ge (10 nm) barrier layers sandwiching the Ge isotope SL were inserted to avoid interdiffused Si reaching the Ge isotope SL during diffusion annealing. The total thickness of the strained Ge layer was 60 nm including the Ge isotope SL and barrier layers. The temperature of the $Si_{0.2}Ge_{0.8}$ virtual substrate during the MBE growth was 250 °C and the substrates were rotated with a same constant speed.

In addition, an unstrained Ge isotope SL, a simple $^{nat}Ge(8nm)/^{70}Ge(8nm)$ SL grown on a (001)-oriented Ge substrate [18–21], was also fabricated to observe self-diffusion in unstrained Ge as a control. The unstrained Ge SL was grown under the same growth conditions as the s-Ge SL.
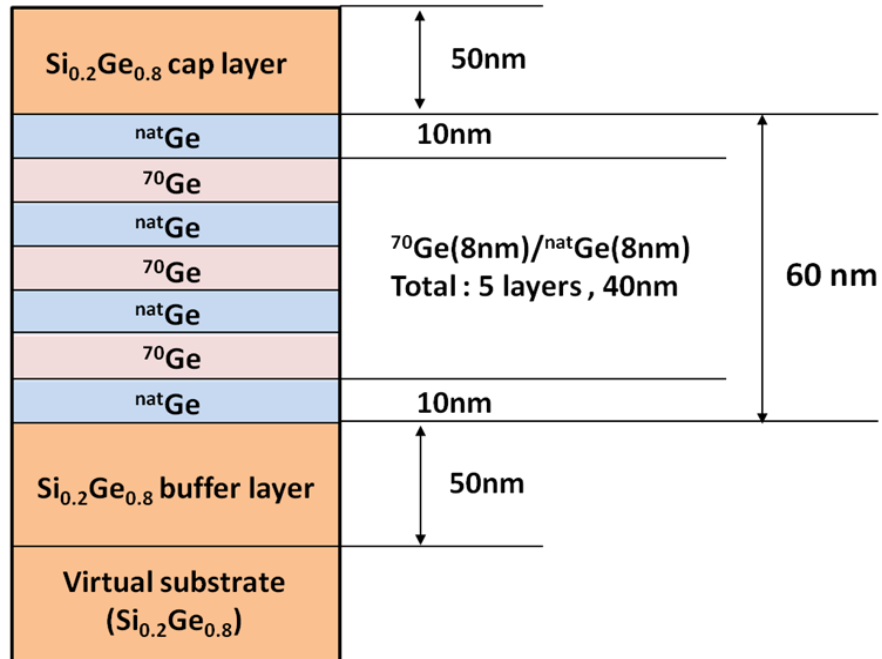
Figure 3.10 Schematic illustration of the relaxed [nat]$Si_{0.2}$[nat]$Ge_{0.8}$ (50 nm)/biaxial compressive s-Ge isotope SL (60 nm)/relaxed [nat]$Si_{0.2}$[nat]$Ge_{0.8}$ heterostructure fabricated in this work.

3.5.3   Characterization: SIMS, XRD, TEM, AFM

3.5.3.1   Secondary Ion Mass Spectroscopy

The heterostructure sample was measured by SIMS with PHI ADEPT-1010 for Ge self-diffusion evaluation. Figure 3.11 shows the depth profile of ^{74}Ge in the as-grown heterostructure in SIMS intensity. A periodicity of ^{74}Ge was observed in the s-Ge isotope SL sandwiched by the relaxed $Si_{0.2}Ge_{0.8}$ layers. The Si and Ge contents in the heterostructure quantified by using SIMS

standard samples of $Si_{0.2}Ge_{0.8}$ and Ge (x=1), respectively, are also shown in the figure. As predicted, a Ge (Si) content of approximately 80% (20%) in the SiGe cap and buffer layers was obtained. The thicknesses of the SiGe cap and s-Ge layers were measured to be approximately 50 and 60 nm, respectively. Note that the intensity of ^{74}Ge in the $Si_{0.2}Ge_{0.8}$ layers is higher than that in the s-Ge layer because of the inherent high SIMS sensitivity of Ge in SiGe compared to that in Ge. For simulation, the intensity of Ge in SiGe is calibrated to be 80% relative to that in s-Ge to avoid overestimating Ge inter-diffusion from SiGe into s-Ge.
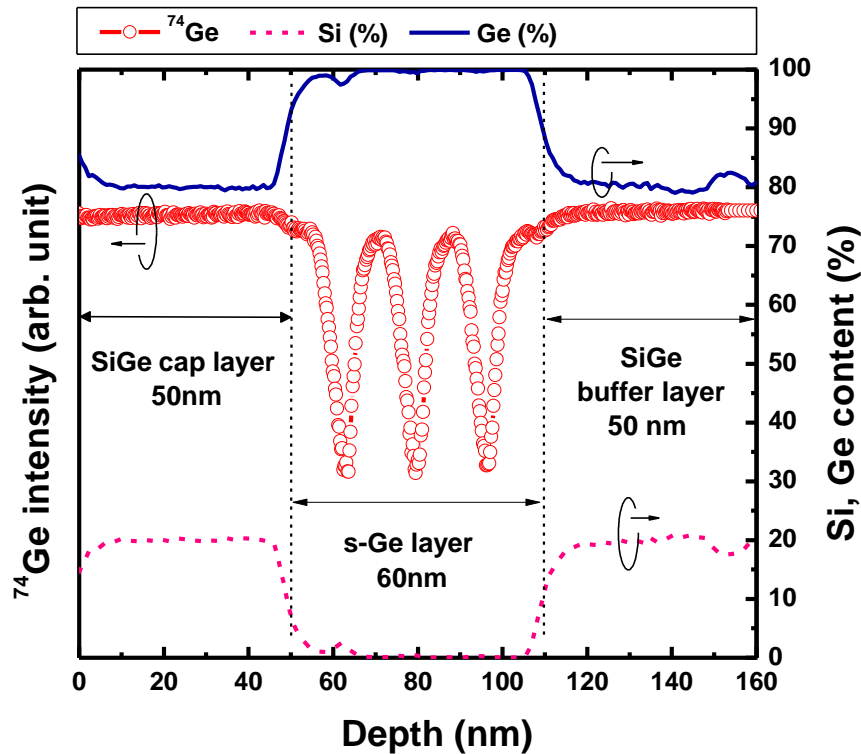
Figure 3.11 Depth profiles of ^{74}Ge (solid symbols) in SIMS intensity, and Si (dashed line) and Ge (solid line) in content (%). The ^{74}Ge intensity corresponds to the left vertical axis. The Si and Ge contents correspond to the right vertical axis.

3.5.3.2   X-Ray Diffraction

The structural properties such as the lattice constants, strain, relaxation, and composition of the heterostructure were determined by (004) $\omega - 2\theta$ scan and asymmetrical (224) RSM measurements using the XRD system, X'pert MRD. Figure 3.12(a) shows the (004) $\omega - 2\theta$ scan rocking curves before and after the MBE growth of the heterostructure. The peak of the s-Ge layer was observed after the growth. The peak broadening of s-Ge was observed due to its small thickness (~60 nm), according to Scherrer's Formula [22]. The asymmetrical (224) RSM image of the sample after the heterostructure growth is displayed in Fig. 3.12(b), in which the peaks of the Si(001) substrate, constant composition SiGe layers, Ge interlayer, and s-Ge isotope SL were observed. Tables 3.3–3.5 summarize the quantitative values of the structural properties of the constant composition $Si_{0.2}Ge_{0.8}$ and s-Ge layers determined from these XRD measurements. The vertical lattice constants of the constant composition $Si_{0.2}Ge_{0.8}$ and s-Ge layers are consistent between the two methods. A good agreement between the in-plane lattice constant values of the s-Ge and relaxed $Si_{0.2}Ge_{0.8}$ layers was obtained The in-plane relaxation of the s-Ge SL compared to the underlying relaxed $Si_{0.2}Ge_{0.8}$ layer was calculated to be 6.0%. There results confirm that the s-Ge isotope SL was almost fully strained relative to the $Si_{0.2}Ge_{0.8}$ layer. The biaxial compressive strain of 0.71 % was obtained from the s-Ge isotope SL relative to unstrained Ge. This strain corresponds to an in-plane stress of 0.95 GPa.

(a)

(b)
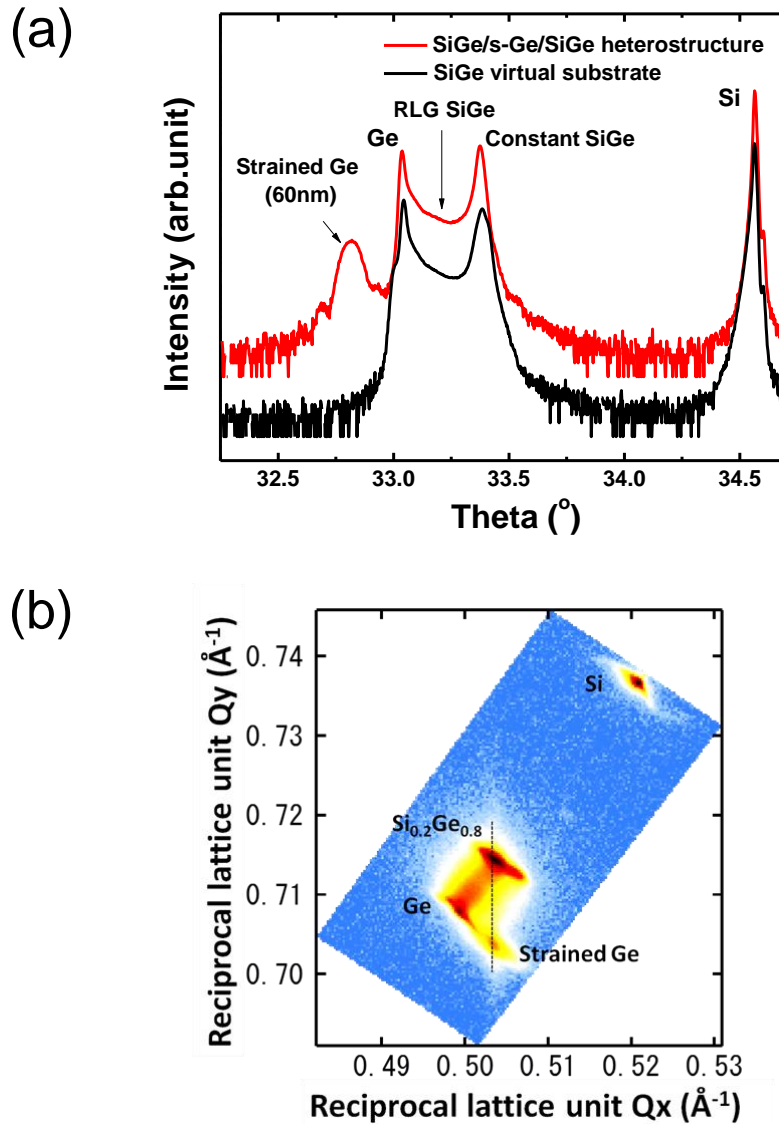
Figure 3.12 (a) (004) $\omega - 2\theta$ scan rocking curve before (lower) and after (upper) the MBE growth of the relaxed $^{nat}Si_{0.2}^{nat}Ge_{0.8}$/s-Ge isotope SL/relaxed $^{nat}Si_{0.2}^{nat}Ge_{0.8}$ heterostructure. (b) Asymmetrical (224) RSM of the sample.

Table 3.3 Vertical lattice constants of the constant composition SiGe and s-Ge layers obtained from the (004) $\omega - 2\theta$ scan rocking curve.

	SiGe	s-Ge
$a_\perp$ (Å)	5.601	5.685

Table 3.4 Structual properties of the constant composition SiGe layers determined from the asymmetrical (224) RSM.

$[a_\parallel,\ a_\perp]$ (Å)	[5.615, 5.602]
Ge content (%)	79.6
a_{SiGe} (Å)	5.608
Relaxation to Si (%)	104

Table 3.5 Structual properties of the s-Ge layer determined from the asymmetrical (224) RSM.

$[a_\parallel,\ a_\perp]$ (Å)	[5.617, 5.685]
$\varepsilon_\parallel$ to Ge (%)	0.71
Relaxation to $Si_{0.2}Ge_{0.8}$ buffer (%)	6.0

3.5.3.3 Transmission Electron Microscopy and Atomic Force Microscopy

Finally, the sample was examined with XTEM with a JEM-2100 F TEM accelerating at 200 kV and AFM with a Seiko SPA300/SPI3800N AFM using a NC-10T Arrow NC crystalline silicon probe (NanoWorld Inc.) to evaluate the dislocation density and surface condition. Figure 3.13(a) shows a XTEM image of the heterostructure. The actual thicknesses of the relaxed SiGe cap, s-Ge, and relaxed SiGe buffer layers were measured to be 50, 60, and 50 nm, respectively. The XTEM observation confirmed that the low threading dislocation density reaching the top surface ($\sim$4$\times$10^6 cm^{-2}) remained throughout the MBE growth of the heterostructure. The AFM image of the top surface is displayed in Fig. 3.13(b). The scan area is 10 $\times$ 10 μm^2. The surface RMS roughness was measured to be 1.7 nm. These observations show that we achieved growth of a high quality s-Ge isotope SL with low threading dislocation density and small surface roughness.

(a)

(b)
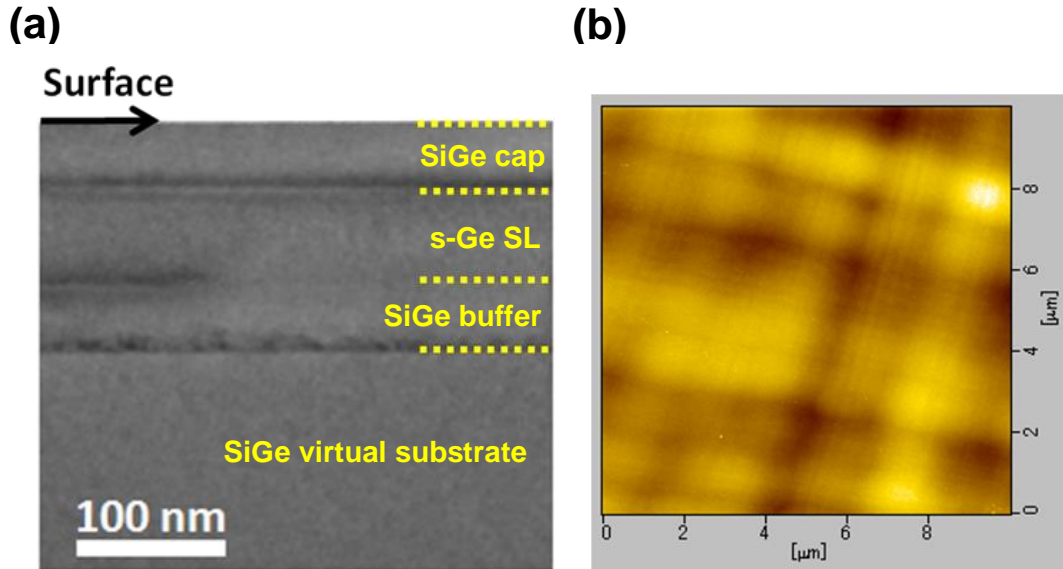
Figure 3.13 (a) XTEM image of the relaxed $^{nat}Si_{0.2}{}^{nat}Ge_{0.8}$ / s-Ge isotope SL / relaxed $^{nat}Si_{0.2}{}^{nat}Ge_{0.8}$ heterostructure grown by MBE. (b) AFM image of the top surface of the sample. The scan area is 10×10 µm². The surface RMS roughness was measured to be 1.7 nm.

3.6   Diffusion Annealing

3.6.1   Annealing Procedure

Figure 3.14(a) shows a picture of a resistive furnace at our group that was used in this experiment. The furnace can provide maximum temperature of 1500 °C. Figure 3.14(b) shows a picture of the samples placed on a quartz boat located at the edge of the quartz tube of the furnace. The quartz boat was equipped with a quartz port at the edge. The samples placed on the quartz boat were inserted into the middle of the furnace by using the quartz port. In order to measure the sample temperature during annealing, a well-calibrated thermocouple in the quartz port was placed right below the samples. The temperature was monitored and recorded by a PC shown in Fig. 3.14(a) throughout annealing. The fluctuation of temperature was found to be less than

±2 °C. Figure 3.14(c) displays a picture of a Si wafer in which 3 thermocouples are embedded at regular intervals. The temperature that the thermocouple placed below the samples indicates was calibrated by comparing it to the actual sample temperature monitored with the thermocouples embedded in the Si wafer.

The Ge isotope SL sample characterized in 3.5 was cut into a number of smaller pieces and they were annealed at various diffusion temperatures between 475 and 600 °C for 0.5–61 h in the resistively heated furnace under a flow of 99.999% Ar at 1.3 l/min. As shown in Fig. 3.14(b), the samples were placed face to face with bulk Ge samples in order to avoid Ge loss from the surface during diffusion annealing. All the samples were cleaned by using the procedure described in 3.5.2.

(a)

(b)

(c)
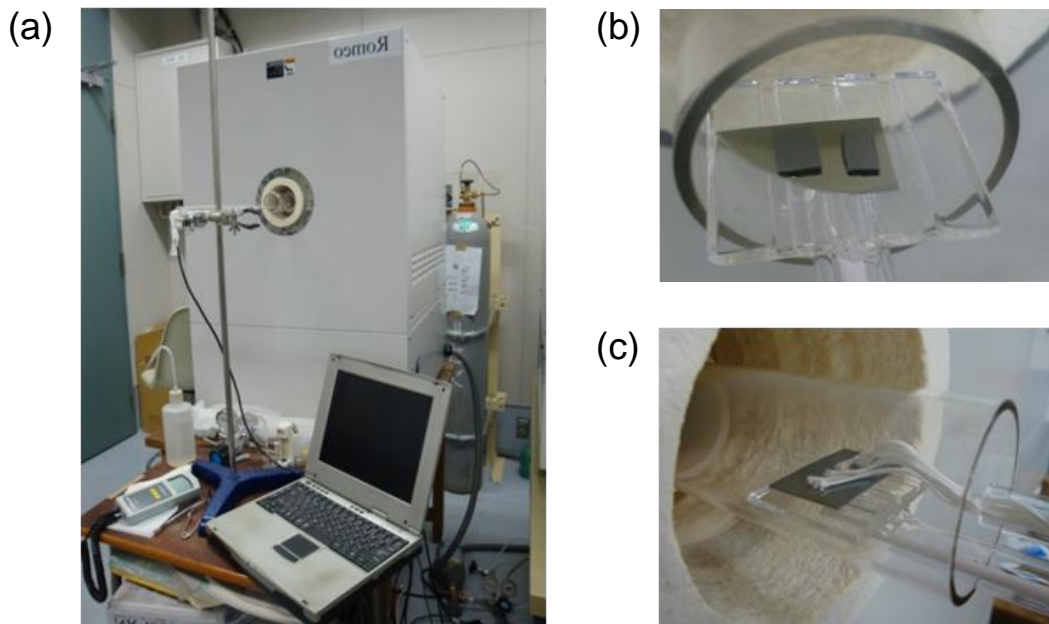
Figure 3.14 (a) Resistive furnace employed in this work. (b) Samples placed on a quartz boat located at the edge of the quartz tube of the furnace. The samples were placed face to face with bulk Ge samples in order to avoid Ge loss from the surface during diffusion annealing. (c) Si wafer in which 3 thermocouples are embedded at regular intervals for monitoring the actual sample temperature.

3.6.2   Strain Analysis after Diffusion Annealing

Structural properties such as the lattice constants, strain, relaxation, and composition of the heterostructure after diffusion annealing were also determined by (004) $\omega - 2\theta$ scan and asymmetrical (224) RSM measurements using XRD. Figure 3.15 shows the (004) $\omega - 2\theta$ scan rocking curves of the samples before and after diffusion annealing at 550 °C for 1, 3, and 6 h. These data show an excellent agreement between the intensity peak position of the s-Ge layer before and after the diffusion annealings. From the RSM data shown in Fig. 3.16, compressive strain of the s-Ge layer after the diffusion annealings at 550 °C was found to be 0.71% for 1 h, 0.68% for 3 h, and 0.66% for 6 h, which is well within the 8% relaxation compared to the initial strain (0.71%). XTEM observations with a JEM-2100 F TEM operating at 200 kV before and after the diffusion annealings (Figure 3.17) showed that the low threading dislocation densities of 4×10^6 cm^{-2} remained constant during the annealings. Importantly, these results confirm that the heterostructure remained pseudomorphic to the underlying $Si_{0.2}Ge_{0.8}$ layers throughout the diffusion annealings.
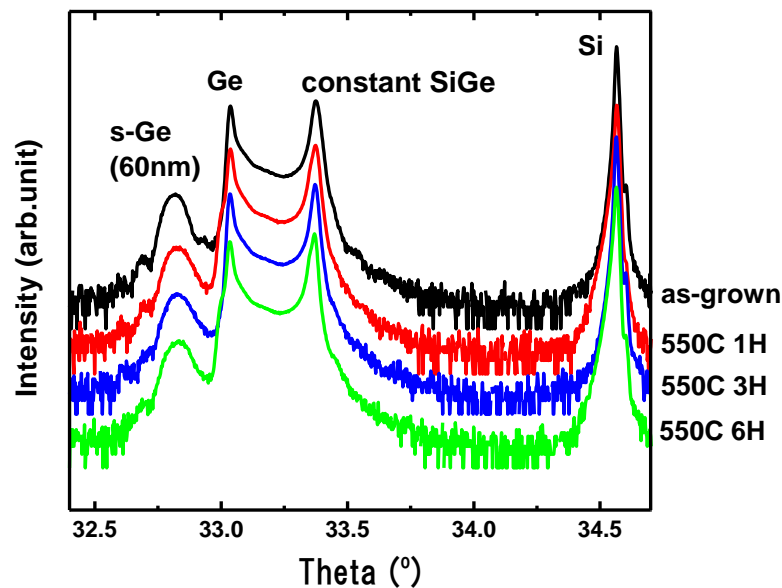
Figure 3.15 (004) $\omega - 2\theta$ scan rocking curves of the samples before and after diffusion annealing at 550 °C for 1h, 3h, and 6h.
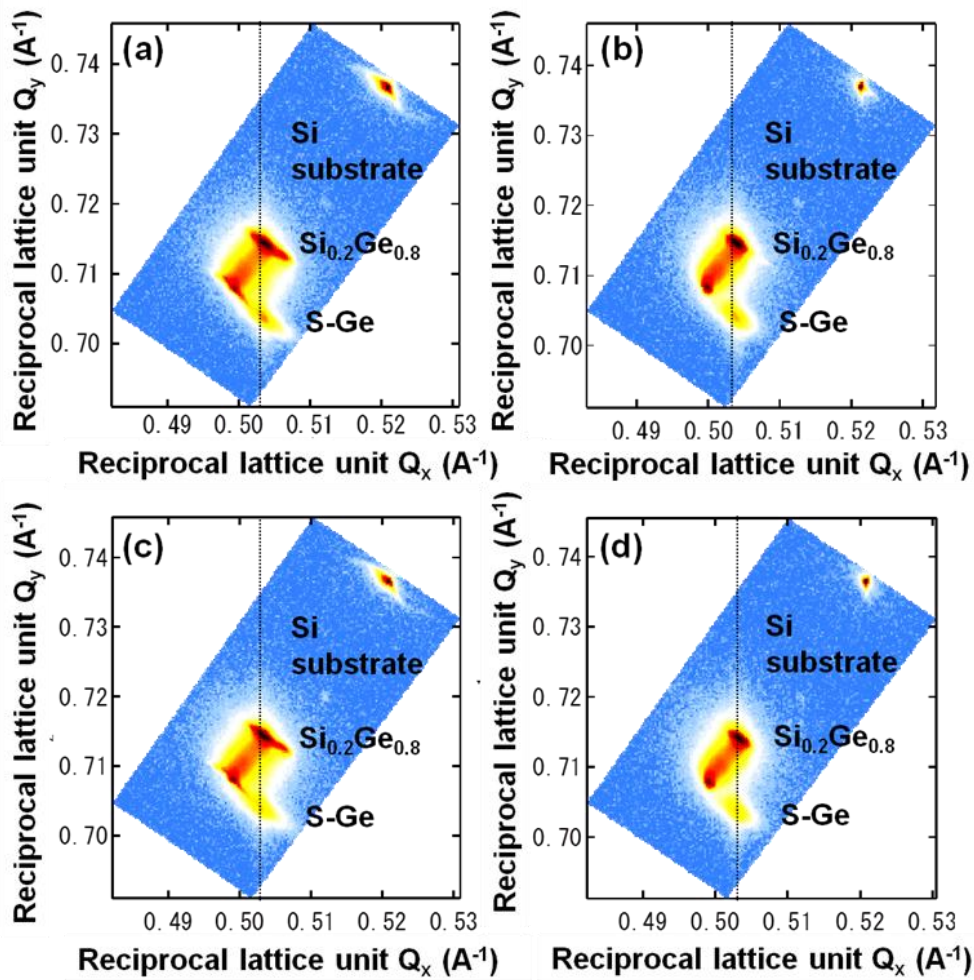
Figure 3.16 Intensity peaks of the Si substrate, relaxed $Si_{0.2}Ge_{0.8}$ layers, and compressively s-Ge layers examined with asymmetrical (224) RSM using XRD system (a) before and after annealing at 550 ^{o}C for (b) 1 h, (c) 3 h, and (d) 6 h.

Figure 3.17 XTEM images of the samples (from the surface, the relaxed $Si_{0.2}Ge_{0.8}$ cap layer, compressively s-Ge isotope SL, $Si_{0.2}Ge_{0.8}$ buffer layer, and $Si_{0.2}Ge_{0.8}$ virtual substrate) (a) before and after diffusion annealing at 550 °C for (b) 1 h, (c) 3 h, and (d) 6 h.

3.7 Self-Diffusion in Germanium under Biaxial Compressive Strain

3.7.1 Self-Diffusion Model

The depth profiles of concentration of isotope ^{74}Ge in the compressively s-Ge isotope SL before and after diffusion annealing were measured by SIMS. The Ge self-diffusivities in compressively s-Ge were determined by fitting the SIMS depth profiles by using a partial differential equation solver, ZOMBIE [23]. In this section, a self-diffusion model utilized for the ZOMBIE simulation is

presented.

As detailed in 3.2, self-diffusion in Ge takes place by simply vacancies. We simulated the ^{74}Ge profiles according to the vacancy mechanism. The self-diffusion reaction can be described as:

$$^{74}V \Leftrightarrow {}^{74}Ge_s + V, \tag{3.28}$$

where V and ^{74}V represent the V of ^{70}Ge (matrix) and ^{74}Ge (diffusing atom), respectively. ^{74}Ge$_s$ represents a substitutional ^{74}Ge. The reaction leads to the following set of coupled partial differential equations:

$$\frac{\partial C_{^{74}Ge_s}}{\partial t} = G \tag{3.29}$$

$$\frac{\partial C_{^{74}V}}{\partial t} = \frac{\partial}{\partial x}\left(D_{^{74}V}\frac{\partial C_{^{74}V}}{\partial x}\right) - G \tag{3.30}$$

$$\frac{\partial C_V}{\partial t} = \frac{\partial}{\partial x}\left(D_V\frac{\partial C_V}{\partial x}\right) + G \tag{3.31}$$

where C_x ($x = {}^{74}Ge_s$, ^{74}V, and V) is the concentration of x, and D_x is the diffusivity of x. G represents the generation term:

$$G = k_f C_{^{74}V} - k_b C_{^{74}Ge_s} C_V \tag{3.32}$$

where k_f and k_b, respectively, are the rate constants donating forward and backward directions. Eqs. $(3.29) - (3.31)$ were solved numerically by ZOMBIE.

3.7.2   Determination of Germanium Self-Diffusivities

Figure 3.18 shows the depth profiles of ^{74}Ge in the heterostructure of the samples measured by SIMS using a PHIADEPT1010 with a Cs$^+$ primary ion beam accelerated at 1.0 kV before and after annealing at 550 °C for 1–6 h along with the simulation results by ZOMBIE. We obtained a Ge self-diffusivity value of 6.40×10^{-18} cm^2/s for this case. Figure 3.19 compares the temperature dependencies of the Ge self-diffusivities in the strained and unstrained Ge obtained in this work. The Ge self-diffusivities in the unstrained Ge agree with

those obtained for bulk Ge reported in Ref. 15. The experimentally obtained Ge self-diffusivities are described by the Arrhenius expression shown in Eq. (3.9). In this study, D_0^{SD}=35.8 cm²/s and H^{SD}=3.07 eV for compressively s-Ge, and D_0^{SD}=17.1 cm²/s and H^{SD}=3.11 eV for unstrained Ge were obtained. The latter set of values agrees with D_0^{SD}=25.4 cm²/s and H^{SD}=3.13 eV reported for bulk Ge in the temperature range of 429 to 904 °C [15]. Therefore, the enhancement of the Ge self-diffusivity by a factor of 3.5 due to the compressive biaxial strain of 0.71% is experimentally established in the temperature range of 475 to 600 °C. Annealing at higher temperatures introduces the relaxation of s-Ge and at lower temperatures does not induce a large enough change in the ^{74}Ge concentration profile for SIMS evaluation.
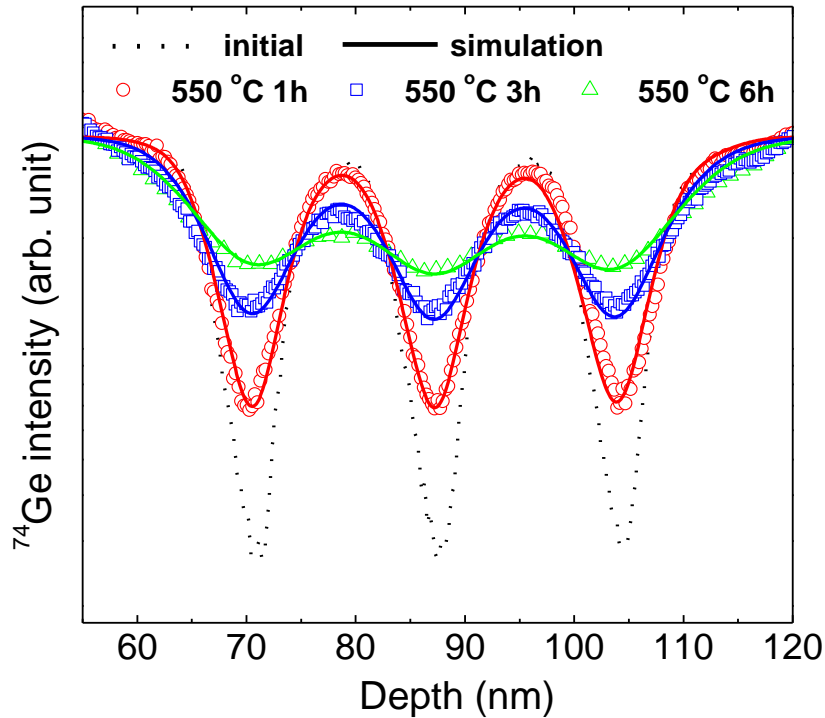
Figure 3.18 SIMS and simulated depth profiles of ^{74}Ge in the relaxed Si$_{0.2}$Ge$_{0.8}$ / s-Ge isotope SL / relaxed Si$_{0.2}$Ge$_{0.8}$ heterostructures. Dashed line, open circles, open squares, and open triangles represent the SIMS depth profiles before and after annealing at 550 ᵒC for 1, 3 and 6 h, respectively. Solid curves are the simulation results.
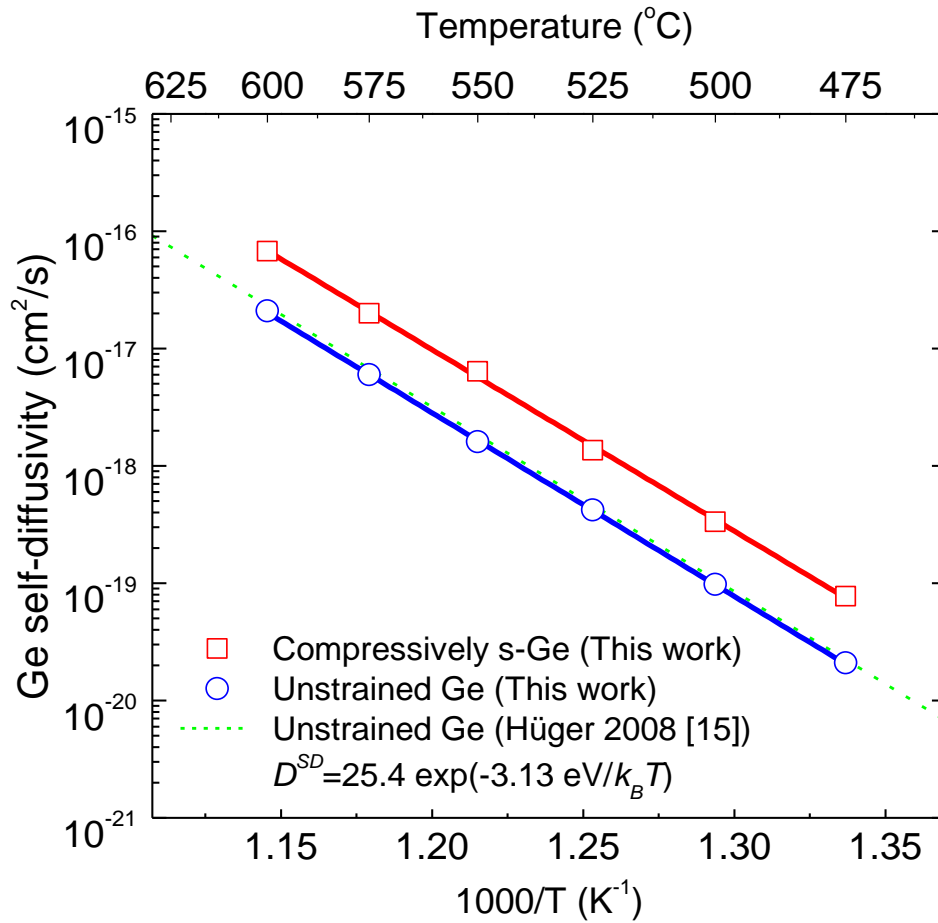
Figure 3.19 Temperature dependences of Ge self-diffusivities in compressively strained and unstrained Ge. The open squares and open circles, respectively, represent the temperature dependences of Ge self-diffusivities in compressively strained and unstrained Ge obtained in this work. The solid lines show the best fits based on an Arrhenius expression. The dashed line represents the temperature dependence of Ge self-diffusivities in unstrained Ge reported in Ref. 15.

3.7.3   Discussion: Activation Volume Model

In this section, the origin of the enhancement by a factor of 3.5 is discussed. It is well-established that Ge self-diffusion in unstrained Ge is mediated by the simple vacancy mechanism [15, 21, 24, 25]. The similarity between the activation enthalpy of s-Ge and that of unstrained Ge, as shown in Fig. 3.19, allows us to assume that the simple vacancy mechanism is also responsible for Ge self-diffusion in Ge with a compressive biaxial strain of 0.71%. The effect of biaxial strain on diffusivity has been characterized by the change in activation enthalpy, Q' with biaxial strain, ε_{biax} [9–12, 26, 27],

$$Q' = -k_B T \frac{\partial \ln D^{SD}}{\partial \varepsilon_{biax}} \bigg|_T . \qquad (3.33)$$

By employing Eq. (3.33) and our self-diffusivities, we deduced the change in the activation enthalpy of $Q' = -13 \pm 4$ eV per unit compressive strain. For Sb diffusion, Kringhøj *et al.* [26] reported $Q' = -13 \pm 3$ eV per unit strain for compressively strained $Si_{0.91}Ge_{0.09}$ and $Q' = -17 \pm 5$ eV for tensile Si. The similarity of the activation enthalpy of Sb to that of Ge is understandable since they both diffuse via the simple vacancy mechanism [4].

Moreover, it has been proposed that the effect of stress (pressure) on diffusion in solids can be thermodynamically treated by the concept of an activation volume [10−12, 24, 28, 29]. The change in the activation enthalpy with compressive strain can be explained by the activation volume based on the behavior of native point defects. From transition state theory, self-diffusivity can be written as [11, 12, 28, 29],

$$D^{SD} = \gamma a^2 v f \exp\left(-\frac{G^{SD}}{k_B T}\right), \qquad (3.34)$$

where γ is the geometrical constant, a is the lattice parameter, v is the attempt frequency, and f is the correlation factor. Here, G^{SD} is the Gibbs free energy of point defects responsible for the self-diffusion processes and described as

$$G^{SD} = H^{SD} - TS^{SD}, \qquad (3.35)$$

with the activation entropy S^{SD}. From Eqs. (3.9), (3.34), and (3.35), the pre-exponential factor D_0^{SD} in Eq. (3.9) can be described including S^{SD} as

$$D_0^{SD} = \gamma a^2 v f \exp\left(-\frac{S^{SD}}{k_B}\right). \tag{3.36}$$

In addition, the activation enthalpy H^{SD} is given by

$$H^{SD} = E_a^{SD} + pV^{SD}. \tag{3.37}$$

Here, p is the hydrostatic pressure, and E_a^{SD} is the activation energy for self-diffusion. H^{SD} at atmospheric pressure is a good approximation equal to. E_a^{SD}. From Eqs. (3.34), (3.35) and (3.37), the activation volume can be given by the pressure derivative of the Gibbs free energy for self-diffusion:

$$V^{SD} = \left.\frac{\partial G^{SD}}{\partial p}\right|_T. \tag{3.38}$$

In addition, the pressure derivative of self-diffusivity is described as

$$k_B T \left.\frac{\partial \ln D^{SD}}{\partial p}\right|_T = k_B T \left.\frac{\partial \ln(\gamma a^2 v f)}{\partial p}\right|_T - \left.\frac{\partial G^{SD}}{\partial p}\right|_T. \tag{3.39}$$

Since the first term on the right hand side of Eq. (3.39) represents a small correction well within a few percent of V^{SD}, the observed increase in D^{SD} with p is attributable to the activation volume term [24, 28, 29]. Therefore, V^{SD} can be described by

$$V^{SD} = -k_B T \left.\frac{\partial \ln D^{SD}}{\partial p}\right|_T, \tag{3.40}$$

and becomes positive (negative) when D^{SD} decreases (increases) with p. For the case of the vacancy mechanism, V^{SD} is the sum of two components:

$$V^{SD} = V^F + V^M, \tag{3.41}$$

where the formation volume, V^F, is the volume change of the system upon formation of a vacancy in its standard state, and the migration volume, V^M, is the additional volume change when the vacancy reaches the saddle point in its

migration path [10−12, 24]. V^F and V^M for a simple vacancy mechanism are schematically shown in Fig. 3.20. For a (001) thin-film geometry, the predominant source of vacancies is the free surface [10−12]. When a vacancy is created in crystalline Ge, one Ge atom leaves a lattice site and migrates to the surface. The resulting increase of the crystal volume corresponding to one Ge atomic volume (Ω_{Ge}) is 2.26×10^{-29} m^3/atom [30]. However, V^F depends on the degree to which the atoms surrounding the vacancy relax toward the vacancy center. Thus, V^{SD} is decreased by the relaxation volume (V^R) which takes a negative value. In addition, V^M is also negative due to the fact that the diffusing atom via a vacancy is expanding a constriction at the saddle point in its migration path [24]. Then, the activation volume of the Ge self-diffusion under hydrostatic pressure is described as

$$V^{SD} = \Omega_{Ge} + V^R + V^M, \tag{3.42}$$
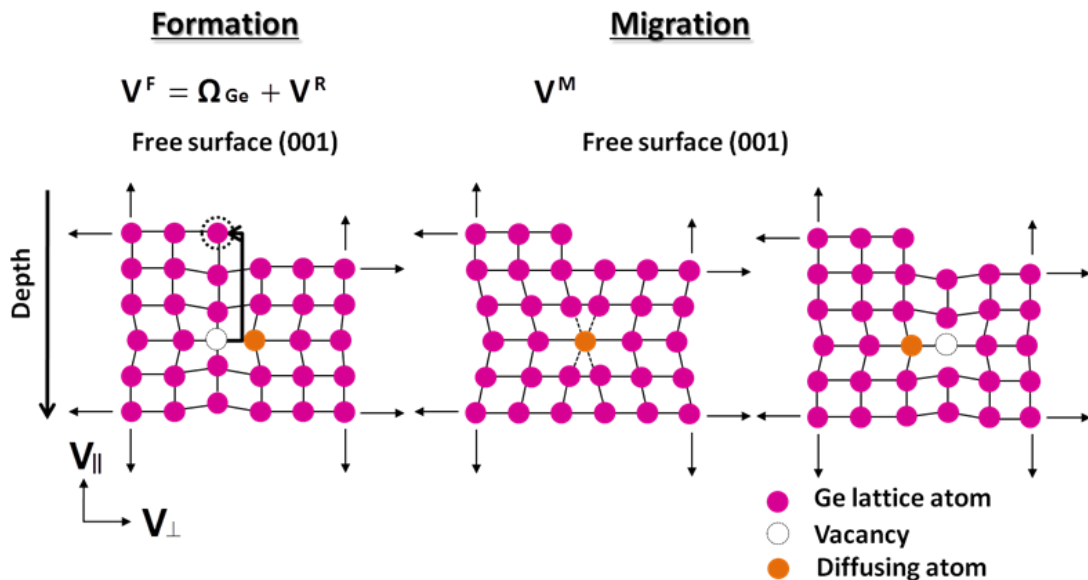
Figure 3.20 Schematic volume changes upon vacancy formation and migration for a simply vacancy mechanism. Work produced by interaction with applied stresses (thin arrows) affects self-diffusivity.

and is smaller than $+\Omega_{\mathrm{Ge}}$. Aziz *et al.* [10–12] further generalized the activation volume for a non-hydrostatic stress state by defining an activation strain tensor. The formation strain tensor ($\mathbf{V^F}$) is described as

$$\mathbf{V^F} = \Omega_{\mathrm{Ge}} \begin{bmatrix} 0 & & \\ & 0 & \\ & & 1 \end{bmatrix} + \frac{V^R}{3} \begin{bmatrix} 1 & & \\ & 1 & \\ & & 1 \end{bmatrix}. \tag{3.43}$$

The first term on the right-hand side of Eq. (3.43) shows the volume change corresponding to Ω_{Ge} at the free surface when a vacancy is created inside the crystal. The second term indicates that the relaxation volume propagates out elastically to surfaces and provides equal contributions in all directions [11]. In addition, the migration strain tensor ($\mathbf{V^M}$) is defined as

$$\mathbf{V^M} = \begin{bmatrix} V_\perp^M & & \\ & V_\perp^M & \\ & & V_\parallel^M \end{bmatrix}, \tag{3.44}$$

where $V_\perp^M$ and $V_\parallel^M$ are the volume changes perpendicular and parallel to the direction of the net transport at the saddle point in its migration path. Under hydrostatic stress, the activation volume is the scalar activation volume conventionally defined in Eq. (3.42), which is the sum of the trace of Eq. (3.43), $\Omega_{\mathrm{Ge}} + V^R$, and that of Eq. (3.44), V^M. In the presence of biaxial stress (σ_{biax}), the work needed to create a lattice site at the surface is zero because there is no normal force at the surface. Furthermore, the part of V^R that propagates on the free surface and interacts with the zero normal stress does not contribute to the work performed against the stress field. Therefore, the contribution of the activation volume to self-diffusion under biaxial stress via the vacancy mechanism, $V_{\mathrm{biax}}^{\mathrm{SD}}$, can be described as

$$V_{\mathrm{biax}}^{\mathrm{SD}} = \frac{2}{3} V^R + V^M - V_\parallel^M, \tag{3.45}$$

which is dominated by the relaxation and migration volume terms. Therefore, $V_{\mathrm{biax}}^{\mathrm{SD}}$ is negative. According to the strain tensor model and activation volume described in Eq. (3.40), the activation volume of self-diffusion under biaxial stress can be described as

$$V_{biax}^{SD} = -k_B T \left. \frac{\partial \ln D_{biax}^{SD}}{\partial \sigma_{biax}} \right|_T , \tag{3.46}$$

Based on Eq. (3.46) and the Ge self-diffusivities obtained experimentally (D_{biax}^{SD}) in this work, we find, $V_{biax}^{SD}=-(0.65\pm0.21)\Omega_{Ge}$. $V_{biax}^{SD} \approx -\Omega_{Ge}$ implies that upon the formation and migration of a vacancy, there exists a strong inward constriction of the lattice. The increase of Ge self-diffusivities in s-Ge results from the decrease of the activation enthalpy by the negative work performed against the stress field, $\sigma_{biax}V_{biax}^{SD}$. The compressive biaxial strain of 0.71% is expected to produce a small change of -0.9 ± 0.03 eV in the activation enthalpy. From the fittings by the Arrhenius expression, the difference between the activation enthalpy of self-diffusion in compressively strained Ge, 3.07 eV (this work), and in unstrained Ge, 3.13 eV (Ref. 15), can be found to be -0.06 eV ($=3.07-3.13$ eV). This value is within the accuracy of the value of -0.09 ± 0.03 eV deduced from the generalized activation volume model. Furthermore, from the comparison between the biaxial and hydrostatic stress states [Eqs. (3.42) and (3.45)], the following relationship can be given:

$$V^{SD} - \frac{3}{2}V_{biax}^{SD} = \Omega_{Ge} + \left(V_\parallel^M - V_\perp^M\right). \tag{3.47}$$

If the anisotropy in $\mathbf{V^M}$ is negligibly small, the right-hand side of Eq. (3.47) should become $+\Omega_{Ge}$. Aziz *et al.* [10−12] have described the contribution of the activation volume under biaxial stress, V_{biax}^{SD}, to the diffusion as $-\left(Q'/Y\right)$, where the biaxial modulus, Y, is the ratio of Young's modulus to one minus the Poisson ratio. For the Sb diffusion [11, 12], they have demonstrated the consistency of the predicted relationship by the values of Q' reported by Kringhøj *et al.* [26] and an activation volume V =+0.66 Ω determined for hydrostatically compressed Si in their work. The results are $V + (3/2)\left(Q'/Y\right) = (+1.20 \pm 0.33)\Omega$ for tensile Si and $V + (3/2)\left(Q'/Y\right) = (+0.93 \pm 0.20)\Omega$ for the compressively strained SiGe alloy, which agrees with the prediction of $+1\Omega$ (Y = 180.5 GPa for these cases). Werner *et al.* [24] reported positive values of the activation volume (V^{SD}) for Ge self-diffusion in Ge under hydrostatic pressure in the temperature range of 603 to 813 °C. Inserting the V_{biax}^{SD} deduced in this study and $V^{SD} = +0.24\Omega_{Ge}$ at 603

ᵒC reported in Ref. 20 into Eq. (3.47), we find $V^{SD} - (3/2)V^{SD}_{biax} = (+1.22 \pm 0.21)\Omega_{Ge}$, which is fully consistent with the $+1\Omega_{Ge}$ prediction. It is important to note that the analysis used here assumes that self-diffusion mediated by vacancies in the SLs reaches thermal equilibrium quickly during annealing, which is also consistent with our experimental results.

3.8 Conclusions

In conclusion, we have designed and conducted an experiment to reliably obtain the Ge self-diffusivity in biaxially compressed Ge. The compressive strain enhances Ge self-diffusion. The degree of the enhancement is described quantitatively by the theoretical prediction of a generalized activation volume model of a simple vacancy-mediated diffusion [10–12].

References

[1] K. Sawano, Y. Abe, H. Satoh, Y. Shiraki, and K. Nakagawa, Appl. Phys. Lett. **87**, 192102 (2005).

[2] B. Rössner, D. Chrastina, G. Isella, and H. von Känel, Appl. Phys. Lett. **84**, 3058 (2004).

[3] H. von Känel, M. Kummer, G. Isella, E. Müller, and T. Hackbarth, Appl. Phys. Lett. **80**, 2922 (2002).

[4] N. R. Zangenberg, J. Lundsgaard Hansen, J. Fage-Pedersen, and A. Nylandsted Larsen, Phys. Rev. Lett. **87** (2001) 125901.

[5] P. Laitinen, A. Strohm, J. Huikari, A. Nieminen, T. Voss, C. Grodon, I. Riihimäki, M. Kummer, J. Äystö, P. Dendooven, J. Räisänen, W. Frank, and the ISOLDE Collaboration, Phys. Rev. Lett. **89** 085902 (2002).

[6] A. Strohm, T. Voss, W. Frank, J. Räisänen, and M. Dietrich, Physica B **308-310**, 542 (2001).

[7] R. Kube, H. Bracht, J. Lundsgaard Hansen, A. Nylandsted Larsen, E. E. Haller, S. Paul, and W. Lerch, J. Appl. Phys. **107**, 073520 (2010).

[8] R. Kube, H. Bracht, J. Lundsgaard Hansen, A. Nylandsted Larsen, E. E.

Haller, S. Paul, and W. Lerch, Mater. Sci. Semicond. Process. **11**, 378 (2008).

[9] N. E. B. Cowern, P. C. Zalm, P. van der Sluis, D. J. Gravesteijn, and W. B. de Boer, Phys. Rev. Lett. **72**, 2585 (1994).

[10] M. J. Aziz, Appl. Phys. Lett. **70**, 2810 (1997).

[11] M. J. Aziz, Mater. Sci. Semicond. Process. **4**, 397 (2001).

[12] M. J. Aziz, Y. Zhao, H. J. Gossmann, S. Mitha, S. P. Smith, and D. Schiferl, Phys. Rev. B **73**, 054101 (2006).

[13] A. Fick, Phil. Mag. **10**, 30 (1855).

[14] Y. Shimizu, M. Uematsu, and K. M. Itoh, Phys. Rev. Lett. **98**, 095901 (2007).

[15] E. Hüger, U. Tietze, D. Lott, H. Bracht, D. Bougeard, E. E. Haller, and H. Schmidt, Appl. Phys. Lett. **93**, 162104 (2008).

[16] E. Kasper, A. Schuh, G. Bauer, B. Holländer, and H.Kibbel, J. Cryst. Growth **157**, 68 (1995).

[17] V. A. Shah, A. Dobbie, M. Myronov, D. J. F. Fulgoni, L. J. Nash, and D. R. Leadley, Appl. Phys. Lett. **93**, 192103 (2008).

[18] K. Morita, K. M. Itoh, M. Nakajima, H. Harima, K. Mizoguchi, Y. Shiraki, and E. E. Haller, Physica B **316-317**, 561 (2002).

[19] Y. Kawamura, Y. Shimizu, H. Oshikawa, M. Uematsu, E. E. Haller, and K. M. Itoh, Appl. Phys. Express **3**, 071303 (2010).

[20] Y. Kawamura, Y. Shimizu, H. Oshikawa, M. Uematsu, E. E. Haller, and K. M. Itoh, Physica B **404**, 4546 (2009).

[21] M. Naganawa, Y. Shimizu, M. Uematsu, K. M. Itoh, K. Sawano, Y. Shiraki, and E. E. Haller, Appl. Phys. Lett. **93**, 191905 (2008).

[22] A. L. Patterson, Phys. Rev. **56**, 978 (1939).

[23] W. Jüngling, P. Pichler, S. Selberherr, E. Guerrero, and H. W. Pötzl, IEEE Trans. Electron Devices **ED-32**, 156 (1985).

[24] M. Werner, H. Mehrer, and H. D. Hochheimer, Phys. Rev. B **32**, 3930 (1985).

[25] D. R. Campbell, Phys. Rev. B **12**, 2318 (1975).

[26] P. Kringhoj, A. Nylandsted Larsen, and S. Yu. Shirayev, Phys. Rev. Lett. **76**, 3372 (1996).

[27] N. R. Zangenberg, J. F. Pedersen, J. Lundsgaard Hansen and A. Nylandsted Larsen, J. Appl. Phys. **94**, 3883 (2003).

[28] E. Nygren, M. J. Aziz, D. Turnbull, J. M. Poate, D. C. Jacobson, and R. Hull,

Appl. Phys. Lett. **47**, 105 (1985).

[29] R. N. Jeffery and D. Lazarus, J. Appl. Phys. **41**, 3186 (1970).

[30] C. F. Smithells, Metals Reference Book, 5th ed. 132 (1976).

Chapter 4

Near-Infrared Photoluminescence from Germanium Nanowires

This chapter reports observation of near-infrared photoluminescence from free-standing, vertically aligned germanium nanowires grown on a (111)-oriented silicon substrate. The energy of the photoluminescence peak is very close to that of the bulk crystalline germanium direct band gap. The intensity shows an approximately quadratic dependence on excitation laser power and decreases with decreasing temperature. The peak position exhibits a red-shift with increasing laser power due to laser-induced heating of the germanium nanowires. These observations indicate that the photoluminescence originates from the direct-band-gap recombination in the germanium nanowires.

This work was carried out in collaborations with Kevin Huang, Shruti Thombare, Marika Gunji, Shu Hu, and Professor Mark Brongersma of Stanford University, and Toyofumi Ishikawa of Keio University.

4.1   Introduction

Over the last decade, nanoscale semiconductor structures with low dimensionality (D) such as quantum wells (2-D), nanowires (1-D), and nanocrystals (0-D) have attracted much attention due to their remarkable physical properties and possible applications in nanoscale electronic and optoelectronic devices [1, 2]. In particular, an application of Ge nanowires (NWs) for MOS FETs has been of great interest, primarily because of the small band gap of Ge, its high carrier mobilities and its compatibility with silicon integrated circuits. [3]. One-dimensional structures suppress carrier scattering and enable fabrication of so-called surrounding gate transistors (SGTs) [4], in which the level of leakage current can be decreases significantly. However, with increasing the surface-to-volume ratio, the effect of surface states and/or surface defects becomes larger in such nanowire devices.   Photoluminescence (PL) is a powerful tool for assessing the structural quality of materials because detection of band-edge PL generally requires a low density of surface state and/or surface defects. Therefore, the PL properties of Ge NWs are of great interest.

There have been several reports on the observation of near-infrared (NIR) PL, near the crystalline Ge band gaps, from Ge quantum wells in various structures [3−7]. For lower-dimension structures, visible PL from Ge nanocrystals embedded in several different oxide matrices [8−13] have been investigated. The origin of the observed blue PL has been discussed extensively and is attributed to defects at the nanocrystal/matrix interface or in the matrix itself. In addition, NIR PL due to radiative recombination of quantum-confined carriers in Ge nanocrystals embedded in silicon dioxide matrices [14], wire-shaped Ge islands grown on Si substrates [15], and Ge quantum wires self-aligned at step edges on Si [16] have been investigated. For Ge nanowires (NWs), Audoit *et. al.* [1] have measured ultraviolet (UV) PL from Ge NWs encased within mesoporous silica hosts. In this case the strain imposed on the wires by the matrix may have induced the UV PL in the NWs. On the other hand, despite the great number of reports on light-emitting indirect gap Si nanowires as well as the synthesis of high quality free-standing Ge NWs and their structural [17−19] and electrical [20, 21] characterization, surprisingly little

attention has been given to PL properties of the free-standing Ge NWs. Kamenev *et al.* [22] have investigated PL from free-standing Ge NWs grown on Si substrates in the NIR wavelength region. The Ge NWs, however, did not show a PL signal near the crystalline Ge band gap, most likely due to the presence of a high density of non-radiative recombination centers at the interface between Ge and the native oxide layer combined with the high surface-to-volume ratio of nanowires.

In this chapter, we report what are, to our knowledge, the first NIR PL observations from free-standing, vertically aligned Ge NWs and discuss the origin of the observed NIR PL.

4.2   Germanium Nanowire Growth

4.2.1   Vapor-Liquid-Solid (VLS) Mechanism

There exist several bottom-up techniques to synthesize semiconductor nanowires, the most commonly studied of which is vapor-liquid-solid (VLS) growth mechanism. Some of the techniques which have been used to synthesize nanowires by the VLS mechanism are chemical vapor deposition (CVD), molecular beam epitaxy (MBE), pulsed laser ablation, and thermal evaporation. The VLS mechanism was proposed in 1964 as an explanation for Si whisker growth from the gas phase in the presence of a liquid gold (Au) droplet placed upon a Si substrate [23]. The growth of a crystal through direct adsorption of a gas phase on to a solid surface is generally very slow due to its high reaction energy. The VLS mechanism overcomes this by introducing a catalytic liquid alloy phase, which is capable of forming a eutectic mixture with the nanowire material. The metal catalyst is heated above the eutectic temperature in the presence of a vapor containing the nanowire material and then can rapidly adsorb the vapor to supersaturation levels, and from which crystal growth can subsequently occur from nucleated seeds at the liquid–solid interface. With continual feeding of the vapor reactive species into the liquid alloy, this solid grows in length as a pillar (nanowire) while the liquid droplet alloy remains at the tip of the pillar. The size and position of the wires are determined by that of

the metal catalysts. The physical characteristics of nanowires grown in this manner depend, in a controllable way, upon the size and physical properties of the liquid alloy. Lithography techniques can also be used to controllably manipulate the diameter and position of the metal catalysts.

Ge NWs used in this study were grown on a (111)-oriented Si substrate using colloidal Au nanoparticles as the catalysts by using CVD. Figure 4.1 shows a schematic illustration of the VLS growth mechanism for the case of Au-nanoparticle-catalyzed Ge NW growth on a Si(111) substrate using germane (GeH_4) as the precursor. According to the Au-Ge binary phase diagram shown in Fig. 4.1(a), mixing Au with Ge greatly reduces the melting temperature of the liquid alloy as compared to the alloy constituents. The melting temperature of the Au:Ge alloy reaches a minimum temperature of 361 °C, i.e., eutectic temperature ($T_{eutectic}$), when the ratio of its constituents is 72:28 Au:Ge. This point in a phase diagram is known as a eutectic point. As shown in Fig. 4.1(b), (1) a Si(111) substrate on the surface of which solid Au nanoparticles with a specific diameter exist is prepared by using colloidal solution with Au nanoperticles. The Au nanoparticles are solid at a temperature just above the Au-Ge eutectic temperature. (2) The substrate is annealed at temperatures higher than the eutectic temperature and vapor Ge is deposited by means of GeH_4 gaseous mixture reaction described by

$$GeH_4(g) \rightarrow GeH_2(g) + H_2(g) \qquad (5.1a)$$

$$GeH_2(g) \rightarrow Ge(g) + H_2(g) \qquad (5.1b)$$
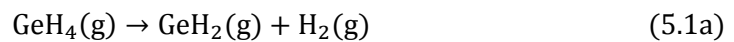
and then Au-Ge alloy droplets are created on the substrate surface. (3) Since Ge has a much higher melting point (~938 °C) than that of the eutectic alloy, Ge atoms precipitate out of the supersaturated liquid-alloy droplets underneath the droplets, which is nucleation of a single-crystalline Ge NW. Then the pillars (NWs) with a diameter that equals to that of the droplets grow and the droplets rise from the surface.

(a)

(b)
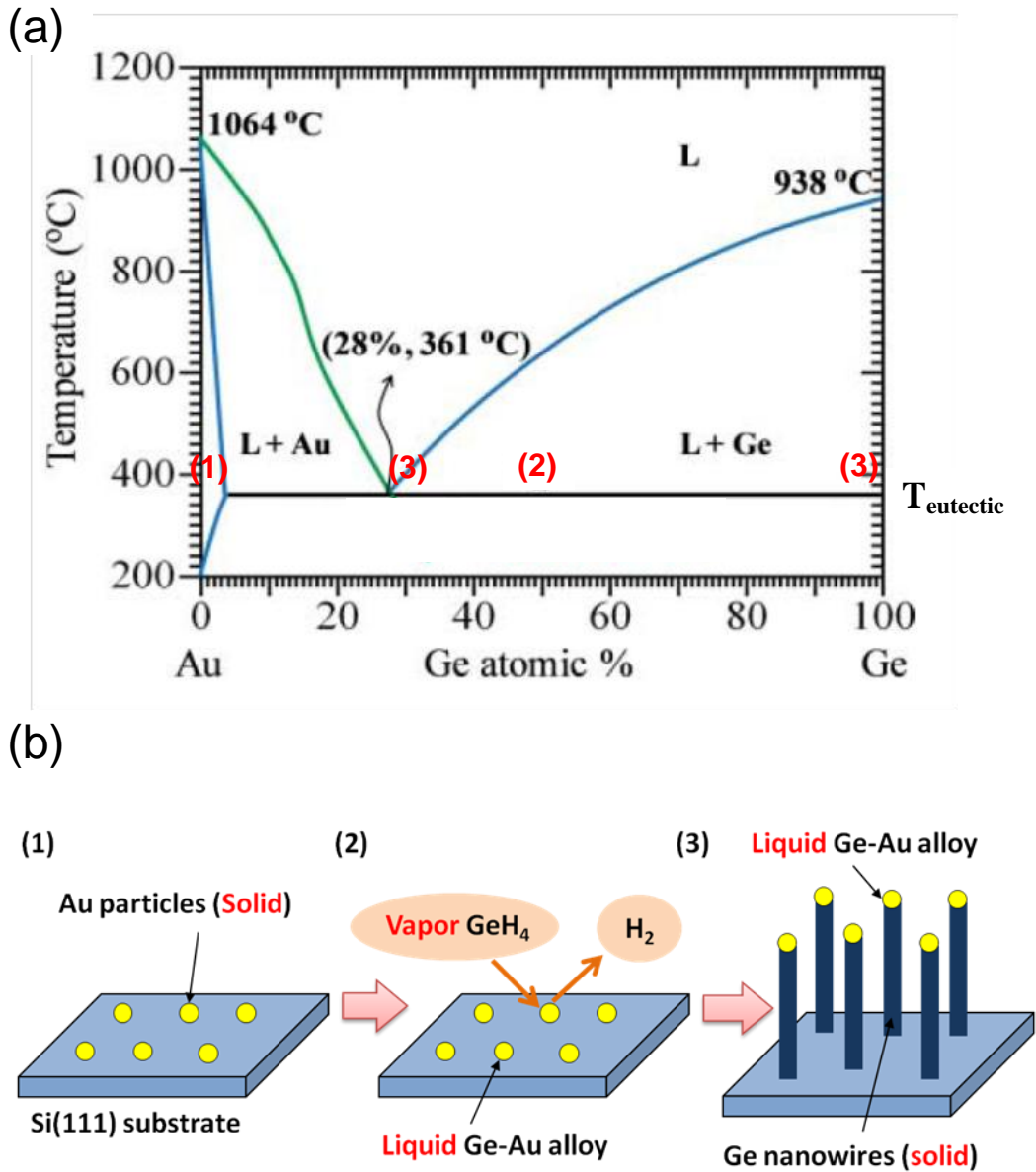
Figure 4.1 (a) Au-Ge alloy phase diagram. (b) Schematic illustration of the VLS growth mechanism for the case of Au-nanoparticle-catalyzed Ge NW growth on a Si(111) substrate using germane (GeH₄) as the precursor. The numbers in the diagram (Fig. (a)), (1)−(3), correspond to the stages (1)−(3) of the VLS growth shown in Fig. (b).

4.2.2　Two-Temperature Growth Method

As mentioned above, temperatures above the Au-Ge eutectic temperature (~361 °C) are ideally required to obtain epitaxial growth of Ge NWs from Au colloids on Si substrates. However, at these high temperatures of growth, there is deposition of Ge on the sidewalls of the growing Ge NW, which competes with the catalyzed deposition at the tip and causes tapering of the nanowires. A tapered Ge NW is illustrated in Fig. 4.2(a). The nanowire base is formed first and presents for more time during reactive gas flow, resulting in the base being wider than the tip. The tapered nanowire significantly affects the device characteristics because the electronic structure of nanowires depends on nanowire diameter.

Recently, it has been revealed that Ge NW growth from Au catalyst at lower temperatures such as 280 °C can be performed without tapering but the epitaxial relation with the substrate is not presented [19]. It has been also known that the initial nucleation step can be performed at temperatures as low as 350 °C. These phenomena may be closely related to the change of the Gibbs-Thomson pressure in nanostructures [19]. In order to obtain epitaxially oriented untapered nanowires, a two-step temperature profile has been proposed:
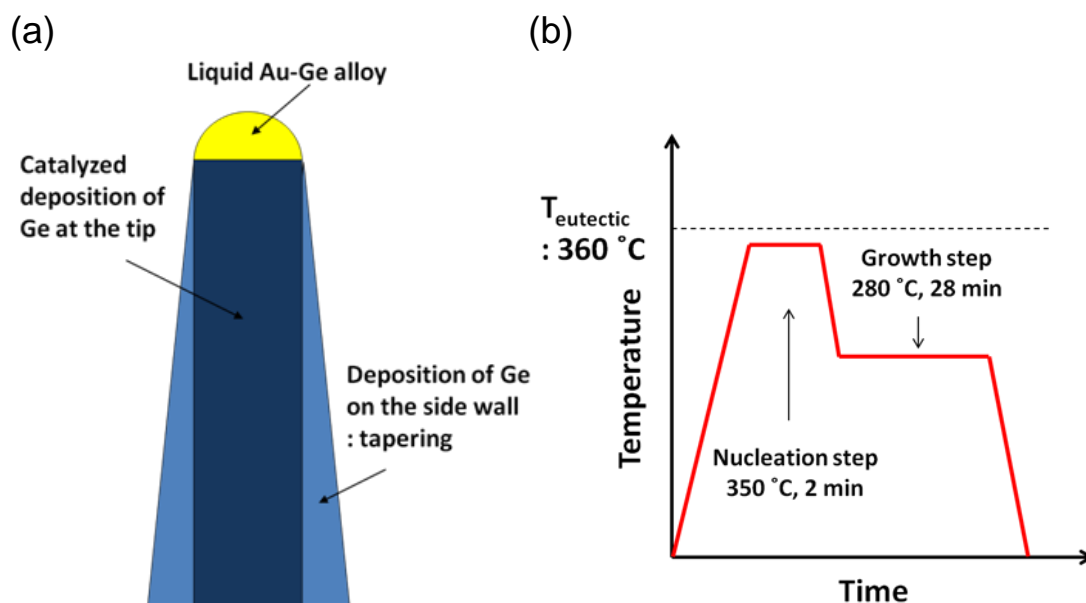
Figure 4.2 (a) Schematic image of a taped Ge NW. (b) Proposed two-step temperature profile for Au-nanoparticle-catalyzed Ge NW growth.

a temperature above 350 °C is used to nucleate the nanowires, and then the temperature is lowered below 280 °C for wire growth, as shown in Fig. 4.2(b). The two temperature procedure leads to the growth of Ge NWs that have uniform diameter and are epitaxially aligned to the <111> direction of the substrate with a strong preference for vertical growth.

4.2.3   Germanium Nanowire Growth System

All growth experiments were performed in a lamp-heated, cold-wall quartz tube reactor (Figure 4.3) [24]. Lamping heating permits fast heating and cooling rates. The tube is cooled using both water and air, which serves to minimize deposition on the reactor walls and allow for faster cooling times after NW growth. The samples are placed on a dummy Si wafer, which rests on a Si carbide susceptor, which in turn rests on another Si wafer with an attached thermocouple. Power to the lamps is controlled through a feedback loop using a proportional-integral-differential controller. The samples are loaded into the reactor through a load lock, which has a base pressure of ~10^{-6} Torr. There are eleven gas lines, the flow rate of each being controlled by a separate mass flow controller. The total pressure in the reactor is controlled by a butterfly valve adjusted by a pressure controller.
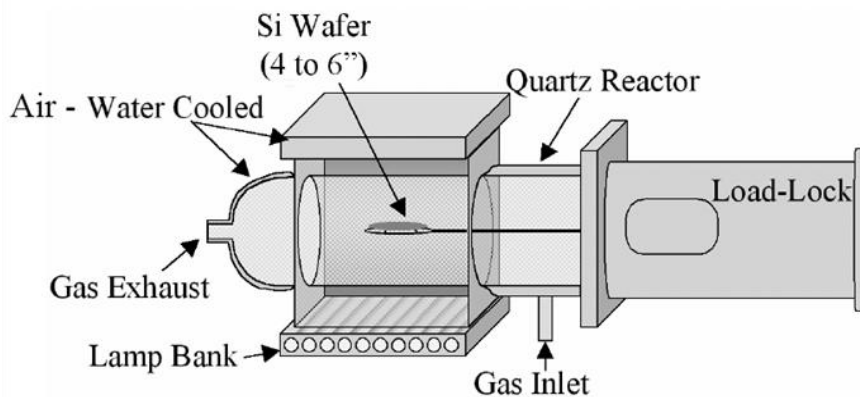
Figure 4.3 Schematic of a lamp-heated, cold-wall quartz tube reactor which was used in this experiment [24].

4.2.4 Growth Procedure and Condition

The Ge NWs used in this study were grown using colloidal gold catalyst particles of 40 nm diameter via the vapor-liquid-solid mechanism, as described in 4.2.1. Substrates were Si (111) (n-type dopant P, resistivity ranging from 1500 to 2500 $\Omega \cdot$cm). All of the substrates were cleaned in freshly made Piranha (4 volumes of H_2SO_4/1 volume of 30% by mass aqueous H_2O_2) followed by a thorough rinse with deionized water. Then the Au colloids were spin coated on the substrate at 3000 rpm. Nanowire growth was carried out in the cold-walled, lamp-heated, CVD chamber (see 4.2.3). In order to grow denser nanowires for PL measurements, we used the two-temperature growth method at higher temperatures than usual (than proposed one in Fig. 4.2.(b)) but for shorter growth time: nucleation step at 375 °C for 2 min and growth step at 360 °C for 20 min, with a GeH_4 precursor diluted with H_2. The GeH_4 partial pressure was maintained at 1 Torr in a total chamber pressure of 30 Torr. These Ge NWs were not intentionally doped.
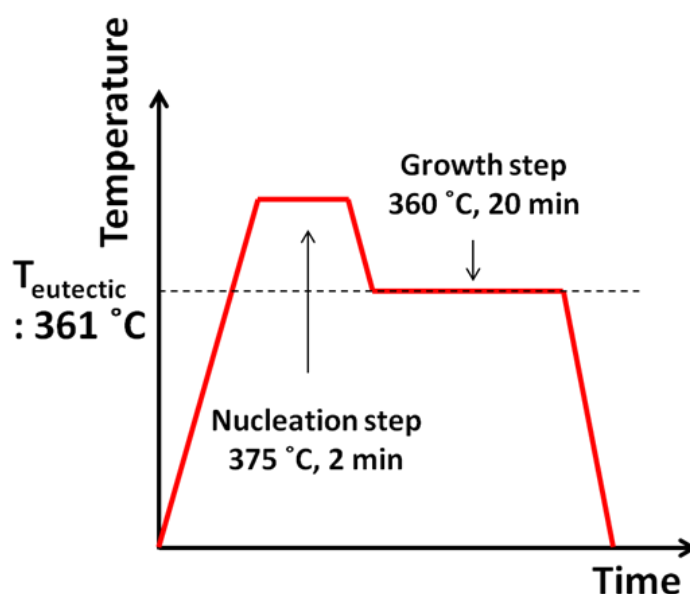
Figure 4.4 Two-step temperature profile that was used in this work to grow denser Ge NWs for PL measurements.

4.2.5   Characterization: SEM, TEM

Transmission electron microscopy (TEM) and scanning electron microscopy (SEM) were used to characterize the crystal structure, growth direction, diameter, and length of the Ge NWs which were grown in this experiment. The TEM observations confirmed that the Ge NWs were found to be epitaxial with a <111> growth orientation and single crystalline in nature. No dislocations were detected in the Ge NWs during the TEM observations. Figure 4.5 shows an SEM image of the Ge NWs. The SEM image reveals that these Ge NWs were vertically aligned on the Si (111) substrate with an average diameter of 40 nm and an average length of 5 µm.
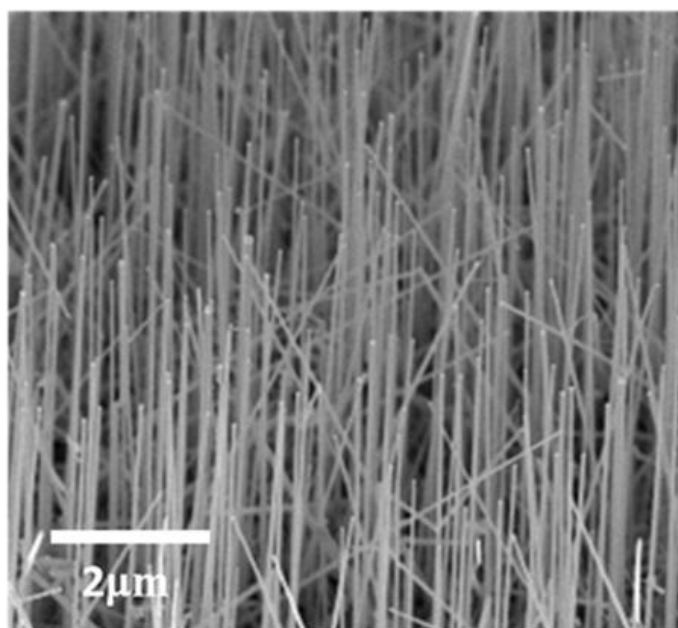
Figure 4.5 SEM image, taken at a 45 tilt angle, of Au-catalyzed Ge NWs grown on a Si(111) substrate. This image shows the average diameter and length of the Ge NWs of 40 nm and 5 µm, respectively.

4.3   Basics of Photoluminescence from Germanium

4.3.1   Photoluminescence (PL)

Photoluminescence (PL) is the spontaneous emission of light from a material under optical excitation. PL investigations can be used to characterize a variety of material parameters. PL in a simple energy band diagram of semiconductors is illustrated in Fig. 4.6. When light of sufficient energy is incident on a semiconductor material, photons are absorbed and electrons at the valence band are excited to the conduction band. Eventually, these excitations relax with time, and the excited electrons return to the valence band and recombine with holes in the valence band. If radiative relaxation (recombination) with emission of photons occurs, the emitted light is called PL, which can be experimentally collected and analyzed. In particular, when electrons in the conduction band recombine with holes in the valence band without involving defects, or intermediate states in the band gap, this recombination process is called band-to-band recombination (Figure 4.6), which radiatively occurs. Typically, band-to-band radiative recombination occurs from the edge of conduction band to the edge of valence band and emits light at an energy which nearly equals to the energy of the band gap. Therefore, the emitted light is called band-edge PL. Thus, PL spectra obtained from PL measurements provide the transition energies, which can be used to determine electronic energy levels in semiconductor material. The intensity of the PL signal provides information on the quality of surfaces and interfaces, because detection of band-edge PL generally requires a low density of surface and interface recombination centers. Surfaces and interfaces usually contain a high concentration of impurity and defect states, which affects band-to-band radiative recombination. Dangling bonds often provide numerous midgap states that facilitate rapid non-radiative recombination. PL analysis is non-destructive and requires very little sample manipulation or environmental control. However, the fundamental limitation of PL analysis is its reliance on radiative events, as remarked above. Materials with poor radiative efficiency, such as low-quality indirect-band-gap semiconductors, are difficult to study via PL.
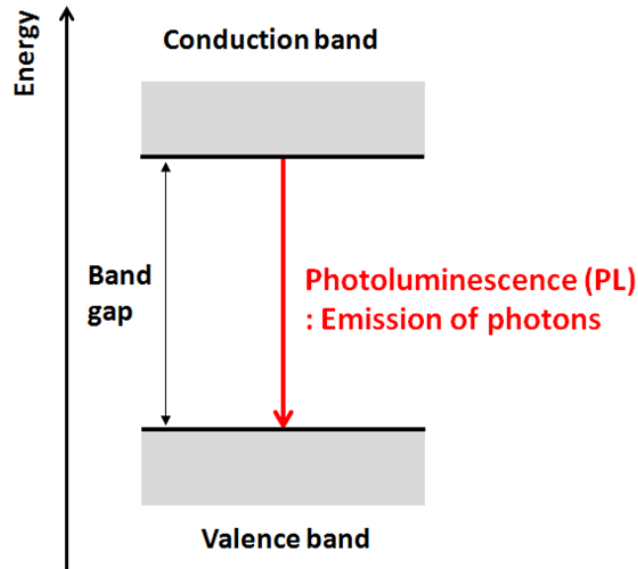
Figure 4.6 Schematic illustration of PL in a simple energy band diagram of semiconductors. This radiative recombination path displayed in the diagram shows band-to-band recombination.

4.3.2   Band Structure of Bulk Germanium

Figure 4.7 shows a schematic energy band diagram of bulk Ge. The energy is plotted as a function of the wavevector, $\mathbf{k}$, along the main crystallographic directions in the crystal, since the band diagram depends on the direction in the crystal. Table 4.1 summarizes the basic energy separations in the Ge band diagram at 300 K. Band-gap energies generally change with temperature due to electron-phonon interactions on the corresponding electronic state. This is called band-gap renormalization. Ge is an indirect band gap semiconductor as well as Si. The conduction band minimum and the valence band maximum do not occur at the same value for the wavenumber. The valence band edge (maximum) is located at the center of the Brillion zone, i.e., the Γ valley ($\mathbf{k} =< 000 >$). The conduction band minimum is located at the L valley

($\mathbf{k}$ =< 111 >) with a relative energy of 0.66 eV at 300 K. This energy separation is so-called indirect band gap (E_g) in Ge. The energy separation between the valence band maximum and a conduction band minimum at the Γ valley ($E_{\Gamma 1}$) is 0.8 eV at 300 K. This is so-called direct band gap in Ge. An important feature of Ge band structure is that the conduction band minimum at the Γ valley with the relative energy of 0.80 eV is only 0.14 eV higher in energy than the L valley minimum with the relative energy of 0.66 eV (at 300 K). Therefore, there has been considerable interest in radiative recombination processes in Ge because of the possibility of achieving direct-band-gap semiconductor action in this indirect-band-gap semiconductor.
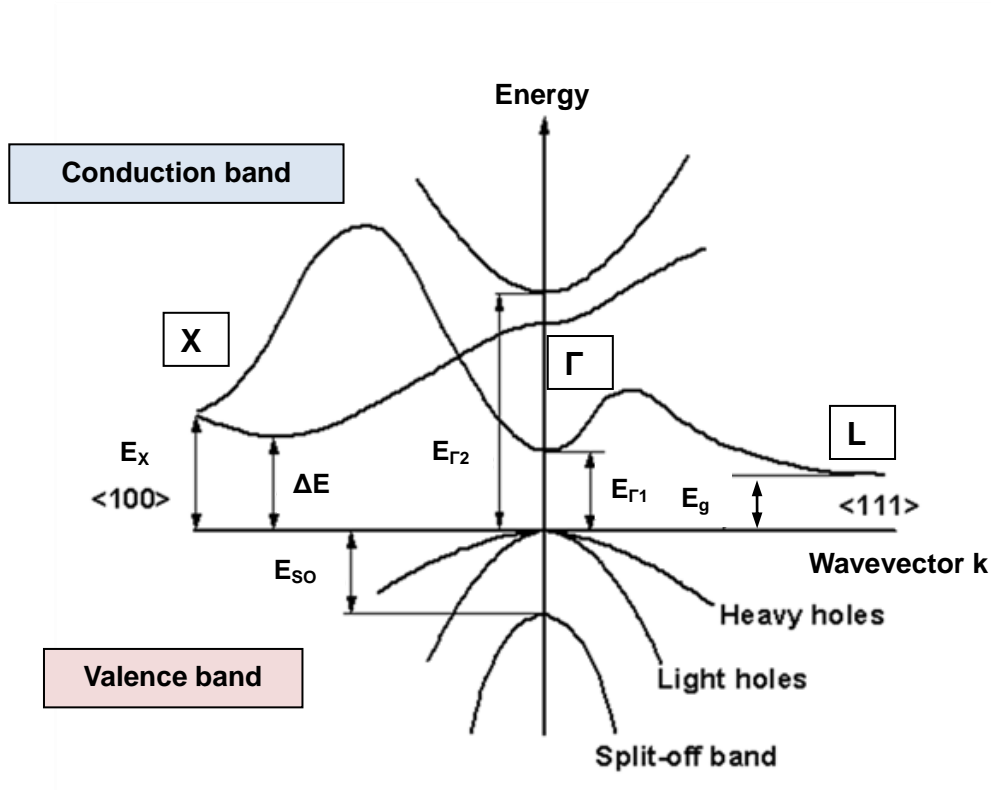
Figure 4.7 Schematic energy band diagram of bulk Ge. The energy is plotted as a function of the wavevector, $\mathbf{k}$, along the main crystallographic directions in the crystal. The basic energy separations, E_x (x=g, Γ1, Γ2, X, SO) and ΔE, in the Ge band diagram are shown in Table 4.1.

Table 4.1 Energy separations in the band diagram of bulk Ge (Figure 4.7) at 300 K.

	Energy (eV)
Indirect band gap (L) E_g	0.66
Direct band gap (Γ1) $E_{\Gamma 1}$	0.80
Energy separation (Γ2) $E_{\Gamma 2}$	3.22
Energy separation (X) E_X	1.2
Energy separation ΔE	0.85
Energy spin-orbital splitting (Γ) E_{SO}	0.29

4.3.3   Band-Edge Photoluminescence in Bulk Germanium

In bulk Ge, mainly two types of band-edge PL can be observed, corresponding to direct band-to-band radiative recombination and indirect band-to-band radiative recombination involving phonon emission and absorption processes [25–33]. The two band-edge PL processes are illustrated in Fig. 4.8. Electrons pumped from the valence band to the conduction band near the Γ valley relax to the conduction band edge at the Γ valley and then majority of the electrons rapidly scatter to the X valley and subsequently to the conduction band minimum, i.e., the L valley, within a time scale of picoseconds [34]. Therefore, majority of the electrons excited to the conduction band eventually recombine with holes in the valence band via the conduction band edge at the L valley (Figure 4.8(b)). This indirect band-to-band recombination is a radiative recombination process, which emits infrared light, so-called indirect-band-gap PL. However, the recombination process also requires participation (absorption and emission) of phonons to conserve momentum, which is a non-radiative process. Therefore, the emitted photon's energy, hν, becomes $h\nu = E_g - \hbar\omega$, where h is Plank's constant, ν is the photon's frequency, and $\hbar\omega$ represents the energy of the phonon involved in the recombination process. On the other hand, electrons remaining at the edge of the Γ valley directly recombine with holes in

the valence band without involving phonons (Figure 4.8(a)). The phonon momentum is negligible compared to the electron momentum so that in the recombination process the electron's k vector does not change. This direct band-to-band recombination emits infrared light at an energy which nearly equals to the direct band gap (hv = $E_{\Gamma 1}$), so-called direct-band-gap PL. Although the number of electrons in the central Γ valley is much less than the number in the L valley, the recombination rate across the direct band gap far exceeds that across the indirect band gap because phonons are required for indirect-band-gap recombination [25, 28].
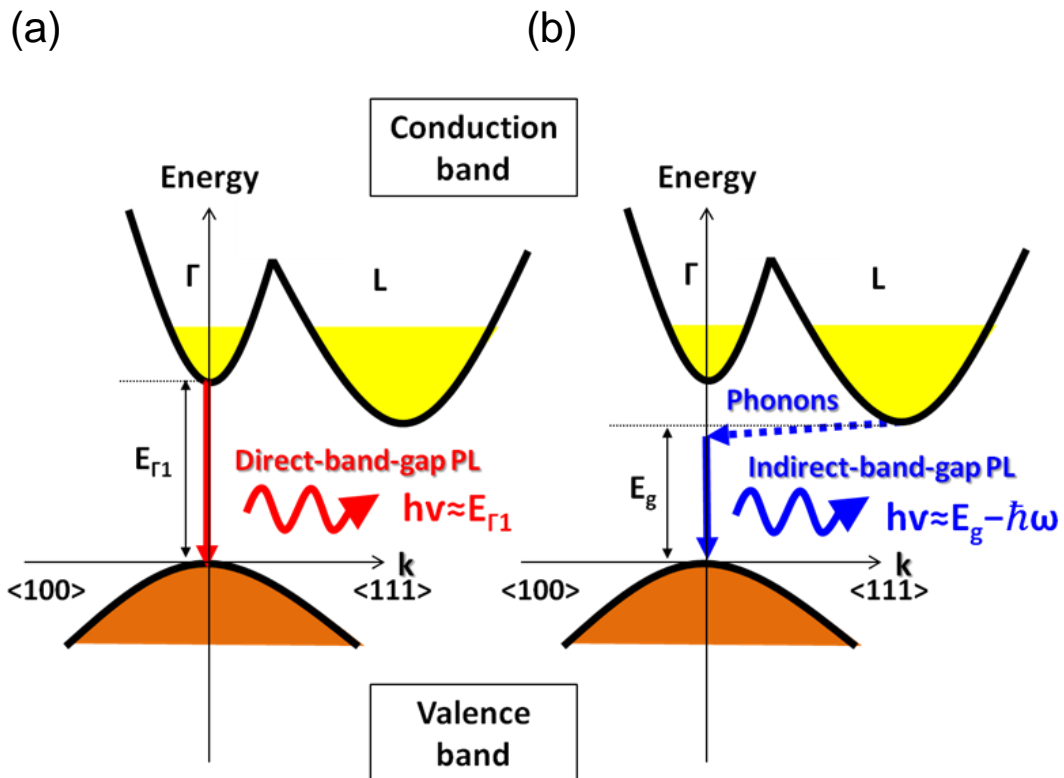
Figure 4.8 Schematic of band-edge PL in bulk Ge: (a) direct-band-gap PL, and (b) indirect-band-gap PL involving phonons. For direct-band-gap PL, electrons in the conduction band directly recombine holes in the valence band and the emitted photon's energy is described by hv = $E_{\Gamma 1}$. For indirect-band-gap PL, electrons in the conduction band recombine with holes in the valence band involving phonons and the emitted photon energy becomes hv = $E_g - \hbar\omega$, where $\hbar\omega$ represents the phonon's energy.

4.4   Photoluminescence Measurement Conditions

A picture of the NIR set-up which was utilized in this work, at Brongersma group of Stanford University, is shown in Fig. 4.9. The samples were excited by means of a frequency doubled Nd:YAG diode-pumped solid-state laser, emitting continuous-wave at a wavelength of 532 nm (Spectra Physics Millennia Pro Laser). The emitted light was dispersed in a Spectra Pro 2750 spectrometer in the wavelength range from 1100 to 2200 nm and collected by a liquid nitrogen-cooled strained-InGaAs detector. The laser beam was focused onto the sample surfaces through a 10× microscope objective having a 0.26 numerical aperture. The incident laser power on the samples surfaces was varied between 10 and 40 mW. The laser power density at 40 mW excitation is estimated to be approximately 10~20 mW/cm^2. All measurements were performed under atmospheric pressure. Quantum confinement effects should be negligible in our NWs because the diameter (~40 nm) of the NWs is larger than the exciton Bohr radius (~24 nm) of Ge [9].
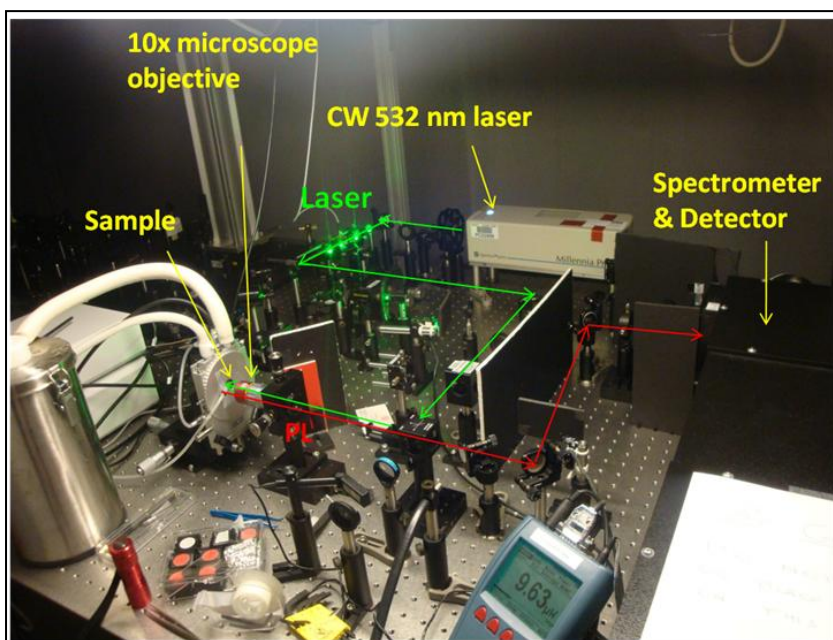
Figure 4.9 Picture of the NIR PL set-up, at Brongersma group of Stanford University, utilized in the measurements

4.5   Near-Infrared Photoluminescence from Germanium Nanowires

4.5.1   Room-Temperature Measurements

Figure 4.10(a) displays the NIR room-temperature PL spectra of the Ge NWs measured with different excitation laser powers between 10 and 40 mW. One broad peak emerges and exhibits a monotonic shift toward longer wavelength of up to ~130 nm (~60 meV) with increasing excitation laser power. To confirm that the Si (111) substrate did not play any part in the observed PL from the Ge NWs, we performed the same experiments on a Si (111) bare substrate identical to the ones used in NW growth, with the same measurement conditions. The spectrum of the Si (111) substrate shows only one peak near the crystalline Si indirect band gap ~1.11 µm (~1.12 eV) and no other peaks are detected in the longer wavelength region. Therefore, the observed NIR PL originates from the Ge NWs.   For further comparison, PL from bulk Ge (Ge (111) substrates: p-type dopant Ga, resistivity ranging from 1.8 to 2.3 Ω·cm) has been measured under the same conditions. As shown in the inset to Fig. 4.10(a), we have observed two PL peaks, corresponding to band-edge recombination through the crystalline Ge direct band gap at 1.55 µm (0.80 eV) and indirect band gap at 1.77 µm (0.70 eV) in increasing order of wavelength. Both the direct- and indirect-band-gap PL peak positions of the bulk Ge are insensitive to excitation laser power, in contrast to the PL peak behavior of the Ge NWs. In addition, the peaks in the inset to Fig. 4.10(a) are consistent with previous reports on PL from Ge [25–33]. Figure 4.10(b) summarizes the PL peak positions as a function of excitation laser power for both samples. The PL peak position of the Ge NWs with 10 mW laser excitation agrees with the direct-band-gap PL peak position of the bulk Ge.   This agreement suggests that the observed PL from the Ge NWs originates from direct-band-gap radiative recombination.
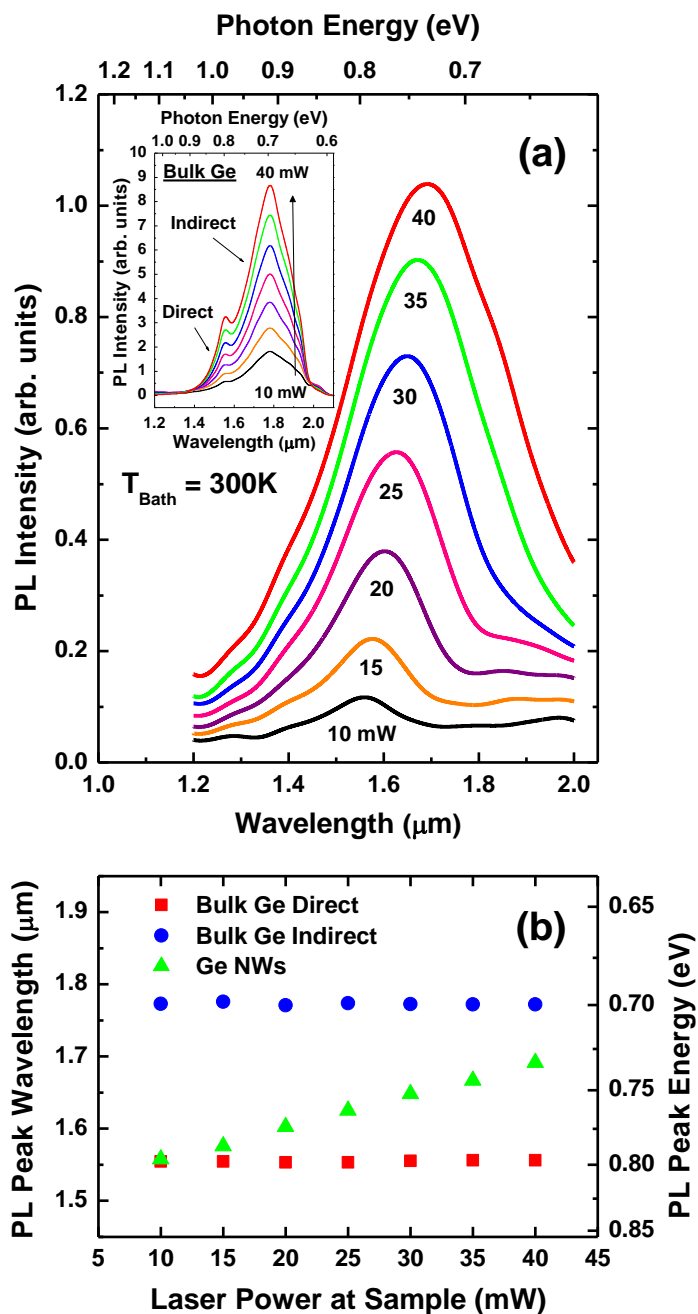
Figure 4.10 (a) NIR room-temperature PL spectra of Ge NWs, measured at different excitation laser powers between 10 and 40 mW. The numbers below the spectra indicate the excitation laser powers impinging on the samples surfaces. The inset shows NIR room-temperature PL spectra of bulk Ge, measured under the same optical conditions as the Ge NWs. (b) PL peak wavelengths (left) and energies (right) of the bulk Ge and the Ge NWs as a function of excitation laser power at the samples surfaces.
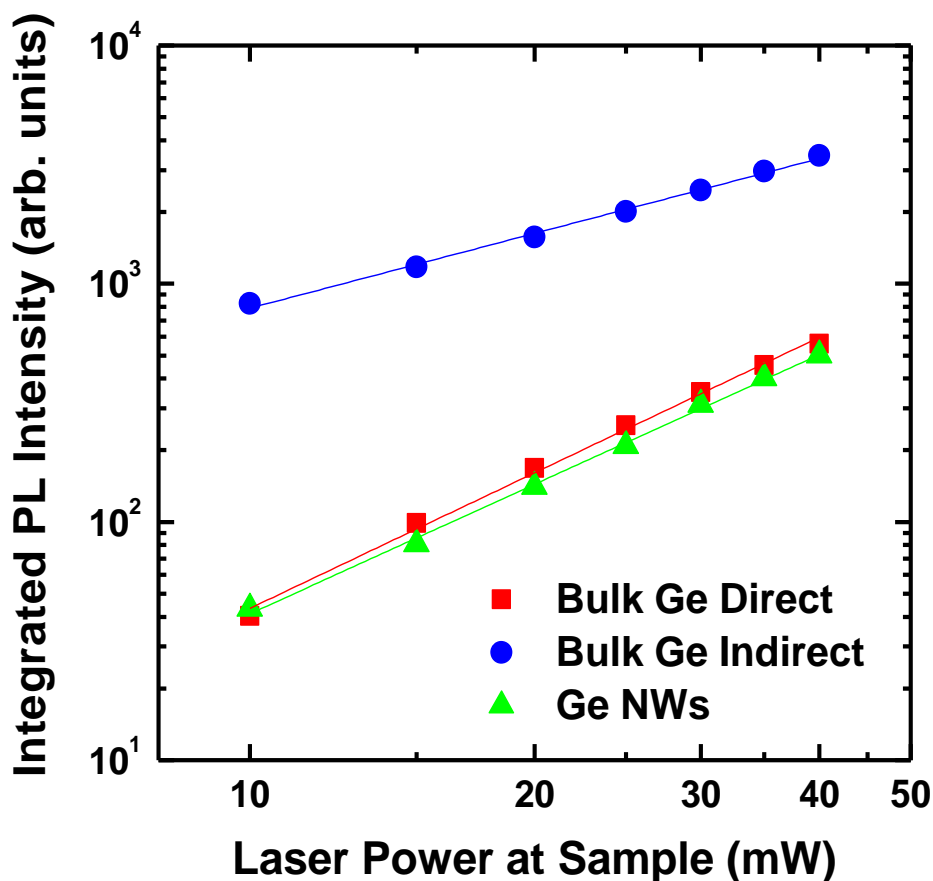
Figure 4.11 Integrated PL peak intensities of bulk Ge and the Ge NWs as a function of excitation laser power, measured at bath temperature of 300 K (room temperature). The scale is logarithmic along both axes.

Figure 4.11 displays integrated PL peak intensities as a function of excitation laser power for both samples. Note that the scale is logarithmic along both axes. For bulk Ge, the exponent is nearly equal to 1 for indirect-band-gap PL and ~1.9 for direct-band-gap PL. It is known that the intensity of PL is proportional to the square of the injected carrier concentration provided that the material is undoped since each emitted photon is generated from a recombination

involving an excess electron-hole pair [27]. The recombination rate is then proportional to the product of the concentrations of electrons and holes and each of those is proportional to the excitation laser power [27]. The nearly quadratic dependence observed for the direct-band-gap PL from the bulk Ge matches well with the expected one. Because the concentration of the electrons in the L valley of the Ge conduction band is significantly higher than that in the Γ valley, the probability of a three-carrier-mediated Auger process with energy transferred to a second electron should also be relatively high [27, 29]. Auger recombination, a process that competes with non-radiative recombination, leads to a linear dependence for the case of indirect-band-gap PL in the bulk Ge [27, 29]. The integrated PL peak intensity of the Ge NWs is very close to that of the direct-band-gap PL in the bulk Ge under the same measurement conditions and shows a nearly quadratic dependence on excitation laser power with an exponent of ~1.8. These results strongly suggest that direct-band-gap recombination is responsible for the PL detected from the Ge NWs.

4.5.2 Low-Temperature Measurements

In order to verify our interpretation, we also performed low-temperature PL measurements on both of these samples, placing them in a thermal stage (Linkam THMS600) cooled down to liquid-nitrogen temperature (77 K) at lowest. Figure 4.12 shows the low-temperature PL spectra of (a) the bulk Ge and (b) the Ge NWs. As shown in Fig. 4.12(a), with decreasing bath temperature, the indirect-band-gap PL peak of the bulk Ge sharpens and its intensity drastically increases. For the direct-band-gap transitions in bulk Ge (see inset to Fig. 4.12(a)), with decreasing bath temperature, the PL peak position shifts towards shorter wavelength and the intensity decreases and disappears at bath temperatures below 170 K. The data in Fig. 4.12(a) suggest that this occurs because the direct-band-gap PL is completely overwhelmed by the strong indirect-band-gap PL. The reduction of direct-band-gap PL with decreasing temperature is attributed to reduced occupancy of the Γ valley due to the sharper energy distribution of the carriers [25, 27]. The PL peak from the Ge NWs has the same tendency. As shown in Fig. 4.12(b), with decreasing bath temperature,

the PL peak position of the Ge NWs shifts towards shorter wavelength and the intensity decreases continuously. The peak becomes unobservable at bath temperatures below 130 K. The similar behavior of the PL spectrum of the Ge NWs to that of the direct-band-gap PL component of bulk Ge provides further support for the conclusion that the observed PL from the Ge NWs is due to direct-band-gap recombination in the Ge NWs.
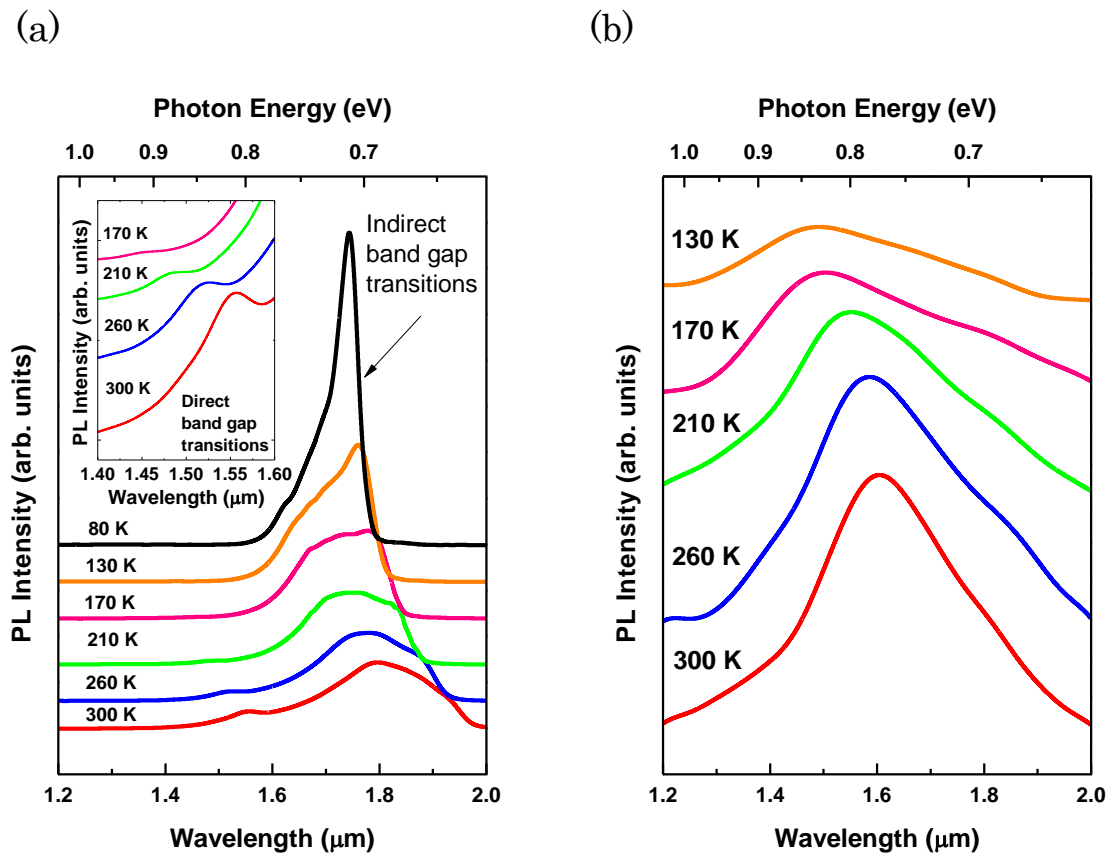
(a)   (b)

Figure 4.12 NIR PL spectra of (a) bulk Ge and (b) Ge NWs, measured at different bath temperatures. The inset in (a) shows the direct-band-gap PL spectra of the bulk Ge in the wavelength range of 1.40 to 1.60 µm. The numbers above the spectra indicate the bath temperatures. The excitation laser power impinging on the both samples is 40 mW.

4.5.3   Laser-Induced Heating Effects

We now turn our attention to the origin of the redshift of the PL peaks of the Ge NWs shown in Fig. 4.10(a). This can be explained by laser-induced heating and subsequent heat trapping within the ensemble of dense NWs (Figure 4.5). It is well-known that at elevated temperatures the PL peak shifts towards longer wavelength at a constant pressure due to thermal expansion of the lattice and renormalization of band-gap energies by electron-phonon interactions on the corresponding electronic states [35−37]. The latter effect gives the predominant contribution as shown in Ref. 35−37, which will not be discussed further here. In a dense NW array, a fraction of the scattered PL and laser light as well as thermal radiation emitted by the NWs is confined within the array, causing ensemble heating [38−40]. Such heating effects cause the redshift and thermal broadening of the direct-band-gap PL observed in our measurements of Ge NWs [38−40]. This effect is not significant in bulk Ge because the light as well as the thermal radiation are more readily able to escape from the illuminated sample region to its surroundings [38, 39].

In order to estimate the temperatures of the Ge NW ensemble during the PL measurements, we performed PL measurements on bulk Ge at temperatures between 300 and 470 K under atmospheric pressure and approximated a linear temperature coefficient of direct-band-gap transitions of Ge. We find the value of $\Delta E/\Delta T = -4.4 \times 10^{-4}$ eV in this temperature range, which is consistent with previous investigations [35−37]. Figure 4.13 displays the comparison of the PL peak energies of the Ge NWs as a function of excitation laser power measured at a bath temperature of 300 K and the linear temperature dependence of direct-band-gap recombination in the bulk Ge. The excellent agreement also supports our assumption that the PL from the Ge NWs originates from direct-band-gap recombination. These data indicate that the temperature of the NWs can reach 450 K with 40 mW laser excitation for the Ge NW arrays investigated. It is worth noting that the laser-induced heating effects alone cannot explain the absence of indirect-band-gap PL from the Ge NWs because measurements at estimated-temperatures below 190 K did not show any significant PL signal near the indirect-band-gap recombination.
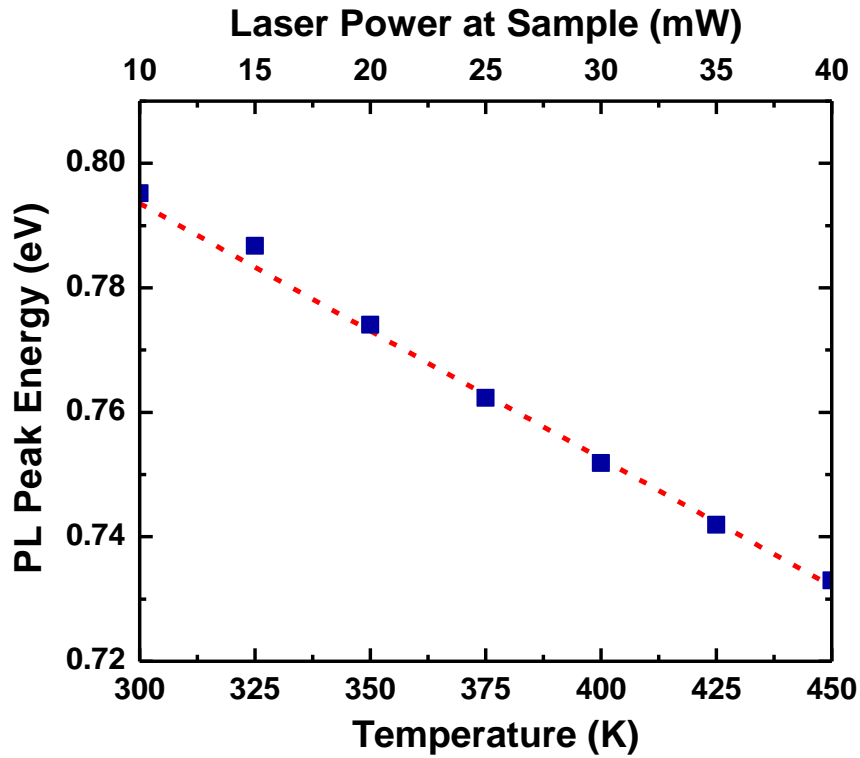
Figure 4.13 Fit of PL peak energies of Ge NWs as a function of excitation laser power at bath temperature of 300 K (filled squares) to a linear temperature dependence of direct-band-gap recombination in bulk Ge in the temperature range of 300 to 470 K (dashed line) obtained in this work.

.

4.6   Discussion: Surface Effects

Several publications have previously indicated that carrier trapping at surface defects and subsequent non-radiative recombination dominates carrier relaxation in semiconductor NWs [34, 41−43]. A thin native oxide layer forms on air-exposed Ge surfaces. The resulting surface states can be categorized as either "slow" or "fast" [34, 44−46]. Slow surface states are either in the oxide layer or on its surface, influencing carrier transport on timescale of seconds to hundreds of seconds [34, 44−46]. The influence of the slow surface states on carrier transport

through Ge NWs has been extensively characterized in Ref. 47. In contrast, fast surface states reside at the interface between Ge and the oxide layer and are chiefly involved in recombination on a timescale of nanoseconds or less [34, 44−46]. Carrier traps associated with fast surface states may be responsible for the failure to observe a strong PL signature for indirect-band-gap transitions in the Ge NWs studied in this work. The non-radiative recombination lifetime of photogenerated carriers via GeO_x/Ge nanowire interface states, τ_{nrs}, can be approximated as [48, 49]

$$\frac{1}{\tau_{nrs}} \cong \frac{4S}{d}, \tag{5.2}$$

where S is the surface recombination velocity and d is the NW diameter. Using the reported surface recombination velocity of bulk Ge with a native oxide coating, $S = 1300$ cm/s [50], in Eq. (5.2), gives a value of $\tau_{nrs} = 1$ ns for these undoped nanowires. In contrast, the radiative recombination lifetime for the indirect-band-gap PL in intrinsic Ge is ~ 1 s, as determined by photoconductivity measurements [51] and detailed balance calculations from photon absorption data [52]. This suggests that electrons in the L valley are very likely to recombine non-radiatively in the Ge NWs prior to their radiative recombination. Both experimental [31] and theoretical [53] results indicate that, even if the density of occupied states in the Γ valley of intrinsic Ge is far lower than that of the L valley, the rate of direct-band-gap recombination is greater for electrons near $\mathbf{k} = 0$. The data in Figs. 4.10−13 suggest that the rate of radiative recombination via the direct band gap exceeds $1/\tau_{nrs}$ for the present nanowire experiments.

Very recently, much effort has been devoted to enhancing and controlling direct-band-gap emission in bulk Ge and Ge thin films. It has been shown that the PL intensity of direct-band-gap recombination in bulk Ge can be increased compared to that of the phonon-mediated indirect-band-gap recombination by simply increasing the excitation laser power [27−29]. The enhancement of direct-band-gap PL in bulk Ge [27, 32] and Ge-on-insulator [32] by high-concentration doping has been demonstrated. Furthermore, stronger enhancement of direct-band-gap transitions than indirect-band-gap transitions in bulk Ge under mechanical biaxial tensile strain [26, 54] and tensily strained

Ge layer with a *δ*-doping SiGe layer on Si and Si-on-insulator [55] has also been reported. Our observations of direct-band-gap emission from the Ge NWs are important for future Ge-NW-based optoelectronic devices and indicate that the size effect of NW diameter on non-radiative recombination rate expressed in Eq. (5.2) can be used to engineer important photonic properties. We expect that surface passivation of the wires through chemical treatments, growth of a high quality oxide layer, or growth of a semiconductor shell on the side walls may increase the radiative-to-non-radiative recombination ratio of direct-band-gap transitions, making Ge NWs even more attractive for device applications.

4.7   Conclusions

In conclusion, we have measured NIR PL of vertically aligned, free-standing Ge NWs grown on a Si(111) substrate. The Ge NWs give one broad PL peak near the crystalline Ge band gap ~1.55 µm (~0.8 eV). The observed PL peak is shifted towards longer wavelengths with increasing excitation laser power due to laser-induced heating and subsequent heat trapping within the dense array of NWs. In addition, the PL peak intensity shows a nearly quadratic dependence on excitation laser power and decreases with decreasing temperature, as can be seen in the direct-band-gap PL behavior of bulk Ge. These observations indicate that efficient direct-band-gap recombination is responsible for the observed PL from the Ge NWs. On the other hand, no peak was observed at the wavelength expected for indirect-band-gap PL. It was suggested by an analysis that carrier traps associated with fast surface states situating at the Ge NW/Ge native oxide interfaces might have been responsible for the absence of the indirect-band-gap PL.

References

[1] G. Audoit, E. Ni Mhuircheartaigh, S. M. Lipson, M. A. Morris, W. J. Blau, and J. D. Holmes, J. Mater. Chem. **15**, 4809 (2005).

[2] D. M. Lyons, K. M. Ryan, M. A. Morris, and J. D. Holmes, Nano Lett. **2**, 811

(2002).

[3] J. Engvall, J. Olajos, H. G. Grimmeiss, H. Kibbel, and H. Presting, Phys. Rev. B **51**, 2001 (1995).

[4] J. Olajos, J. Engvall, H. G. Grimmeiss, M. Gail, G. Abstreiter, H. Presting, and H. Kibbel, Phys. Rev. B **54**, 1922 (1996).

[5] M. Bonfanti, E. Grilli, M. Guzzi, M. Virgilio, G. Grosso, D. Chrastina, G. Issella, H. and von Kanel, Phys. Rev. B **78**, 041407 (2008).

[6] Y. Chen, C. Li, Z. Zhou, H. Lai, S. Chen, W. Ding, B. Cheng, and Y. Yu, Appl Phys. Lett. **94**, 141902 (2009).

[7] E. Gatti, E. Grilli, M. Guzzi, D. Chrastina, G. Isella, and H. von Kanel, Appl. Phys. Lett. **98**, 031106 (2011).

[8] D. C. Paine, C. Caragianis, T. Y. Kim, Y. Shigesato, and T. Ishahara, Appl. Phys. Lett. **62**, 2842 (1993).

[9] Y. Maeda, Phys. Rev. B **51**, 1658 (1995).

[10] M. Zacharias and P. M. Fauchet, Appl. Phys. Lett. **71,** 380 (1997).

[11] C. L. Yuan and P. S. Lee, Europhys. Lett. **83**, 47010 (2008).

[12] C. L. Yuan, H. Cai, P. S. Lee, J. Guo, and J. He, J. Phys. Chem. C **113**, 19863 (2009).

[13] K. S. Min, K. V. Shcheglov, C. M. Yang, H. A. Atwater, M. L. Brongersma, and A. Polman, Appl. Phys. Lett. **68**, 2511 (1996).

[14] S. Takeoka, M. Fujii, S. Hayashi, and K. Yamamoto, Phys. Rev. B **58**, 7921 (1998).

[15] M. P. Halsall, H. Omi, and T. Ogino, Appl. Phys. Lett. **81**, 2448 (2002).

[16] H. Sunamura, N. Usami, Y. Shiraki, and S. Fukatsu, Appl. Phys. Lett. **68**, 1847 (1996).

[17] H. Adhikari, A. F. Marshall, C. E. D. Chidsey, and P. C. McIntyre, Nano Lett. **6**, 318 (2006).

[18] H. Jagannathan, M. Deal, Y. Nishi, J. Woodruff, C. Chidsey, and P. C. McIntyre, J. Appl. Phys. **100**, 024318 (2006).

[19] T. I. Kamins, X. Li, R. S. Williams, and X. Liu, Nano Lett. **4**, 503 (2004).

[20] E. Tutuc, J. Appenzeller, M. C. Reuter, and S. Guha, Nano Lett. **6**, 2070 (2006).

[21] S. Zhang, E. R. Hemesath, D. E. Perea, D. Wijaya, J. L. Lensch-Falk, and L.

J. Lauhon, Nano Lett. **9**, 3268 (2009).

[22] B. V. Kamenev, V. Sharma, L. Tsybeskov, and T. I. Kamins, Phys. Stat. Sol. **202**, 1753 (2005).

[23] R. S. Wagner and W. C. Ellis, Appl. Phys. Lett. **4**, 89 (1964).

[24] I. A. Goldthorpe, Ph.D Thesis, Stanford University, (2009) p.20.

[25] H. M. van Driel, A. Elci, J. S. Bessey, and M. O. Scully, Solid State Commun. **20**, 837 (1976).

[26] T. -H. Cheng, K. -L. Peng, C. -Y. Ko, C. -Y. Chen, H. -S. Lan, Y. -R. Wu, C. W. Liu, and H. -H. Tseng, Appl. Phys. Lett. **96**, 211108 (2010).

[27] T. Arguirov, M. Kittler, and N. V. Abrosimov, J. Phys.: Conf. Ser. **281**, 012021 (2011).

[28] T. -H. Cheng, C. -Y. Ko, C. -Y. Chen, K. -L. Peng, G. -L. Luo, C. W. Liu, and H. -H. Tseng, Appl. Phys. Lett. 96, 091105 (2010).

[29] W. Klingesten and H. Schweizer, Solid-State Electron. **21**, 1371 (1978).

[30] S. -R. Jan, C. -Y. Chen, C. -H. Lee, S. -T. Chan, K. -L. Peng, C. W. Liu, Y. Yamamoto, and B. Tillack, Appl. Phys. Lett. **98**, 141105 (2011).

[31] J. Haynes, Phys. Rev. **98**, 1866 (1955).

[32] M. El Kurdi, T. Kociniewski, T. -P. Ngo, J. Boulmer, D. Debarre, P. Boucaud, J. F. Damlencout, O. Kermarrec, and D. Bensahel, Appl Phys. Lett. **94**, 191107 (2009).

[33] J. R. Haynes, M. Lax, and W. F. Flood, J. Phys. Chem. Solids **8**, 392 (1959).

[34] R. P. Prasankumar, S. Choi, S. A. Trugman, S.T. Picraux, and A. Taylor, Nano Lett. **8**, 1619 (2008).

[35] H. Y. Fan, Phys. Rev. **82**, 900 (1951).

[36] P. B. Allen and M. Cardona, Phys. Rev. B **27**, 4760 (1983).

[37] P. Lautenschlager, P. B. Allen, and M. Cardona, Phys. Rev. B **31**, 2163 (1985).

[38] L. Bergman, X. -B. Chen, J. L. Morrison, J. Huso, and A. P. Purdy, J. Appl. Phys. **96**, 675 (2004).

[39] L. Bergman, X. -B. Chen, J. Feldmeier, and A. P. Purdy, Appl. Phys. Lett. **83**, 764 (2003).

[40] P. A. M. Rodrigues, P. Y. Yu, G. Tamulaitis, and S. H. Risbud, J. Appl. Phys. **80**, 5963 (1996).

[41] P. Parkinson, J. Lloyd-Hughes, Q. Gao, H. H. Tan, C. Jagadish, M. B.

Johnston, and L. M. Herz, Nano Lett. **7**, 2162 (2007).

[42] L. V. Titova, T. B. Hoang, J. M. Yarrison-Rice, H. E. Jackson, Y. Kim, H. J. Joyce, Q. Gao, H. H. Tan, C. Jagadish, X. Zhang, J. Zou, and L. M. Smith, Nano Lett. **7**, 3383 (2007).

[43] S. Reitzenstein, S. Munch, C. Hofmann, A. Forchel, S. Crankshaw, L. C. Chuang, M. Moewe, and C. Chang-Hasnain, Appl. Phys. Lett. **91**, 091103 (2007).

[44] D. H. Lindley and P. C. Banbury, Proc. Phys. Soc. **74**, 395 (1959).

[45] R. H. Kingston, J. Appl. Phys. **27**, 101 (1956).

[46] H. Statz, G. A. deMars, L.J. Davis, and A. J. Adams, Phys. Rev. **101**, 1272 (1956).

[47] T. Hanrath and B. A. Korgel, J. Phys. Chem. B **109**, 5518 (2005).

[48] Y. Dan, K. Seo, K. Takei, J. H. Meza, A. Javey, and K. B. Crozier, Nano Lett. **11**(6), 2527 (2011).

[49] J. E. Allen, E. R. Hemesath, D. E. Perea, J. L. Lensch-Falk, Z. Y. Li, F. Yin, M. H. Gass, P. Wang, A. L. Bleloch, R. E. Palmer, and L. J. Lauhon, Nature Nanotechnol. **3**, 168 (2008).

[50] N. Derhacobian, P. Fine, J. T. Walton, Y. K. Wong, C. S. Rossington, and P. N. Luke, IEEE Trans. Nuclear Sci. **41**, 1026 (1994).

[51] P. H. Brill and R. F. Schwartz, Phys. Rev. **112**, 330 (1958).

[52] W. van Roosbrozck and W. Shockley, Phys. Rev. **94**, 1558 (1954)

[53] W. P. Dumke, Phys. Rev., **105**, 139 (1957).

[54] M. El Kurdi, H. Bertin, E. Martincic, M. de Kersauson, G. Fishman, S. Sauvage, A. Bosseboeuf, and P. Boucaud, Appl Phys. Lett. **96**, 041909 (2010).

[55] C. Li, Y. Chen, Z. Zhou, H. Lai, and S. Chen, Appl. Phys. Lett. **95**, 251102 (2009).

Chapter 5

Conclusions

The present thesis has focused on understanding of defect and surface behaviors in germanium (Ge).

Chapter 2 presented an experiment investigation of the effect of arsenic (As) impurity ion-implantation on the host Ge atomic displacement and amorphization. The Ge samples were cooled down to liquid-nitrogen temperature during implantation since the same implantation performed at room temperature led to elevation of the sample temperature causing redistribution of Ge atoms displaced by the As bombardment. Ge isotope superlattices (SLs), composed of alternating layers of stable isotope ^{70}Ge and naturally available Ge (^{nat}Ge), were grown by solid-source molecular beam epitaxy (MBE). As was ion-implanted into the Ge isotope SLs from the surfaces with doses in the range of 5×13 to 5×14 cm^{-2} at an energy of 90 keV. Ge host-atoms were displaced by collisions with implanted As ions and a part of the crystalline Ge region underwent a phase transition into an amorphous state. As a result, the ^{74}Ge periodicity in the depth profiles of the SLs measured by secondary ion mass spectroscopy (SIMS) after implantation was perturbed compared to the profiles before implantation. The degree of Ge mixing in the SLs increased with increasing implantation doses. The average length of the Ge displacement due to the collisions with As ions was obtained by reproducing the SIMS depth profiles of ^{74}Ge by a numerical model based on convolution integrals. Further observation of the sample structures by cross-sectional transmission

electron microscopy (XTEM) revealed that amorphization occurs in the region having the Ge displacements larger than 0.75 nm. This critical displacement for amorphization, 0.75 nm, was found to be independent of implantation doses. Interestingly, this critical value is 50% larger than 0.5 nm of silicon [1].

Chapter 3 presented the effect of compressive biaxial strain on self-diffusion in Ge. Growth of a biaxial compressive strained-Ge (s-Ge) isotope SL, composed of alternating layers of stable isotope ^{70}Ge and ^{nat}Ge, was achieved by sandwiching a Ge isotope SL by relaxed ^{nat}Si$_{0.2}$^{nat}Ge$_{0.8}$ layers. This sample was cut into smaller pieces and annealed at various temperatures in the range of 475−600 °C and the duration of 0.5–61 hours. The compressive biaxial strain in the SL was found to be 0.71% before the diffusion annealing by an (224) asymmetrical reciprocal space mapping (RSM) in X-ray diffraction. RSM and XTEM observations after annealing confirmed that the s-Ge isotope SL remained pseudomorphic to the sandwiching relaxed Si$_{0.2}$Ge$_{0.8}$ layers. The self-diffusivities in s-Ge were determined by reproducing the SIMS depth profiles of ^{74}Ge in the Ge isotope SLs by a partial differential equation solver using a series of differential equations involved in our analysis. It was found that self-diffusivity in Ge was enhanced by the compressive biaxial stain. The degree of the enhancement was fully consistent with a theoretical prediction of a generalized activation volume model for a simple vacancy-mediated diffusion developed by Aziz *et al.* [2−4]. The activation volume of −(0.65±0.21) times the Ge atomic volume reproduced the experimentally observed enhancement very well.

Chapter 4 presented the first observation of near-infrared (NIR) photoluminescence (PL) from Ge nanowires (NWs). Ge NWs with an average diameter of 40 nm were grown vertically on a (111)-oriented Si substrate via vapor-liquid-solid mechanism using chemical vapor deposition. The samples were excited by means of a frequency doubled Nd:YAG diode-pumped solid-state laser, emitting continuous-wave at a wavelength of 532 nm. The incident laser power on the sample surfaces was varied between 10 and 40 mW. The Ge NWs yielded one broad PL peak centered at the wavelength near the crystalline Ge band gap ~1.55 μm (~0.8 eV) with luminescence spanning between 1100 and 2200 nm. The peak position shifted to longer wavelength with increasing excitation laser power due to laser-induced heating and subsequent heat

trapping within the dense array of NWs. The PL peak intensity showed a nearly quadratic dependence on excitation laser power and decreased with decreasing temperature in the manner similar to the behavior of the direct-band-gap PL from bulk Ge. Based on these observations, it is concluded that direct-band-gap recombination was responsible for the observed PL peak from the Ge NWs. On the other hand, no peak was observed at the wavelength expected for indirect-band-gap PL. Analysis of carrier recombination rates using data in the literature suggests carrier traps associated with fast surface states situating at the Ge NW/Ge native oxide interfaces may have been responsible for the absence of detectable indirect-band-gap PL.

References

[1] Y. Shimizu, M. Uematsu, K. M. Itoh, A. Takano, K. Sawano, and Y. Shiraki, Appl. Phys. Express **1**, 021401 (2008).

[2] M. J. Aziz, Appl. Phys. Lett. **70**, 2810 (1997).

[3] M. J. Aziz, Mater. Sci. Semicond. Process. **4**, 397 (2001).

[4] M. J. Aziz, Y. Zhao, H. J. Gossmann, S. Mitha, S. P. Smith, and D. Schiferl, Phys. Rev. B **73**, 054101 (2006).

List of Publications

[Journal Articles]

1. **Y. Kawamura**, K. C. Y. Haung, S. V. Thombare, S. Hu, M. Gunji, T. Ishikawa, M. Brongersma, K. M. Itoh, and P. C. McIntyre
   "Direct-gap photoluminescence from germanium nanowires"
   submitted to Nano Letters (2011).

2. S. Hu, **Y. Kawamura**, K. C. Y. Huang, Y. Li, A. F. Marshall, K. M. Itoh, M. Brongersma and P. C. McIntyre
   "Thermal stability and surface passivation of Ge nanowires coated by epitaxial SiGe shells"
   submitted to Nano Letters (2011).

3. M. Tomita, M. Koike, H. Akutsu, S. Takeno, **Y. Kawamura**, Y. Shimizu, M. Uematsu, and K. M. Itoh
   "Investigation of the factors determining the SIMS depth resolution in silicon-isotope multiple layers"
   Journal of Vacuum Science and Technology B **30**, 011803 (2011).

4. **Y. Kawamura**, M. Uematsu, Y. Hoshi, K. Sawano, M. Myronov, Y. Shiraki, E. E. Haller, and K. M. Itoh
   "Ge self-diffusion in compressively strained Ge"
   Journal of Applied Physics **110**, 034906 (2011).

5. L. J. García, **Y. Kawamura**, M. Uematsu, and K. M. Itoh
   "Monte Carlo simulation of silicon atomic displacement and amorphization induced by ion implantation"
   Journal of Applied Physics **109**, 123507 (2011).

6. Y. Shimizu, **Y. Kawamura**, M. Uematsu, M. Tomita, T. Kinno, N. Okada, M. Kato, H. Uchida, M. Takahashi, H. Ito, H. Ishikawa, Y. Ohji, H. Takamizawa,

Y. Nagai, and K. M. Itoh

"*Depth and lateral resolution of laser-assisted atom probe microscopy of silicon revealed by isotopic heterostructures*"

Journal of Applied Physics **109**, 036102 (2011).

7. O. Moutanabbir, D. Isheim, D. N. Seidman, <u>**Y. Kawamura**</u>, and K. M. Itoh,

"*Ultraviolet-laser atom-probe tomographic 3-D atom-by-atom imaging of isotopically modulated Si nanoscopic layers*"

Applied Physics Letters **98**, 013111 (2011).

8. <u>**Y. Kawamura**</u>, Y. Shimizu, H. Oshikawa, M. Uematsu, E. E. Haller, and K. M. Itoh

"*Critical Displacement of Host-Atoms for Amorphization in Germanium Induced by Arsenic Implantation*"

Applied Physics Express **3**, 071303 (2010).

9. <u>**Y. Kawamura**</u>, Y. Shimizu, H. Oshikawa, M. Uematsu, E. E. Haller and K. M. Itoh

"*Quantitative evaluation of germanium displacement induced by arsenic implantation using gemanium isotope superlattices*"

Physica B **404**, 4546 (2009).

10. Y. Shimizu, <u>**Y. Kawamura**</u>, M. Uematsu, K. M. Itoh, M. Tomita, M. Sasaki, H. Uchida, and M. Takahashi

"*Atom probe microscopy of three-dimensional distribution of silicon isotopes in 28Si/30Si isotope superlattices with sub-nanometer spatial resolution*"

Journal of Applied Physics **106**, 076102 (2009).

11. M. Naganawa, <u>**Y. Kawamura**</u>, Y. Shimizu, M. Uematsu, K. M. Itoh, H. Ito, M. Nakamura, H. Ishikawa, and Y. Ohji

"*Accurate Determination of the Intrinsic Diffusivities of Boron, Phosphorus, and Arsenic in Silicon : The Influence of SiO_2 Film*"

Japanese Journal of Applied Physics **47**, 6205 (2008).

[International Conferences]

1. <u>**Y. Kawamura**</u>, M. Uematsu, K. M. Itoh, Y. Hoshi, K. Sawano, Y. Shiraki, E. E. Haller, and M. Myronov

   "Germanium self-diffusion in compressive-strained germanium grown on relaxed SiGe"

   International Conference on Solid State Devices and Materials, The University of Tokyo, Japan. (September 2010).

2. <u>**Y. Kawamura**</u>, Y. Shimizu, H. Oshikawa, M. Uematsu, and K. M. Itoh

   "Quantitative evaluation of germanium displacement induced by arsenic implantation using gemanium isotope superlattices"

   25th International Conference on Defects in Semiconductors, Saint Petersburg, Russia. (July 2009)

3. <u>**Y. Kawamura**</u>, M. Naganawa, Y. Shimizu, M. Uematsu, K. M. Itoh, H. Ito, M. Nakamura, H. Ishikawa, and Y. Ohji

   "Accurate determination of the intrinsic diffusivities of boron phosphorus and arsenic in silicon: The influence of SiO2 films"

   Material Research Society International Materials Research Conference, Chongqing, China. (June 2008)

[Domestic Conferences]

1. <u>**河村踊子**</u>，植松真司，伊藤公平，星裕介，澤野憲太郎，Maksym Myronov，白木靖寛，Eugene E. Haller，伊藤公平

   "圧縮歪ゲルマニウム中の自己拡散"

   第58回応用物理学関係連合講演会，神奈川工科大学，2011年3月.

2. <u>**河村踊子**</u>，清水康雄，押川浩之，植松真司，E. E. Haller，伊藤公平

   "Ge同位体超格子を用いた砒素イオン注入によるGe原子のミキシング評価"

   第70回応用物理学会学術講演会，富山大学，2009年9月.

3. <u>**河村踊子**</u>，長縄美樹，清水康雄，植松真司，伊藤公平，伊藤浩之，中村光利，石川英明，大路譲

   "Ｓｉ基板中のＢ拡散における表面シリコン酸化膜の影響"

   第68回応用物理学会学術講演会，北海道工業大学，2008年9月